

Statistical and Dynamical Properties in the Energy
Spectra of XXZ Spin Chains

Kazue KUDO

Integrated Sciences, Graduate School of Humanities and Sciences,
Ochanomizu University

January, 2005

Abstract

Spectral properties of XXZ spin chains are studied intensively. The integrable XXZ spin chain is one of the most important quantum integrable systems, and its Hamiltonian is given by

$$\mathcal{H} = J \sum_{j=1}^L (S_j^x S_{j+1}^x + S_j^y S_{j+1}^y + \Delta S_j^z S_{j+1}^z). \quad (1)$$

Here, L is the number of sites; $S_j^\alpha = \frac{1}{2}\sigma_j^\alpha$ and σ_j^α ($\alpha = x, y, z$) is the Pauli matrix on the j th site. Equation (1) corresponds to the Heisenberg spin chain at $\Delta = 1$, to the XY model at $\Delta = 0$, and to the Ising spin chain when $\Delta \rightarrow \infty$. In this thesis, we study on XXZ spin chains with next-nearest-neighbor (NNN) coupling and/or with a magnetic field as well as Eq. (1).

First, we discuss level crossings in the energy spectra of the integrable XXZ spin chain. Some of the level crossings are counterexamples of a theorem by von Neumann and Wigner: two energy levels with the same symmetry rarely cross each other in the flow of the spectrum. Multiple degeneracies appear at the particular crossing points where the symmetry of the system is enhanced in the spectral flow. The eigenvalues and the eigenvectors are obtained in an analytical form for 3-site and 4-site chains. The spectral flow of a 6-site chain is shown by numerical calculation.

Not only level crossings but also “level bifurcations” are found in the flow of eigenvalues for the inhomogeneous transfer matrix of the XXZ spin chain. The “level bifurcations” are branches such as bifurcation or multiple branches in the flow of eigenvalues and not observed for the homogeneous transfer matrix. The observations are obtained by numerical calculation. We also confirm the appearance of some of the branches through the Bethe ansatz method. The behavior of some branching points are analyzed in the flow of eigenvalues for a particular inhomogeneous case.

Level statistics is discussed for the XXZ spin chains with NNN coupling or with a random magnetic field. Evaluating the level-spacing distribution, the spectral rigidity and the number variance, we confirm the following conjecture: the level-spacing distribution should be described by the Poisson distribution for an integrable model and by the Wigner distribution for a nonintegrable model. The XXZ spin chains with the NNN coupling (J_2) or with a random magnetic field (h) are nonintegrable, so that mostly the level statistics shows Wigner behavior. However, the level statistics even for a nonintegrable model sometimes shows Poisson-like behavior because of the finite-size effects. For the NNN coupled XXZ spin chain, the behavior of level statistics comes close to the Poissonian around $J_2 = 0$ and/or $\Delta = 1$. As h/J becomes large, Poisson-like behavior appears for

the level statistics of the XXZ spin chain under random magnetic field. When $h/J \simeq 0$, however, Poisson-like behavior appears for small L .

In addition to the Poisson-like behavior, unexpected non-Wigner behavior of level statistics can appear due to mixed symmetry. When we discuss level statistics, we have to consider the whole symmetry of a system and perform desymmetrization. The NNN coupled XXZ chains are invariant under spin rotation around the z axis, translation, reflection. However, we have to consider spin reversal symmetry only when $S_{\text{tot}}^z = 0$. If spin reversal symmetry is not considered for $S_{\text{tot}}^z = 0$, the behavior of level statistics is described by almost the numerical average of Poisson and Wigner behavior.

To observe the dynamical properties of the energy spectra, we investigate energy diffusion for NNN coupled XXZ spin chains in the presence of a periodically oscillating magnetic field. Diffusion coefficients (D) are found to obey the power law with respect to both the field strength (B_0) and driving frequency (ω): $D \propto (B_0\omega)^\beta$. We observe that $\beta = 2$ for “linear response regime” and $\beta = 1$ for “non-perturbative regime”. In the linear response regime, the diffusion coefficient can be calculated using the Kubo formula. On the other hand, $B_0\omega$ is so large in the non-perturbative regime that the perturbation theory fails. The diffusion coefficient is smaller than that predicted by the Kubo formula and the perturbation theory fails in the non-perturbative regime. The ranges of the linear response and the non-perturbative regimes depend on J_2 . When J_2 is small, we observe large-amplitude oscillations, which is attributed to a non-diffusive and ballistic nature of the underlying energy diffusion.

In this way, we investigate the energy spectra of finite quantum XXZ spin chains in several different aspects. We hope that the results of the thesis will contribute to the development of the physics of low-dimensional systems and mesoscopic systems.

Contents

1	Introduction	3
2	Level Crossing	7
2.1	The eigenvalues and the eigenvectors of 3-site and 4-site XXZ spin chains	7
2.2	The spectral flow of the XXZ spin chain on 6 sites.	13
3	Level Bifurcation	14
3.1	Transfer matrix	14
3.2	Eigenvalues of the transfer matrix obtained by numerical diagonalization .	15
3.3	Eigenvalues of the transfer matrix obtained through the Bethe ansatz method	19
3.4	Discussion	20
4	Level Statistics	23
4.1	Preliminaries	23
4.2	Models and numerical procedure	25
4.2.1	Models	25
4.2.2	Desymmetrization	26
4.2.3	Unfolding	27
4.2.4	Level-spacing distribution, spectral rigidity and number variance . .	28
4.3	Integrable XXZ spin chain	31
4.4	Next-nearest-neighbor coupled XXZ spin chains	31
4.4.1	Wigner behavior for $S_{\text{tot}}^z = 0$	31
4.4.2	How does non-Wigner behavior appear?	33
4.4.3	Finite-size effects on the level spacing distribution	37
4.4.4	Homogeneity of the characteristic behavior of level statistics through- out the spectrum	38
4.5	XXZ spin chains under random magnetic field	40
4.5.1	Dependence on the anisotropy parameter Δ	40
4.5.2	Dependence on the magnetic field	42
4.5.3	Dependence on the system size	44

4.5.4	Homogeneity of the characteristic behavior of level statistics throughout the spectrum	46
4.6	Summary	46
5	Energy Diffusion	47
5.1	Preliminaries	47
5.2	What is energy diffusion like?	49
5.3	Numerical procedure	49
5.4	Time dependence of energy variance	51
5.5	Diffusion coefficients: dependence on field strength and frequency	52
5.6	Oscillation of energy diffusion in weakly-frustrated cases	55
5.7	Summary	60
6	Conclusions	61
A	Hamiltonian Matrix	64
B	Jordan-Wigner and Fourier Transformations	66
C	Spin reversal symmetry on momentum-based fermions	69
D	Spin reversal operation on the vacuum state	71
E	Energy diffusion for a random matrix model	73

Chapter 1

Introduction

A repulsion of two close levels is often discussed for various quantum systems through the perturbation theory [1, 2, 3]. Now we consider a Hamiltonian which is given by

$$H = H_0 + V, \quad (1.1)$$

where H_0 is the non-perturbative part and V is the perturbative part. When H_0 has two close eigenvalues ε_1 and ε_2 , where the corresponding eigenstates are ϕ_1 and ϕ_2 , we can assume that the eigenstates of H should be given by

$$\psi = c_1\phi_1 + c_2\phi_2. \quad (1.2)$$

Then, the time-independent Schrödinger equation is

$$H\psi = E\psi, \quad (1.3)$$

where

$$H = \begin{pmatrix} H_{11} & H_{12} \\ H_{21} & H_{22} \end{pmatrix}. \quad (1.4)$$

The solutions of the equation is written as

$$E_1 = \frac{1}{2}(H_{11} + H_{22}) + \frac{1}{2}\sqrt{(H_{11} - H_{22})^2 + 4|H_{12}|^2}, \quad (1.5)$$

$$E_2 = \frac{1}{2}(H_{11} + H_{22}) - \frac{1}{2}\sqrt{(H_{11} - H_{22})^2 + 4|H_{12}|^2}. \quad (1.6)$$

The energy levels are drawn in Fig. 1.1 as the functions of $x = H_{11} - H_{22}$. If the two levels have different symmetries, the level repulsion does not necessarily occur, since we can choose such a basis that the non-diagonal elements H_{12} and H_{21} equal 0. If the two levels have the same set of symmetry quantum numbers, however, the non-diagonal elements are generally nonzero and the level repulsion occurs.

According to a theorem by von Neumann and Wigner, two energy levels with the same symmetry rarely cross each other in the flow of the spectrum [4]. Here we assume

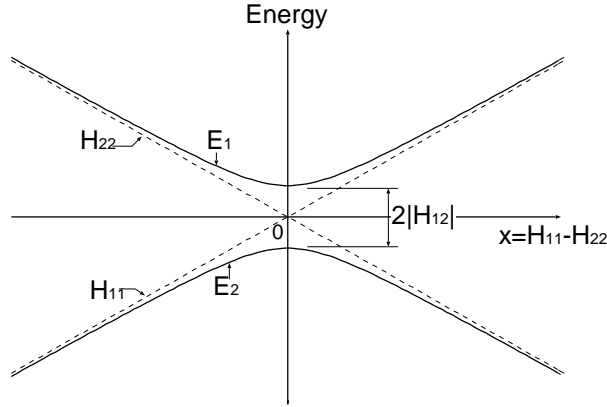


Figure 1.1: Level repulsion. (See text.)

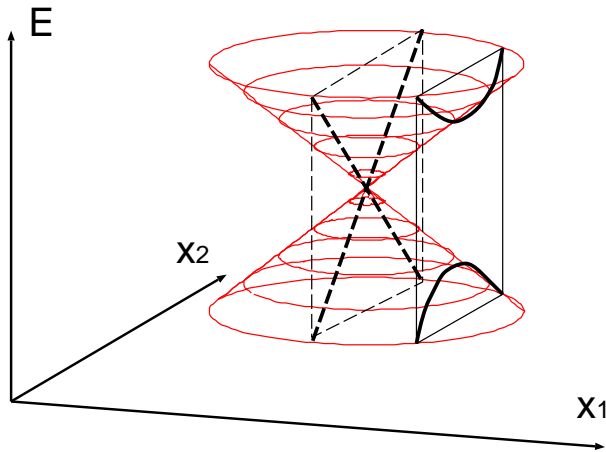


Figure 1.2: Energy surfaces which have the same symmetry. x_1 and x_2 are real parameters.

that the Hamiltonian matrix depends on two real parameters. Then the energy surfaces which have the same symmetry near the crossing point are given by two circular cones as shown in Fig. 1.2. We suppose the spectral flow is given by changing a parameter x_2 , where x_1 is fixed. Generally, a level crossing does not happen (Solid lines in Fig. 1.2). When x_1 is chosen to be through the top of the cones, however, the level crossing occurs (Dashed lines in Fig. 1.2). In other words, levels of the same symmetry can cross in the spectral flow, although the possibility is very small. When the level crossing occurs, the levels are degenerate at the crossing. We call such a degeneracy an accidental degeneracy. Some examples of accidental degeneracies are discussed, which give counterexamples to the noncrossing rule [5, 6]. In particular, it is shown by Heilmann and Lieb that the one-dimensional Hubbard model with the Hubbard coupling U provides a quantum mechanical counterexample to the noncrossing rule [5].

The above arguments indicate that spectral properties are relevant to symmetry of a

system. In this thesis, spectral properties are studied for quantum XXZ spin chains, which can have extraordinary symmetry, i.e. sl_2 loop algebra symmetry. The XXZ Hamiltonian on L sites is given by

$$\mathcal{H} = J \sum_{j=1}^L (S_j^x S_{j+1}^x + S_j^y S_{j+1}^y + \Delta S_j^z S_{j+1}^z). \quad (1.7)$$

Here, $S_j^\alpha = \frac{1}{2}\sigma_j^\alpha$, and σ_j^α 's ($\alpha = x, y, z$) are the Pauli matrices acting on the j th site for $j = 1, \dots, L$. The XXZ Hamiltonian commutes with the sl_2 loop algebra when q is a root of unity, where q is defined by $\Delta = (q + q^{-1})/2$ [7]. The loop algebra is an infinite-dimensional Lie algebra and the dimensions of the largest degenerate eigenspaces are given by $N2^{L/N}$, where $q^{2N} = 1$ for an integer N [8, 9]. Thus the spectral degeneracy can increase exponentially with respect to L .

There is another motivation to study about XXZ spin chains. Quantum XXZ spin chains are related to various important systems of quantum spin chains. An XXZ spin chain corresponds to the Heisenberg spin chain at $\Delta = 1$, to the XY model at $\Delta = 0$, and to the Ising spin chain when $\Delta \rightarrow \infty$. Furthermore, XXZ spin chains with next-nearest-neighbor couplings are realized in quasi one-dimensional antiferromagnets: for example, CsCoBr₃, CsCoCl₃ [10], Cu(ampy)Br₂ [11] and (N₂H₅)CuCl₃ [12].

This thesis is based on 6 articles, i.e. Refs. [13, 14, 15, 16, 17, 18]. In Ref. [13], we have observed several level crossings associated with the sl_2 loop algebra symmetry in the spectral flow of the XXZ spin chain. Furthermore, novel spectral phenomena have been found in Ref. [14]. We have observed that branches appear in the spectral flow for the inhomogeneous transfer matrix of the XXZ spin chain. The spectral branches are important, since an inhomogeneous transfer matrix plays a central role in the exact calculation of thermodynamic quantities for the spin chain.

In Ref. [15], we have discussed the level-spacing distributions of next-nearest-neighbor (NNN) coupled XXZ spin chains to investigate the statistical behavior of their whole energy spectra. It is well known that a level-spacing distribution is described by the Poisson distribution for an integrable model and by the Wigner distribution for a nonintegrable model. Though the NNN coupled XXZ spin chains are nonintegrable models, robust non-Wigner behavior has been seen. To find possible distribution of another nonintegrable XXZ model, i.e. an XXZ spin chain under random magnetic field, in Ref. [16]. We have shown how the level-spacing distributions depend on the lattice size, the anisotropy parameter and the magnetic field. In Ref. [17], we have solved the unexpected non-Wigner behavior of the level-spacing distributions of the NNN coupled XXZ spin chains. We have demonstrated that mixed symmetry and finite effects can lead to the unexpected behavior of level statistics. We have also shown that the characteristic behavior of level statistics does not depend on the spectral range for the XXZ spin chains.

We have investigated dynamics for the XXZ spin chains in Ref. [18]. The nature

of energy diffusion has been analyzed for NNN coupled XXZ spin chains with an applied periodically oscillating magnetic field. We have evaluated the time dependence of energy variance and shown how the diffusion coefficients depend on the coupling constants, the anisotropy parameter, the magnetic field and the driving frequency.

The organization of this thesis is the following. We show some counterexamples to the noncrossing rule in Chapter 2. The spectral flows are calculated for the XXZ spin chains on 3, 4, and 6 sites. Diagonalizing the Hamiltonian, we observe several level crossings corresponding to the sl_2 loop algebra symmetry. In Chapter 3, novel spectral phenomena are shown in the spectral flow of the XXZ transfer matrix. One spectral line may split into two spectral lines in the spectral flow of the inhomogeneous XXZ transfer matrix. Such branches appear in the spectral flow for the inhomogeneous case, while no branches appear for the homogeneous case. In Chapter 4, level statistics is discussed for XXZ spin chains with next-nearest-neighbor couplings or with a random magnetic field. Level statistics is described by Poisson behavior for integrable models and Wigner behavior for nonintegrable ones. We investigate the correspondence between non-integrability and Wigner behavior. We also refer that level statistics is influenced by finite-size effects and the symmetry of the system. Dynamical properties of the energy spectra are discussed in Chapter 5. As dynamics of energy levels, energy diffusion is investigated. Diffusion coefficients are found to obey the power law with respect to both the field strength and driving frequency with its power varying depending on the linear response and non-perturbative regimes. Finally, we give conclusions in Chapter 6.

Chapter 2

Level Crossing

Two energy levels with the same symmetry rarely cross each other. The integrable XXZ spin chain, however, has many level crossings at some particular values of the anisotropy parameter associated with roots of unity. Diagonalizing the Hamiltonian of the XXZ spin chain, we indeed observe some of such level crossings [13].

In this chapter, the eigenvalues and the eigenvectors are resolved analytically for 3-site and 4-site XXZ spin chains under the twisted boundary conditions. It will be useful in the future to show analytical forms of the eigenvalues and the eigenvectors of XXZ spin chains, even though the size of the chains is small. Furthermore, the spectral flow is shown for the 6-site XXZ spin chain. Then several level crossings related to the sl_2 loop algebra symmetry are observed.

2.1 The eigenvalues and the eigenvectors of 3-site and 4-site XXZ spin chains

First of all, let us rewrite the Hamiltonian (1.7) by using $\sigma_j^+ = (\sigma_j^x + i\sigma_j^y)/2$ and $\sigma_j^- = (\sigma_j^x - i\sigma_j^y)/2$:

$$\mathcal{H} = \frac{J}{4} \sum_{j=1}^L (2\sigma_j^+ \sigma_{j+1}^- + 2\sigma_j^- \sigma_{j+1}^+ + \Delta \sigma_j^z \sigma_{j+1}^z). \quad (2.1)$$

Here, twisted boundary conditions are imposed: $S_{L+1}^\pm = e^{\pm i\phi} S_1^\pm$, $S_{N+1}^z = S_1^z$. The conditions correspond to the state where a magnetic flux ϕ goes through the spin chain. The schematic picture of this model is shown in Fig. 2.1. In Appendix A, we show how to write the Hamiltonian matrix of Eq. (2.1).

The eigenvalues and eigenvectors are resolved analytically. They are listed in Tables 2.1 and 2.2 for $L = 3$ and $L = 4$, respectively. The eigenvectors are not normalized. Figures 2.2 and 2.3 shows the energy spectra for $L = 3$ and $L = 4$, respectively.

All the eigenvalues for $L = 3$ are double degenerated. The degeneracies correspond

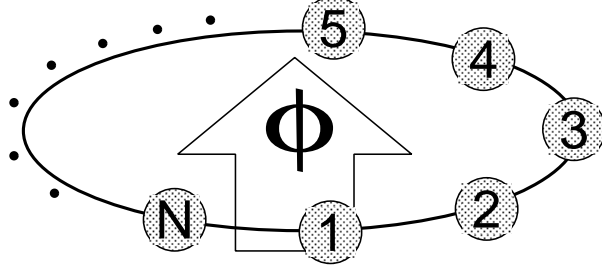


Figure 2.1: Schematic picture of the XXZ spin chain described by Eq. (2.1).

Table 2.1: The eigenvectors and the eigenvalues for the 3-site XXZ chain. The numbers in the first column “No.” correspond to the numbers in Fig. 2.2.

No.	Eigenvectors	Eigenvalues
1	$ \uparrow\uparrow\uparrow\rangle$	$(J/4) \cdot 3\Delta$
2	$ \downarrow\downarrow\downarrow\rangle$	(double degenerated)
3	$e^{\frac{\phi i}{3}} \uparrow\uparrow\downarrow\rangle + \uparrow\downarrow\uparrow\rangle + e^{-\frac{\phi i}{3}} \downarrow\uparrow\uparrow\rangle$	$(J/4)\{4 \cos[\phi/3] - \Delta\}$
4	$e^{\frac{\phi i}{3}} \uparrow\downarrow\downarrow\rangle + \downarrow\uparrow\downarrow\rangle + e^{-\frac{\phi i}{3}} \downarrow\downarrow\uparrow\rangle$	(double degenerated)
5	$e^{\frac{\phi-\pi}{3}i} \uparrow\uparrow\downarrow\rangle - \uparrow\downarrow\uparrow\rangle + e^{-\frac{\phi-\pi}{3}i} \downarrow\uparrow\uparrow\rangle$	$(J/4)\{-4 \cos[(\phi - \pi)/3] - \Delta\}$
6	$e^{\frac{\phi-\pi}{3}i} \uparrow\downarrow\downarrow\rangle - \downarrow\uparrow\downarrow\rangle + e^{-\frac{\phi-\pi}{3}i} \downarrow\downarrow\uparrow\rangle$	(double degenerated)
7	$e^{\frac{\phi+\pi}{3}i} \uparrow\uparrow\downarrow\rangle - \uparrow\downarrow\uparrow\rangle + e^{-\frac{\phi+\pi}{3}i} \downarrow\uparrow\uparrow\rangle$	$(J/4)\{-4 \cos[(\phi + \pi)/3] - \Delta\}$
8	$e^{\frac{\phi+\pi}{3}i} \uparrow\downarrow\downarrow\rangle - \downarrow\uparrow\downarrow\rangle + e^{-\frac{\phi+\pi}{3}i} \downarrow\downarrow\uparrow\rangle$	(double degenerated)

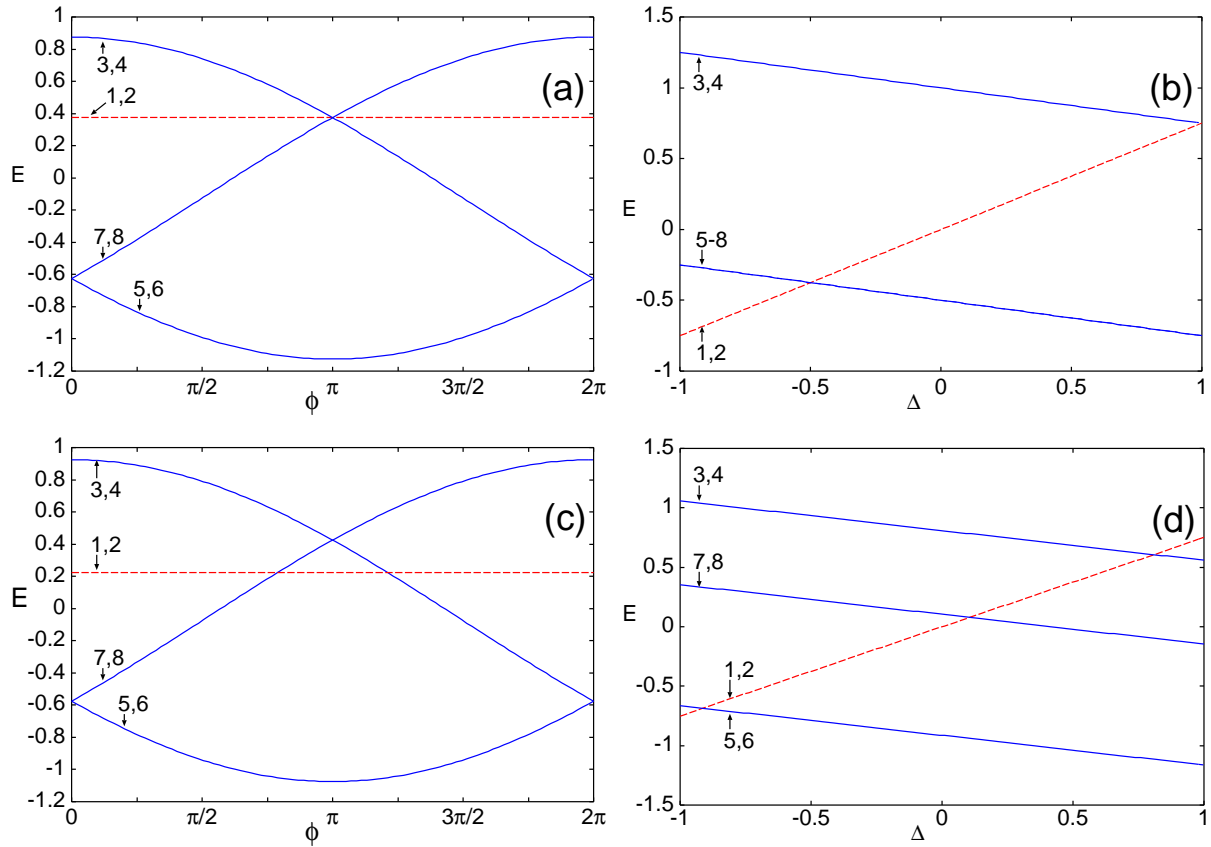


Figure 2.2: Energy spectra of XXZ spin chains on 3 sites. The numbers in the figures correspond to “No.” of Table 2.1. Color of the lines indicates $|S_{\text{tot}}^z|$: Red dashed lines, $|S_{\text{tot}}^z| = 3/2$; Blue solid lines, $|S_{\text{tot}}^z| = 1/2$. The values of the fixed parameters are the following: (a) $\Delta = \cos(\pi/3)$, (b) $\phi = 0$, (c) $\Delta = 0.3$, (d) $\phi = 0.6\pi$.

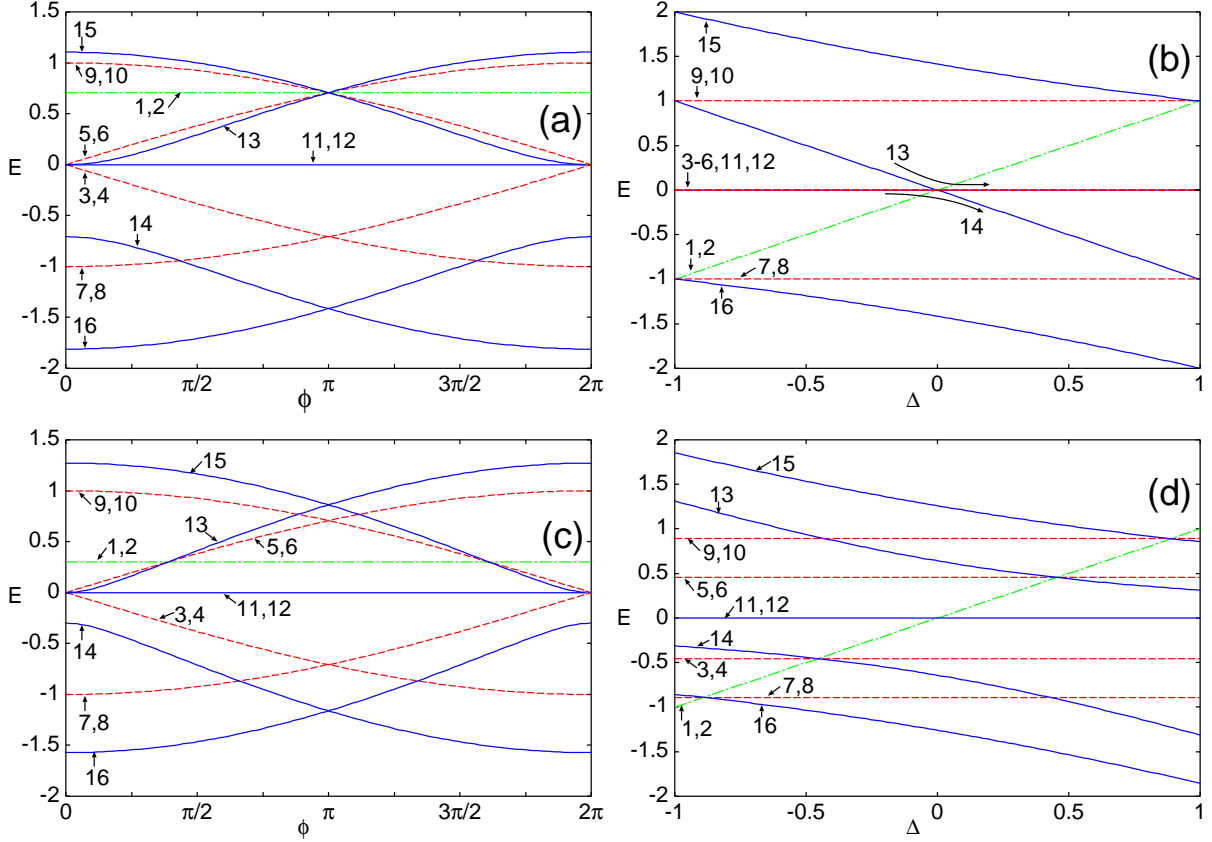


Figure 2.3: Energy spectra of XXZ spin chains on 4 sites. The numbers in the figures correspond to “No.” of Table 2.2. Color of the lines indicates $|S_{\text{tot}}^z|$: Green chained lines, $|S_{\text{tot}}^z| = 2$; Red dashed lines, $|S_{\text{tot}}^z| = 1$; Blue solid lines, $S_{\text{tot}}^z = 0$. The values of the fixed parameters are the following: (a) $\Delta = \cos(\pi/4)$, (b) $\phi = 0$, (c) $\Delta = 0.3$, (d) $\phi = 0.6\pi$.

to the Kramers doublets. Examples of the energy spectral flows for $L = 3$ are shown in Fig. 2.2. The left and right figures are drawn for the fixed values of Δ and ϕ , respectively. In Fig. 2.2(a), where $\Delta = \cos(\pi/3)$, a sixfold degenerated point exists at $\phi = \pi$. In Fig. 2.2(b), where $\phi = 0$, a sixfold degenerated point exists at $\Delta = -0.5 = -\cos(\pi/3)$. There are not sixfold degenerated points for general cases, whose examples are shown in Figs. 2.2(c) and 2.2(d). From Fig. 2.2 and the Table 2.1, we find that sixfold degenerated points appear for $(\Delta, \phi) = (-\cos \frac{\pi}{3}, 0)$ and $(\cos \frac{\pi}{3}, \pi)$. We note that multi-fold degeneracies appear when the system has many symmetries. Figures 2.2(a) and 2.2(b) are for the cases where the system has many symmetries, while Figs. 2.2(c) and 2.2(d) are for the cases where the system has fewer symmetries.

When $L = 4$, all the eigenvalues for $|S_{\text{tot}}^z| = 2$ and $|S_{\text{tot}}^z| = 1$ are double degenerated but not for $S_{\text{tot}}^z = 0$. It is a nature of even-site spin chains under zero magnetic field. Examples of the energy spectral flows for $L = 4$ are shown in Fig. 2.3. The left and

Table 2.2: The eigenvectors and the eigenvalues for the 4-site XXZ chains. The numbers in the first column “No.” correspond to the numbers in Fig. 2.3.

No.	Eigenvectors	Eigenvalues
1	$ \uparrow\uparrow\uparrow\uparrow\rangle$	$J\Delta$
2	$ \downarrow\downarrow\downarrow\downarrow\rangle$	(double degenerated)
3	$e^{\phi i} \uparrow\uparrow\uparrow\downarrow\rangle + e^{(\frac{3}{4}\phi - \frac{\pi}{2})i} \uparrow\uparrow\downarrow\uparrow\rangle - e^{\frac{\phi i}{2}} \uparrow\downarrow\uparrow\uparrow\rangle + e^{(\frac{\phi}{4} + \frac{\pi}{2})i} \downarrow\uparrow\uparrow\uparrow\rangle$	$(J/2)(-2\sin(\phi/4))$
4	$e^{\phi i} \uparrow\downarrow\downarrow\downarrow\rangle + e^{(\frac{3}{4}\phi - \frac{\pi}{2})i} \downarrow\downarrow\downarrow\downarrow\rangle - e^{\frac{\phi i}{2}} \downarrow\downarrow\uparrow\downarrow\rangle + e^{(\frac{\phi}{4} + \frac{\pi}{2})i} \downarrow\downarrow\downarrow\uparrow\rangle$	(double degenerated)
5	$e^{\phi i} \uparrow\uparrow\uparrow\downarrow\rangle + e^{(\frac{3}{4}\phi + \frac{\pi}{2})i} \uparrow\uparrow\downarrow\uparrow\rangle - e^{\frac{\phi i}{2}} \uparrow\downarrow\uparrow\uparrow\rangle + e^{(\frac{\phi}{4} - \frac{\pi}{2})i} \downarrow\uparrow\uparrow\uparrow\rangle$	$(J/2)(2\sin(\phi/4))$
6	$e^{\phi i} \uparrow\downarrow\downarrow\downarrow\rangle + e^{(\frac{3}{4}\phi + \frac{\pi}{2})i} \downarrow\downarrow\downarrow\downarrow\rangle - e^{\frac{\phi i}{2}} \downarrow\downarrow\uparrow\downarrow\rangle + e^{(\frac{\phi}{4} - \frac{\pi}{2})i} \downarrow\downarrow\downarrow\uparrow\rangle$	(double degenerated)
7	$e^{\phi i} \uparrow\uparrow\uparrow\downarrow\rangle - e^{\frac{3\phi i}{4}} \uparrow\uparrow\downarrow\uparrow\rangle + e^{\frac{\phi i}{2}} \uparrow\downarrow\uparrow\uparrow\rangle - e^{\frac{\phi i}{4}} \downarrow\uparrow\uparrow\uparrow\rangle$	$(J/2)(-2\cos(\phi/4))$
8	$e^{\phi i} \uparrow\downarrow\downarrow\downarrow\rangle - e^{\frac{3\phi i}{4}} \downarrow\downarrow\downarrow\downarrow\rangle + e^{\frac{\phi i}{2}} \downarrow\downarrow\uparrow\downarrow\rangle - e^{\frac{\phi i}{4}} \downarrow\downarrow\downarrow\uparrow\rangle$	(double degenerated)
9	$e^{\phi i} \uparrow\uparrow\uparrow\downarrow\rangle + e^{\frac{3\phi i}{4}} \uparrow\uparrow\downarrow\uparrow\rangle + e^{\frac{\phi i}{2}} \uparrow\downarrow\uparrow\uparrow\rangle + e^{\frac{\phi i}{4}} \downarrow\uparrow\uparrow\uparrow\rangle$	$(J/2)(2\cos(\phi/4))$
10	$e^{\phi i} \uparrow\downarrow\downarrow\downarrow\rangle + e^{\frac{3\phi i}{4}} \downarrow\downarrow\downarrow\downarrow\rangle + e^{\frac{\phi i}{2}} \downarrow\downarrow\uparrow\downarrow\rangle + e^{\frac{\phi i}{4}} \downarrow\downarrow\downarrow\uparrow\rangle$	(double degenerated)
11	$ \uparrow\downarrow\downarrow\uparrow\rangle - \downarrow\uparrow\uparrow\downarrow\rangle$	0
12	$e^{\frac{\phi i}{2}} \uparrow\uparrow\downarrow\downarrow\rangle - e^{-\frac{\phi i}{2}} \downarrow\downarrow\uparrow\uparrow\rangle$	(double degenerated)
13	$(e^{\phi i} - e^{\frac{\phi i}{2}}) \uparrow\uparrow\downarrow\downarrow\rangle - \lambda_{13}e^{\frac{\phi i}{2}} \uparrow\downarrow\uparrow\uparrow\rangle + (1 - e^{\frac{\phi i}{2}}) \uparrow\downarrow\downarrow\uparrow\rangle$ $+ (1 - e^{\frac{\phi i}{2}}) \downarrow\uparrow\uparrow\downarrow\rangle + \lambda_{13} \downarrow\uparrow\downarrow\uparrow\rangle + (1 - e^{-\frac{\phi i}{2}}) \downarrow\downarrow\uparrow\uparrow\rangle$ (Here, $\lambda_{13} = -\Delta + \sqrt{4 - 4\cos\frac{\phi}{2} + \Delta^2}$.)	$(J/2) \{-\Delta + [4 - 4\cos(\phi/2) + \Delta^2]^{1/2}\}$
14	$(e^{\phi i} - e^{\frac{\phi i}{2}}) \uparrow\uparrow\downarrow\downarrow\rangle - \lambda_{14}e^{\frac{\phi i}{2}} \uparrow\downarrow\uparrow\uparrow\rangle + (1 - e^{\frac{\phi i}{2}}) \uparrow\downarrow\downarrow\uparrow\rangle$ $+ (1 - e^{\frac{\phi i}{2}}) \downarrow\uparrow\uparrow\downarrow\rangle + \lambda_{14} \downarrow\uparrow\downarrow\uparrow\rangle + (1 - e^{-\frac{\phi i}{2}}) \downarrow\downarrow\uparrow\uparrow\rangle$ (Here, $\lambda_{14} = -\Delta - \sqrt{4 - 4\cos(\phi/2) + \Delta^2}$.)	$(J/2) \{-\Delta - [4 - 4\cos(\phi/2) + \Delta^2]^{1/2}\}$
15	$(e^{\phi i} + e^{\frac{\phi i}{2}}) \uparrow\uparrow\downarrow\downarrow\rangle + \lambda_{15}e^{\frac{\phi i}{2}} \uparrow\downarrow\uparrow\uparrow\rangle + (1 + e^{\frac{\phi i}{2}}) \uparrow\downarrow\downarrow\uparrow\rangle$ $+ (1 + e^{\frac{\phi i}{2}}) \downarrow\uparrow\uparrow\downarrow\rangle + \lambda_{15} \downarrow\uparrow\downarrow\uparrow\rangle + (1 + e^{-\frac{\phi i}{2}}) \downarrow\downarrow\uparrow\uparrow\rangle$ (Here, $\lambda_{15} = -\Delta + \sqrt{4 + 4\cos(\phi/2) + \Delta^2}$.)	$(J/2) \{-\Delta + [4 + 4\cos(\phi/2) + \Delta^2]^{1/2}\}$
16	$(e^{\phi i} + e^{\frac{\phi i}{2}}) \uparrow\uparrow\downarrow\downarrow\rangle + \lambda_{16}e^{\frac{\phi i}{2}} \uparrow\downarrow\uparrow\uparrow\rangle + (1 + e^{\frac{\phi i}{2}}) \uparrow\downarrow\downarrow\uparrow\rangle$ $+ (1 + e^{\frac{\phi i}{2}}) \downarrow\uparrow\uparrow\downarrow\rangle + \lambda_{16} \downarrow\uparrow\downarrow\uparrow\rangle + (1 + e^{-\frac{\phi i}{2}}) \downarrow\downarrow\uparrow\uparrow\rangle$ (Here, $\lambda_{16} = -\Delta - \sqrt{4 + 4\cos(\phi/2) + \Delta^2}$.)	$(J/2) \{-\Delta - [4 + 4\cos(\phi/2) + \Delta^2]^{1/2}\}$

right figures are drawn for the fixed values of Δ and ϕ , respectively. In Fig. 2.3(a), where $\Delta = \cos(\pi/4)$, an eightfold degenerated point exists at $\phi = \pi$. For general values of Δ , the eightfold degenerated point vanishes and a pair of fivefold degenerated points appears [see Fig. 2.3(c)]. The coordinates of the degenerated points depend on the value of Δ . In Fig. 2.3(b), where $\phi = 0$, a tenfold and two fivefold degenerated points exist at $\Delta = 0$ and at $\Delta = \pm 1$, respectively. For general values of ϕ , the ten fold degenerated point vanishes and an additional pair of fivefold degenerated points appears [see Fig. 2.3(d)].

In this way, we find many degeneracies at several points where the parameters, Δ and ϕ , correspond to some particular values. Some of the particular values are independent of the lattice size L (for example, $\phi = 0$ or $\Delta = 0$). Other are dependent on L (for example, $\Delta = \cos(\pi/3)$ or $\Delta = \cos(\pi/4)$).

The analytical forms of the eigenvalues are useful to discuss the behavior of crossing points in the energy spectra. In Fig. 2.3, for example, Line 1,2, Line 5,6 and Line 13 seem to be always crossing together at one point. We prove that the expectation is right from Table 2.2. At the crossing point of Line 1,2 and Line 5,6,

$$\Delta = \sin \frac{\phi}{4}. \quad (2.2)$$

Here, we assume $J \neq 0$. On the other hand, at the crossing point of Line 1,2 and Line 13,

$$\Delta = \frac{1}{2} \left\{ -\Delta + \left[4 - 4 \cos \frac{\phi}{2} + \Delta^2 \right]^{\frac{1}{2}} \right\}. \quad (2.3)$$

Namely,

$$3\Delta = \left[4 - 4 \cos \frac{\phi}{2} + \Delta^2 \right]^{\frac{1}{2}}. \quad (2.4)$$

Here we notice that $\Delta \geq 0$. If each hand side of Eq. (2.4) is squared, then we have

$$\Delta^2 = \frac{1}{2} \left(1 - \cos \frac{\phi}{2} \right) \quad (2.5)$$

$$= \sin^2 \frac{\phi}{4}. \quad (2.6)$$

Since $\Delta \geq 0$, Eq. (2.6) is reduced to

$$\Delta = \sin \frac{\phi}{4}. \quad (2.7)$$

We now find that Eq. (2.2) coincides with Eq. (2.7). In other words, the crossing point of Line 1,2 and Line 5,6 coincides with that of Line 1,2 and Line 13. Therefore those lines are always crossing together at one point.

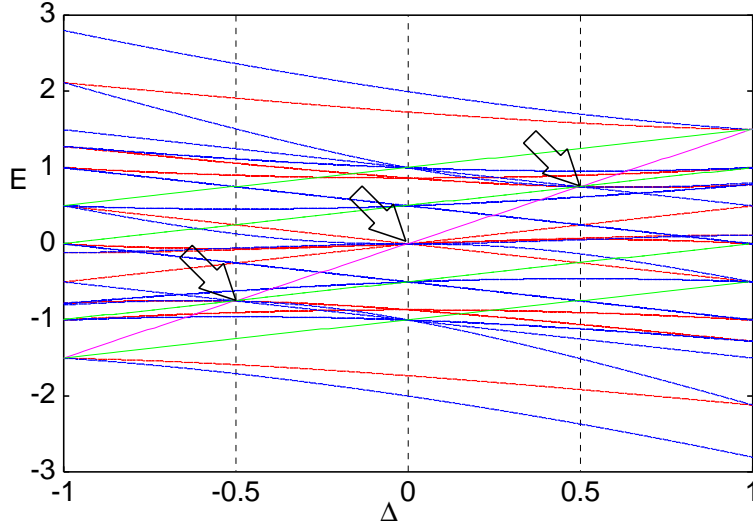


Figure 2.4: Energy spectra of the XXZ spin chain on 6 sites (reprinted from Ref. [13]). The arrows indicate the points relating to the sl_2 loop algebra symmetry. Color of the lines indicates the value of $|S_{\text{tot}}^z|$: Magenta, $|S_{\text{tot}}^z| = 3$; Green, $|S_{\text{tot}}^z| = 2$; Red, $|S_{\text{tot}}^z| = 1$; Blue, $S_{\text{tot}}^z = 0$.

2.2 The spectral flow of the XXZ spin chain on 6 sites.

Figure 2.4 is the energy spectral flow for $L = 6$, which is calculated numerically. Here, periodic boundary conditions are imposed: $\phi = 0$. All the spectra for $|S_{\text{tot}}^z| \neq 0$ are, at least, double degenerated when $L = 6$.

The arrow in Fig. 2.4 indicates the points which is related to the sl_2 loop algebra symmetry. As mentioned in Chapter 1, the sl_2 loop algebra symmetry leads to many spectral degeneracies. The dimensions of degenerate eigenspaces are 12 at $\Delta = \pm 0.5$ and 16 at $\Delta = 0$.

Chapter 3

Level Bifurcation

Branches such as bifurcations or multiple branches are observed in the flow of eigenvalues for the inhomogeneous transfer matrix of the XXZ spin chain [14]. The spectral flow for the XXZ anisotropic parameter Δ is obtained by directly diagonalizing the transfer matrix in the regime: $-1 \leq \Delta \leq 1$, where the inhomogeneous transfer matrix is real. The branches are considered as novel spectral behaviors, which are not decomposed into simple superpositions of level crossings. We may call them *level bifurcations*. We also observe that no branches appear in the homogeneous case. The appearance of some of the branches are confirmed through the Bethe ansatz method. We note that an inhomogeneous transfer matrix plays a central role in the exact calculation of thermodynamic quantities at finite temperatures for the XXZ spin chain (for example, see Ref. [19]). We believe that the present study will shed some light on the spectral degeneracies in quantum systems.

3.1 Transfer matrix

Let us introduce the transfer matrix of the XXZ spin chain for both homogeneous and inhomogeneous cases [20, 21]. We define the L operator [21, 22] of the XXZ spin chain by

$$L_j(z) = \begin{pmatrix} \sin(zI_j + \nu\sigma_j^z) & \sin(2\nu)\sigma_j^- \\ \sin(2\nu)\sigma_j^+ & \sin(zI_j - \nu\sigma_j^z) \end{pmatrix}. \quad (3.1)$$

Here, I_j is the identity matrix, σ_j^\pm is given by $\sigma_j^\pm = (\sigma_j^x \pm i\sigma_j^y)/2$, and the real parameter ν is related to the parameter Δ by

$$\Delta = -\cos(2\nu) \quad \left(0 \leq \nu \leq \frac{\pi}{2}\right). \quad (3.2)$$

In this work, we consider only the massless regime of the XXZ spin chain: $-1 \leq \Delta \leq 1$. All the nonzero matrix elements of $L(z)$ are real and positive if z satisfies the condition: $-\nu < z < \nu$. We define the inhomogeneous transfer matrix $\tau(w; \{\zeta_j\})$ acting on L sites

by

$$\begin{aligned} \tau(w; \{\zeta_j\}) \\ = \text{Tr}(L_L(w + \zeta_L) \dots L_2(w + \zeta_2)L_1(w + \zeta_1)). \end{aligned} \quad (3.3)$$

Here, the parameters $\zeta_1, \zeta_2, \dots, \zeta_L$ are called inhomogeneous parameters. The symbol $\{\zeta_j\}$ denotes the set of ζ_j 's. When all ζ_j 's take the same value, the transfer matrix is called *homogeneous*. When they do not, it is called *inhomogeneous*. The Hamiltonian, Eq. (1.7), of the XXZ spin chain is given by the logarithmic derivative of the homogeneous transfer matrix [20]:

$$\left. \frac{d}{dw} \ln \tau \right|_{w=-\zeta+\nu} \propto \mathcal{H} + \text{constant}, \quad (3.4)$$

where the inhomogeneous parameters have the same value: $\zeta_j = \zeta$ for $j = 1, 2, \dots, L$.

3.2 Eigenvalues of the transfer matrix obtained by numerical diagonalization

Let us now discuss numerical results on the spectrum of the transfer matrix. Hereafter we normalize the transfer matrix so that the eigenvalue is given by 1 for the “vacuum” state in which all spins are up. We also set $w = 0$ for the transfer matrix. We consider four cases for setting ζ_j 's: three inhomogeneous cases and one homogeneous case. The equations for the four cases, which correspond to Fig. 3.1, are the following:

$$\begin{aligned} \text{(a)} \quad \zeta_j &= k_j \nu && (0 < k_j < 1; k_j \text{'s are arbitrarily chosen.}) \\ \text{(b)} \quad \zeta_j &= \frac{j}{L} \cdot k_0 \nu \\ \text{(c)} \quad \zeta_j &= (-1)^j \cdot k_0 \nu \\ \text{(d)} \quad \zeta_j &= k_0 \nu && (\text{homogeneous case}) \end{aligned} \quad (3.5)$$

The real parts of eigenvalues of the transfer matrices $\tau(0; \{\zeta_j\})$ shown in Fig. 3.1 are obtained by numerically diagonalizing them for $L = 6$. In Fig. 3.1, we set $k_0 = 0.8$ in Eq. (3.5). We observe branches in the inhomogeneous cases. On the other hand, there is no branch in the homogeneous case, as shown in Fig. 3.1(d).

Figure 3.2 shows that Case (b) in Eq. (3.5) is a special inhomogeneous case. In Case (b), two branching points lie on the same line, as shown in Fig. 3.2(b). On the contrary, two branching points are not on the same line in Cases (a) or (c), as evident in Figs. 3.2(a) and (c).

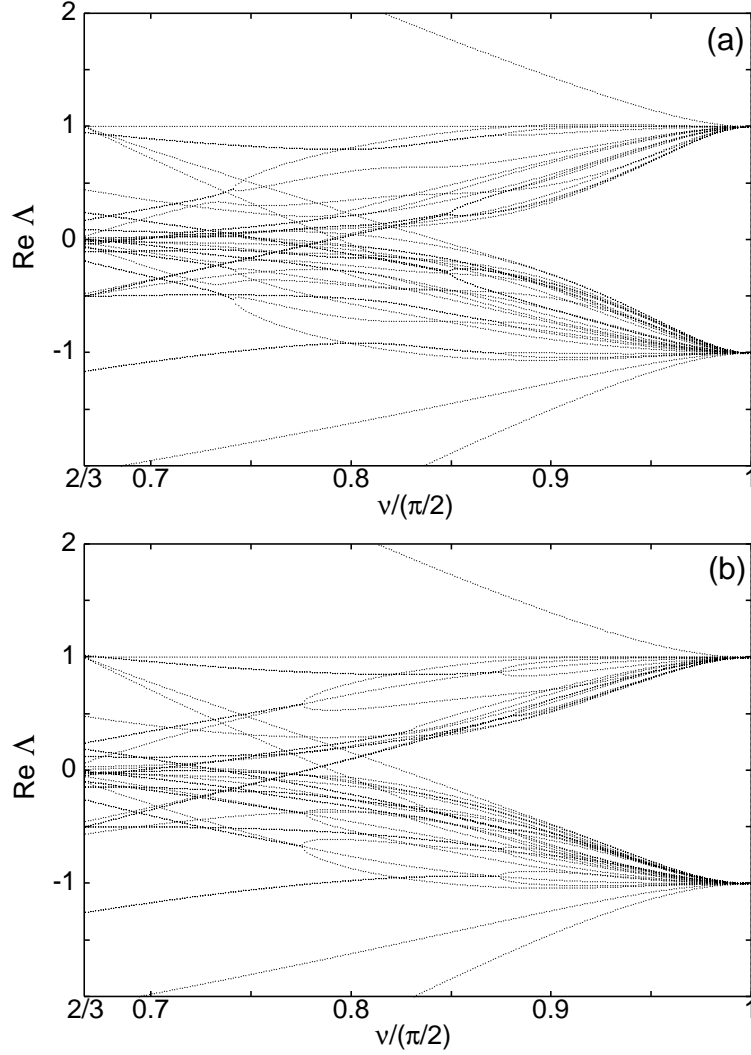
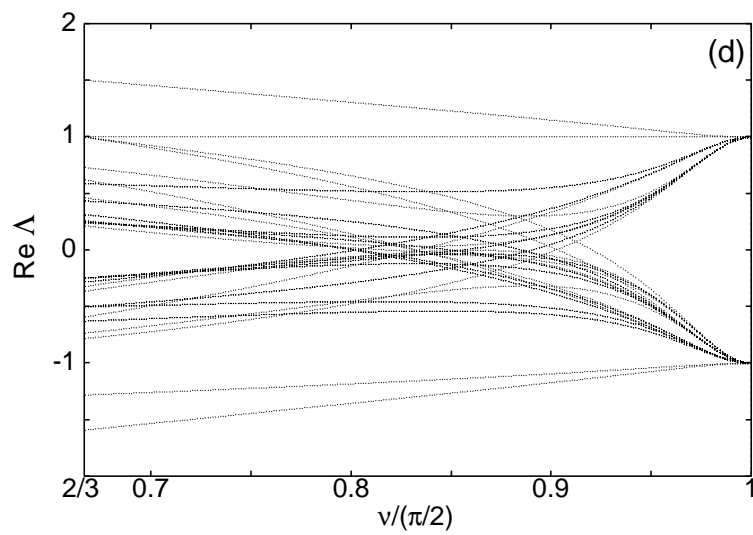
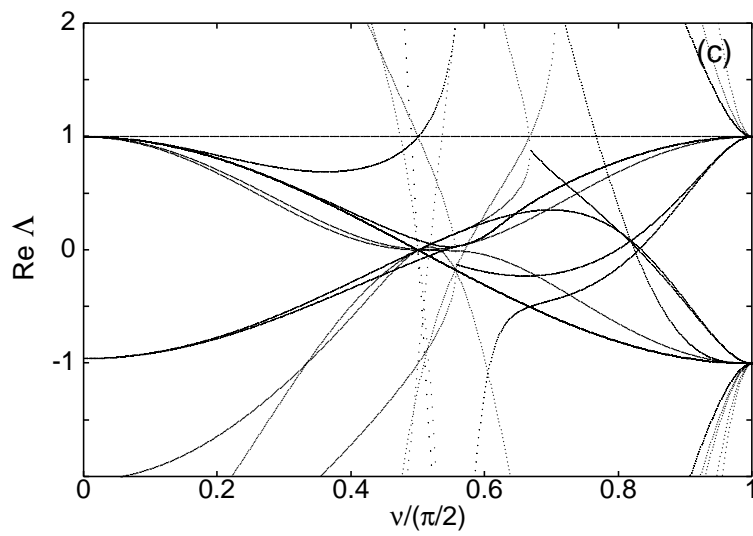


Figure 3.1: The real part of the eigenvalues of the transfer matrices for $L = 6$ (partly reprinted from Ref. [14]). Labels (a)-(d) correspond to the labels (a)-(d) in Eq. (3.5). The spectral flows in inhomogeneous cases have many branches, which do not appear in the homogeneous case.



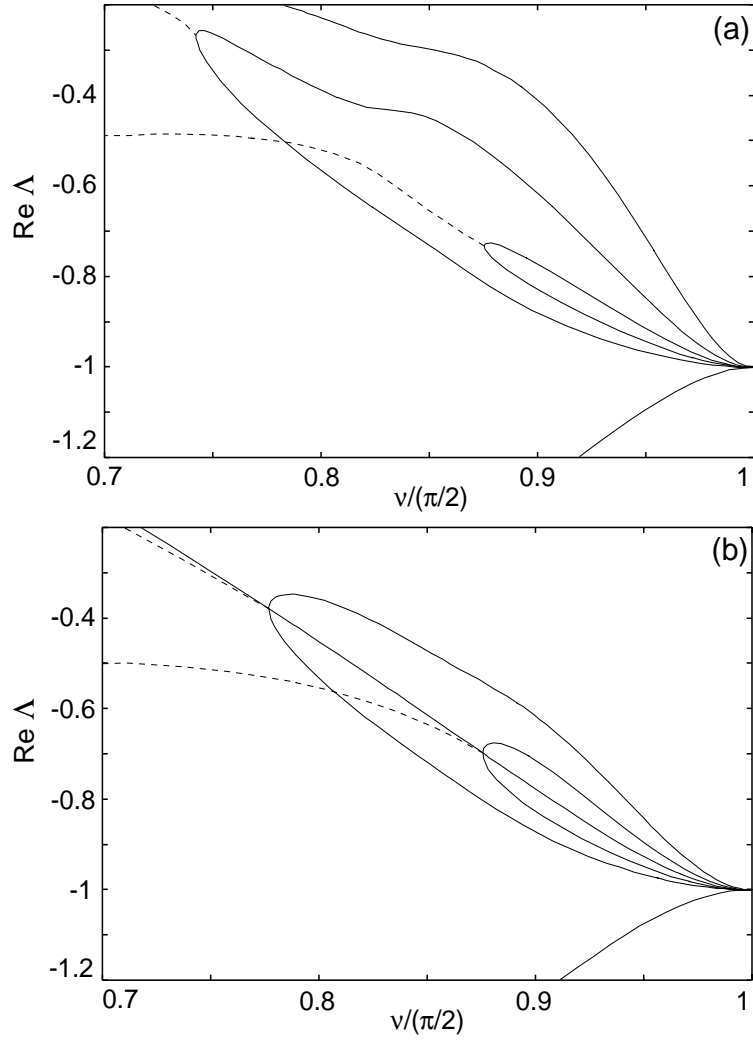


Figure 3.2: Graphs (a) and (b) show the magnified spectral flow in the sector of one down spin, which has been given in Figs. 3.1(a) and 3.1(b), respectively (reprinted from Ref. [14]). The solid lines denote single real eigenvalues, and the dashed lines denote real parts of complex eigenvalues.

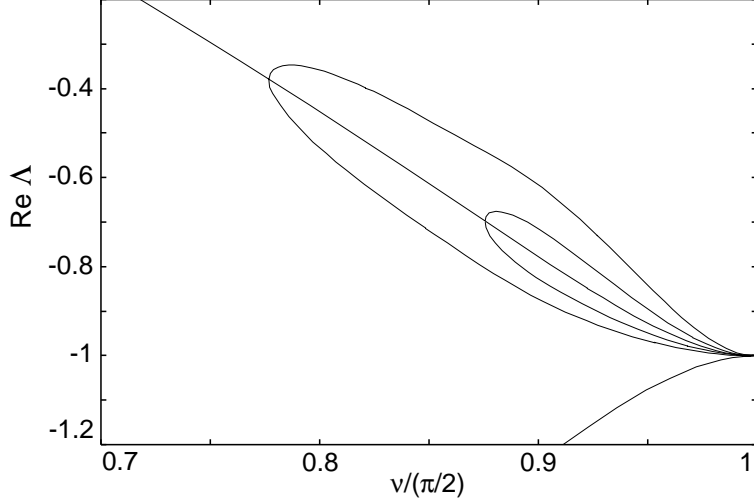


Figure 3.3: The magnified spectral flow for $L = 6$ given by real solutions to the Bethe ansatz equation, Eq. (3.6) (reprinted from Ref. [14]).

3.3 Eigenvalues of the transfer matrix obtained through the Bethe ansatz method

Let us confirm the appearance of spectral branches by an independent method. First, we show that the branches of the regular-interval case, i.e. Case (b) in Eq. (3.5), can also be obtained by the Bethe ansatz method. For simplicity, we consider only the case of one down spin. For the inhomogeneous case, according to Refs. [20, 21] the Bethe ansatz equation with one down spin is given by

$$\prod_{j=1}^L \frac{\sin(t_1 + \zeta_j + \nu)}{\sin(t_1 + \zeta_j - \nu)} = 1. \quad (3.6)$$

The solution t_1 leads to the eigenvalue of the transfer matrix:

$$\Lambda(t_1) = \frac{1}{A_{\text{norm}}} \left(\frac{\sin(t_1 + 2\nu)}{\sin(t_1)} \prod_{j=1}^L \sin(\zeta_j + \nu) + \frac{\sin(t_1 - 2\nu)}{\sin(t_1)} \prod_{j=1}^L \sin(\zeta_j - \nu) \right). \quad (3.7)$$

Here, A_{norm} denotes the normalization factor, which corresponds to the “vacuum” state eigenvalue:

$$A_{\text{norm}} = \prod_{j=1}^L \sin(\zeta_j + \nu) + \prod_{j=1}^L \sin(\zeta_j - \nu). \quad (3.8)$$

Now let us discuss numerical solutions to the Bethe ansatz equation, Eq. (3.6). We introduce a function of rapidity t in the following:

$$f(t) = \prod_{j=1}^L \sin(t + \zeta_j + \nu) - \prod_{j=1}^L \sin(t + \zeta_j - \nu). \quad (3.9)$$

We can easily obtain real solutions to the equation: $f(t) = 0$, for instance, by the Newton method. Substituting real solutions of Eq. (3.6) for Eq. (3.7), we obtain the eigenvalues of the transfer matrix by the Bethe ansatz method. We note that Eq. (3.6) has L singular points at the zeros of $\prod_{j=1}^L \sin(t + \zeta_j - \nu)$ as a function of t .

We see in Fig. 3.3 that the same solid lines given in Fig. 3.2(b) are indeed obtained with the Bethe ansatz method. The numerical differences between the two methods are less than 10^{-7} for the eigenvalues of the transfer matrix. Thus, we may conclude that they are consistent. We have not reconstructed the dashed lines in Fig. 3.2(b) because we can obtain only the real (not complex) solutions of Eq. (3.6) by the above method.

3.4 Discussion

Let us discuss the behavior of branching points for Case (b) in Eq. (3.5). Sending the inhomogeneous parameters continually to a fixed value, we observe that the branching points in the spectral flow in Fig. 3.1(b) gradually move to the large- ν direction. When the branching points approach the XXX point ($\nu = \pi/2$), i.e. the homogeneous point, the branches finally vanish as shown in Fig. 3.4. Figure 3.4 shows how the branching points for Case (b) behave. Here, we rewrite Case (b) in Eq. (3.5) as

$$\zeta_j = \left(1 - \frac{j-1}{L}k_1\right) k_0\nu. \quad (3.10)$$

When $k_1 = 1$, Eq. (3.10) is efficiently equal to Case (b) in Eq. (3.5). When $k_1 = 0$, Eq. (3.10) corresponds to the homogeneous case. In Fig. 3.4, the values of $\nu/(\pi/2)$ at the branching points, which are calculated through the Bethe ansatz method, are shown as a function of k_1 . The solid lines and the broken lines in Fig. 3.4 correspond to the smaller- ν (first) branching points and the larger- ν (second) branching points. Furthermore, in Fig. 3.4(b) we show the fitting lines to the values of $\nu/(\pi/2)$ at the branching points. The fitting function of the lines in Fig. 3.4(b) is given by

$$\frac{\nu}{\pi/2} = \frac{1}{1 + ak_0k_1}, \quad (3.11)$$

where $a = 0.359$ for the first branching point, $a = 0.178$ for the second branching point, and $k_0 = 0.8$ for both points.

The spectral branches are important when we investigate the solutions of the Bethe ansatz equations. In fact, it is nontrivial to solve the Bethe ansatz equations at a spectral branch. Here, we recall Fig. 3.2(a). Two solid lines correspond to two real solutions of the Bethe ansatz equation, Eq. (3.6), while the dashed line corresponds to the real part of two complex conjugate solutions of Eq. (3.6). Thus, two real solutions should be converted into complex solutions at the branching point, where the Bethe ansatz equations may be singular.

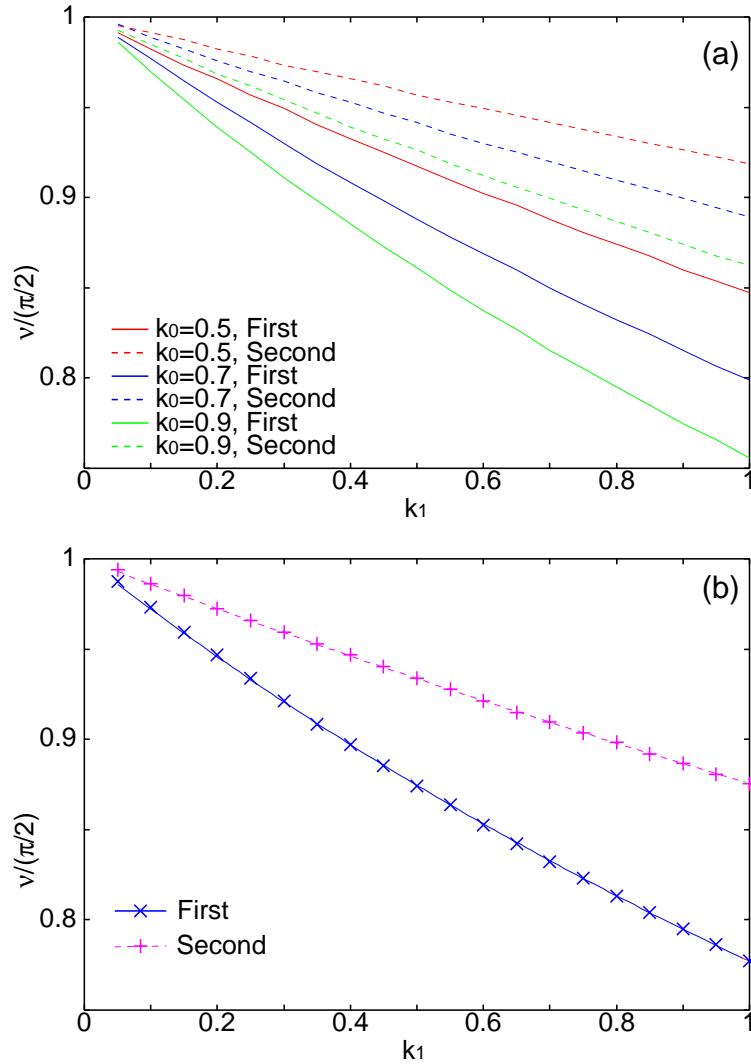


Figure 3.4: Branching points for Case (b) with k_1 varying in Eq. (3.10). (a) Solid lines are for the smaller- ν (first) branching points; Broken lines are for the larger- ν (second) branching points. (b) Crosses are for the branching points when $k_0 = 0.8$. The solid line and the dashed line are the fitting line to the crosses, where the fitting function is given by Eq. (3.11).

It is surprising that spectral branches appear in Case (c) in Eq. (3.5). The system has the translational invariance in that case as well as the homogeneous case. We should say that the expectation of Ref. [14] is incorrect: the appearance of spectral branches could be related to the breakdown of the translational symmetry of the system. The expectation has come from an ordinary interpretation. In other words, the level bifurcations are nontrivial and extraordinary phenomena.

Chapter 4

Level Statistics

We have studied level statistics for XXZ spin chains with next-nearest-neighbor (NNN) couplings [15, 17] or with a random magnetic field [16]. Evaluating the level-spacing distribution, the spectral rigidity and the number variance, we confirm the correspondence between non-integrability and Wigner behavior in the spectrum. We show how the level statistics of the finite-size systems depends on the anisotropy parameter and the NNN coupling parameter or the strength of the magnetic field.

4.1 Preliminaries

Statistical properties of energy levels have been studied for various physical systems in terms of the random matrix theory (RMT). In the RMT, we consider a large Hamiltonian whose elements are random variables with given probability laws. The statistical behavior of the energy levels depends only on the symmetry of the Hamiltonian [23]. For systems with time-reversal invariance, the Gaussian orthogonal ensemble (GOE) is appropriate for the description of the Hamiltonian matrices. For systems having invariance under time-reversal but no rotational symmetry, the Gaussian symplectic ensemble (GSE) is appropriate. For systems without time-reversal invariance, the Gaussian unitary ensemble (GUE) is appropriate. The RMT analysis was performed also in the view of semi-classical pictures of quantum many-body systems [24, 25]. When the classical motion is integrable, level-clustering can occur. Then the level-spacing distribution is the negative exponential characteristic of Poisson processes [24]. Chaotic motion in the classical system is associated with level repulsion and with the level statistics characteristic of GOE [25].

For quantum many-body systems, the RMT analysis has been applied to characterizing quantum chaos and to investigating the integrability of a system. For quantum spin systems, we adopt a definition of integrability by the Bethe ansatz: an integrable model is exactly solvable by the Bethe ansatz. Since a pioneering work [26], the following

conjecture has been widely accepted: If a given Hamiltonian is integrable by the Bethe ansatz, the level-spacing distribution should be described by the Poisson distribution:

$$P_{\text{Poi}}(s) = \exp(-s). \quad (4.1)$$

If it is nonintegrable, the level-spacing distribution should be given by the Wigner distribution:

$$P_{\text{Wig}}(s) = \frac{\pi s}{2} \exp\left(-\frac{\pi s^2}{4}\right). \quad (4.2)$$

In fact, the above conjecture has been numerically confirmed for many quantum spin systems such as correlated spin systems [15, 17, 26, 27, 28, 29, 30, 31, 32, 33, 34, 35] and disordered spin systems [16, 36, 37, 38, 39]. In the Anderson model of disordered systems, $P_{\text{Poi}}(s)$ and $P_{\text{Wig}}(s)$ characterize the localized and the metallic phases, respectively [40].

Here we note that the Wigner distribution, Eq. (4.2), is commonly known as the Wigner surmise for GOE. In this chapter, we use the word ‘‘Wigner behavior’’ instead of ‘‘GOE behavior’’.

It should be important to study statistical properties of energy levels for XXZ spin chains. The XXZ spin chains are closely related to the most important families of integrable spin systems through the integrable point as mentioned in Chapter 1. On the other hand, XXZ spin chains are also extended into nonintegrable systems quite naturally with NNN couplings or a random magnetic field. We can therefore expect that the RMT analysis of the XXZ spin chains could be important in discussing level statistics for other quantum systems that would have some connection to an integrable system.

The organization of this chapter is as follows: In Sec. 4.2, we describe our models and numerical methods. We explain the details especially about desymmetrization and unfolding. Definitions of level-spacing distribution, spectral rigidity and numerical variance are also described in the section. In Sec. 4.3, we discuss level statistics of integrable XXZ spin chains in both a standard case and a special symmetrical case. In Sec. 4.4, the characteristic behavior of level statistics is discussed for NNN coupled XXZ spin chains. First we confirm the correspondence between non-integrability and Wigner behavior. Then we show how the behavior of level statistics changes due to mixed symmetry and finite-size effects. We also show that the characteristic behavior of level statistics does not depend in the energy range. In Sec. 4.5, the behavior of level statistics is discussed for XXZ spin chains under random magnetic field. We show how the behavior of level statistics depends on the anisotropy parameter, the magnetic field and the system size. We also discuss the correspondence between the Anderson model of disordered systems and our model. Finally, we summarize this chapter in Sec. 4.6.

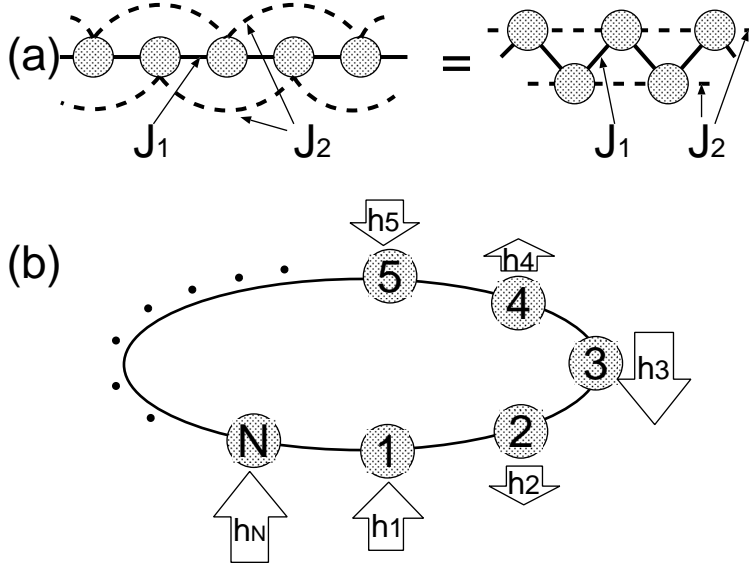


Figure 4.1: Schematic pictures of the models. (a) XXXZ spin chain with next-nearest-neighbor couplings. It is also called “zig-zag chain”. (b) XXZ spin chain with a random magnetic field.

4.2 Models and numerical procedure

4.2.1 Models

Let us give the Hamiltonian of a XXZ spin chain with NNN couplings on L sites by

$$\mathcal{H}_{\text{NNN}} = J_1 \sum_{j=1}^L (S_j^x S_{j+1}^x + S_j^y S_{j+1}^y + \Delta_1 S_j^z S_{j+1}^z) + J_2 \sum_{j=1}^L (S_j^x S_{j+2}^x + S_j^y S_{j+2}^y + \Delta_2 S_j^z S_{j+2}^z). \quad (4.3)$$

We also give that of a XXZ spin chain under random magnetic field by

$$\mathcal{H}_{\text{random}} = J \sum_{j=1}^L (S_j^x S_{j+1}^x + S_j^y S_{j+1}^y + \Delta S_j^z S_{j+1}^z) + \sum_{j=1}^L h_j S_j^z. \quad (4.4)$$

Here, $S^\alpha = \frac{1}{2} \sigma^\alpha$ and $(\sigma^x, \sigma^y, \sigma^z)$ are the Pauli matrices; h_j is random magnetic field along the z axis at site j ; the periodic boundary conditions are imposed. The random magnetic field h_j 's are uncorrelated random numbers with a Gaussian distribution: $\langle h_j \rangle = 0$ and $\langle h_n h_m \rangle = h^2 \delta_{nm}$. The schematic pictures of the above two models are shown in Fig. 4.1.

The Hamiltonian (4.3) is nonintegrable when the NNN coupling parameter J_2 is nonzero, while it is integrable when J_2 vanishes. Here we note that Eq. (4.3) is coincides with the NNN coupling Heisenberg chain when $\Delta_1 = \Delta_2 = 1$. We should also note that the Hamiltonian (4.4) is integrable when $h = 0$, while it is not when $h \neq 0$.

4.2.2 Desymmetrization

Let us discuss desymmetrization of the Hamiltonians of the XXZ spin chains. When performing calculation on level statistics, one has to separate the Hamiltonian matrices into some sectors; in each sector, the eigenstates have the same quantum numbers. The NNN coupled XXZ chains are invariant under spin rotation around the z axis, translation, reflection, and spin reversal. Therefore we consider quantum numbers for the total S^z (S_{tot}^z), the total momentum K_{tot} , the parity, and the spin reversal. However the total momentum K_{tot} is invariant under reflection only when $K_{\text{tot}} = 0$ or π . Thus the desymmetrization according to parity is performed only when $K_{\text{tot}} = 0$ or π . Similarly, S_{tot}^z is invariant under spin reversal only when $S_{\text{tot}}^z = 0$. Thus the desymmetrization according to spin reversal is performed only when $S_{\text{tot}}^z = 0$. In the case of a XXZ spin chain under random magnetic field, we have to consider only S_{tot}^z as a quantum number.

It is convenient to use a momentum-based form for the Hamiltonian when we discuss the symmetries of the model as well as when we calculate the eigenvalues. To obtain the form, we perform the Jordan-Wigner and the Fourier transformations on the original Hamiltonian. Some details are explained in Appendix B.

We now discuss some details of the spin reversal operation. The spin reversal operation on the spin variable of the j th site is defined by

$$S_j^\pm \rightarrow S_j^\mp, \quad S_j^z \rightarrow -S_j^z. \quad (4.5)$$

Here, $S_j^\pm = (S_j^x \pm iS_j^y)/2$. Let M denote the number of down-spins in a given sector. The value of the total spin operator S_{tot}^z is given by $S_{\text{tot}}^z = L/2 - M$. We can show that in a sector of $S_{\text{tot}}^z = L/2 - M$, the transformation of Eq. (4.5) corresponds to the following operation on momentum-based fermion operators:

$$\hat{c}_k^\dagger \rightarrow -\hat{c}_{\pi-k}, \quad \hat{c}_k \rightarrow -\hat{c}_{\pi-k}^\dagger. \quad (4.6)$$

Here, \hat{c}_k^\dagger and \hat{c}_k are the creation and annihilation operators of free fermions with momentum k . We note that the value of momentum k is given by $(2\pi/L) \times$ (an integer) for odd M and $(2\pi/L) \times$ (a half-integer) for even M . An explicit derivation of the transformation Eq. (4.6) from the definition Eq. (4.5) is given in Appendix C.

For desymmetrizing the Hamiltonian with respect to spin reversal symmetry, it is useful to know how the vacuum state transforms under the spin reversal operation expressed in terms of the momentum-based fermion operators. Let us denote by $|0\rangle$ the vacuum state where there is no down-spin. Under the spin reversal operation, it transforms up to a phase factor A_L as follows

$$|0\rangle \rightarrow A_L \hat{c}_{q_1}^\dagger \hat{c}_{q_2}^\dagger \cdots \hat{c}_{q_L}^\dagger |0\rangle \quad (4.7)$$

Here q_j denotes momentum $(2\pi/L)j$ for $j = 1, 2, \dots, L$, when M is odd, and $(2\pi/L)(j - 1/2)$ for $j = 1, 2, \dots, L$, when M is even. We can show that the phase factor A_L is given

by

$$A_L = \frac{1}{L^{L/2}} \sum_{P \in \mathcal{S}_L} \epsilon_P \exp(-i \sum_{j=1}^L j k_{Pj}). \quad (4.8)$$

Here \mathcal{S}_L denotes the set of permutations on L elements, ϵ_P the sign of permutation P . Furthermore, we can calculate the phase factor A_L as follows

$$A_L = \begin{cases} (-1)^\ell & \text{for } M = 2\ell \\ (-1)^{\ell+1} & \text{for } M = 2\ell + 1 \end{cases} \quad (4.9)$$

The derivation is given in Appendix D.

It is sometimes convenient to use the following in stead of Eq. (4.6):

$$\hat{c}_k^\dagger \rightarrow \hat{c}_{\pi-k}, \quad \hat{c}_k \rightarrow c_{\pi-k}^\dagger. \quad (4.10)$$

The Hamiltonians are invariant not only for Eq. (4.6) but also for Eq. (4.10). The form Eq. (4.10) has an advantage that we do not need to consider the phase factor -1 that appears in Eq. (4.6).

Making use of the spin reversal operation expressed in terms of the fermion basis Eq. (4.10), we have desymmetrized the Hamiltonian matrix in the sector $S_{\text{tot}}^z = 0$ with respect to spin reversal symmetry. For a given vector with $S_{\text{tot}}^z = 0$, we calculate how it transforms under the operation Eq. (4.10). If it is not a singlet and transforms into a different vector, then we combine the pair into an eigenvector of the operation Eq. (4.10).

4.2.3 Unfolding

To find universal statistical properties of the Hamiltonians, one has to deal with unfolded eigenvalues instead of raw eigenvalues. The unfolded eigenvalues are renormalized values, whose local density of states is equal to unity everywhere in the spectrum. In this work, the unfolded eigenvalues x_i 's are obtained from the raw eigenvalues E_i in the following method. Let us define the integrated density of states as

$$n(E) = \sum_{i=1}^N \theta(E - E_i). \quad (4.11)$$

Here, $\theta(E)$ is the step function and N is the number of the eigenvalues. We choose some points of coordinates: $(E_i, n(E_i))$ for $i = 1, 21, 41, \dots, N$. The average of the integrated density of states $\langle n(E) \rangle$ is approximated by the spline interpolation through the chosen points. The unfolded eigenvalues are defined as

$$x_i = \langle n(E_i) \rangle. \quad (4.12)$$

In Fig. 4.2, the schematic picture of the integrated density of states shows how to obtain unfolded eigenvalues from raw eigenvalues.

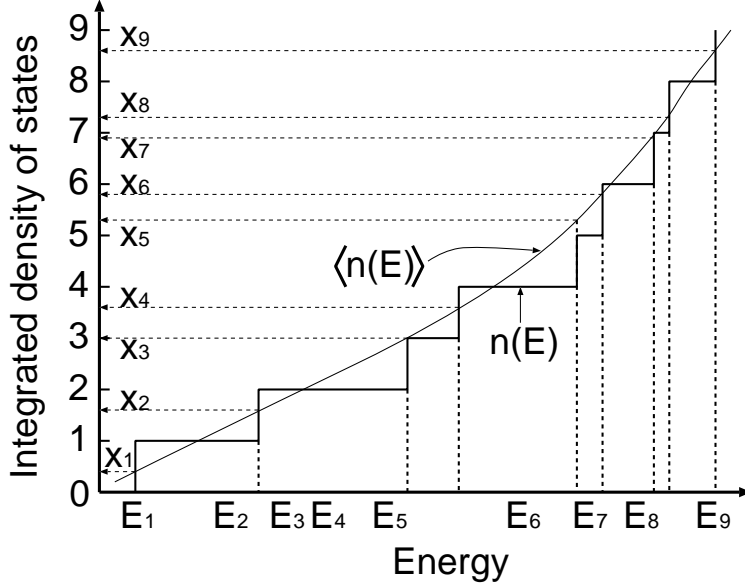


Figure 4.2: How to obtain unfolded eigenvalues x_j 's from raw eigenvalues E_j 's. The integrated density of states $n(E)$ is defined by Eq. (4.11). The average of the integrated density of states $\langle n(E) \rangle$ here is just an example.

4.2.4 Level-spacing distribution, spectral rigidity and number variance

To analyze spectral properties, in this chapter, we calculate three quantities: level-spacing distribution $P(s)$, spectral rigidity $\Delta_3(l)$, and number variance $\Sigma^2(l)$. The level-spacing distribution is the probability function $P(s)$ of nearest-neighbor level-spacing $s = x_{i+1} - x_i$, where x_i 's are unfolded eigenvalues. The level-spacing distribution is calculated over the whole spectrum of unfolded eigenvalues unless we specify the range. The spectral rigidity is given by

$$\Delta_3(l) = \left\langle \frac{1}{l} \min_{a,b} \int_{\varepsilon_0 - l/2}^{\varepsilon_0 + l/2} [N_u(\varepsilon) - a\varepsilon - b]^2 d\varepsilon \right\rangle_{\varepsilon_0}, \quad (4.13)$$

where $N_u(\varepsilon) = \sum_i \theta(\varepsilon - \varepsilon_i)$ is the integrated density of unfolded eigenvalues and $\langle \rangle_{\varepsilon_0}$ denotes an average over ε_0 . The average is done on the whole spectrum except about 15 levels on each side. The expression of $\Delta_3(l)$ gives the least square deviation of $N_u(\varepsilon)$ from the best fit straight line in an interval l . The number variance is given by

$$\Sigma^2(l) = \left\langle \left[N_u \left(\varepsilon_0 + \frac{l}{2} \right) - N_u \left(\varepsilon_0 - \frac{l}{2} \right) - l \right]^2 \right\rangle_{\varepsilon_0}, \quad (4.14)$$

where $\langle \rangle_{\varepsilon_0}$ denotes an average over ε_0 [34]. The average is done on the whole spectrum except about 10 levels on each side.

For NNN coupled chains, we calculate the spectra for $L = 18$. The matrix size is

Table 4.1: Matrix size of the subspaces where calculation is performed for NNN coupled XXZ spin chains ($L = 18$) in this work.

S_{tot}^z and K_{tot}	Matrix size
$S_{\text{tot}}^z = 0$ and $K_{\text{tot}} = 2\pi/18$	1364×1364
$S_{\text{tot}}^z = 1$ and $K_{\text{tot}} = 0$	1282×1282
$S_{\text{tot}}^z = 0$ and $K_{\text{tot}} = 0$ (not considering the spin reversal)	1387×1387

Table 4.2: Matrix size of the largest subspace and the number of samples calculated in this work for XXZ spin chains under random magnetic field.

Lattice size	Matrix size	Number of samples
8	70×70	10000
10	252×252	3000
12	924×924	1000
14	3432×3432	300

given by the following (See also Table 4.1): 1364×1364 for $S_{\text{tot}}^z = 0$ and $K_{\text{tot}} = 2\pi/L$, where L is the number of sites; 1282×1282 for $S_{\text{tot}}^z = 1$ and $K_{\text{tot}} = 0$; 1387×1387 for $S_{\text{tot}}^z = 0$ and $K_{\text{tot}} = 0$ when desymmetrization is performed except for spin reversal. For XXZ spin chains under a random magnetic field, we consider the largest subspace $S_{\text{tot}}^z = 0$. The largest sectors for the lattice size $L = 8, 10, 12, 14$ have 70, 252, 924, 3432 eigenvalues, respectively (see Table 4.2). We have calculated 10000, 3000, 1000, 300 samples of $P(s)$ and $\Delta_3(l)$ for $L = 8, 10, 12, 14$, respectively (see Table 4.2), and averaged the samples for each L . To calculate the eigenvalues, we use standard numerical methods, which are contained in the LAPACK library.

Numerical calculations are performed for the XY -like region, $|\Delta| < 1$, where Δ is the anisotropic parameter. It may be interesting to study for the Ising-like region, $|\Delta| > 1$, because there exist Ising-like magnets. For example, CsCoBr_3 and CsCoCl_3 are quasi-1D Ising-like antiferromagnets with $\Delta \sim 10$ [10]. For $\Delta \gg 1$, however, level statistics is not reliable because energy spectra have some large gaps relative to Δ and the above unfolding method is invalid.

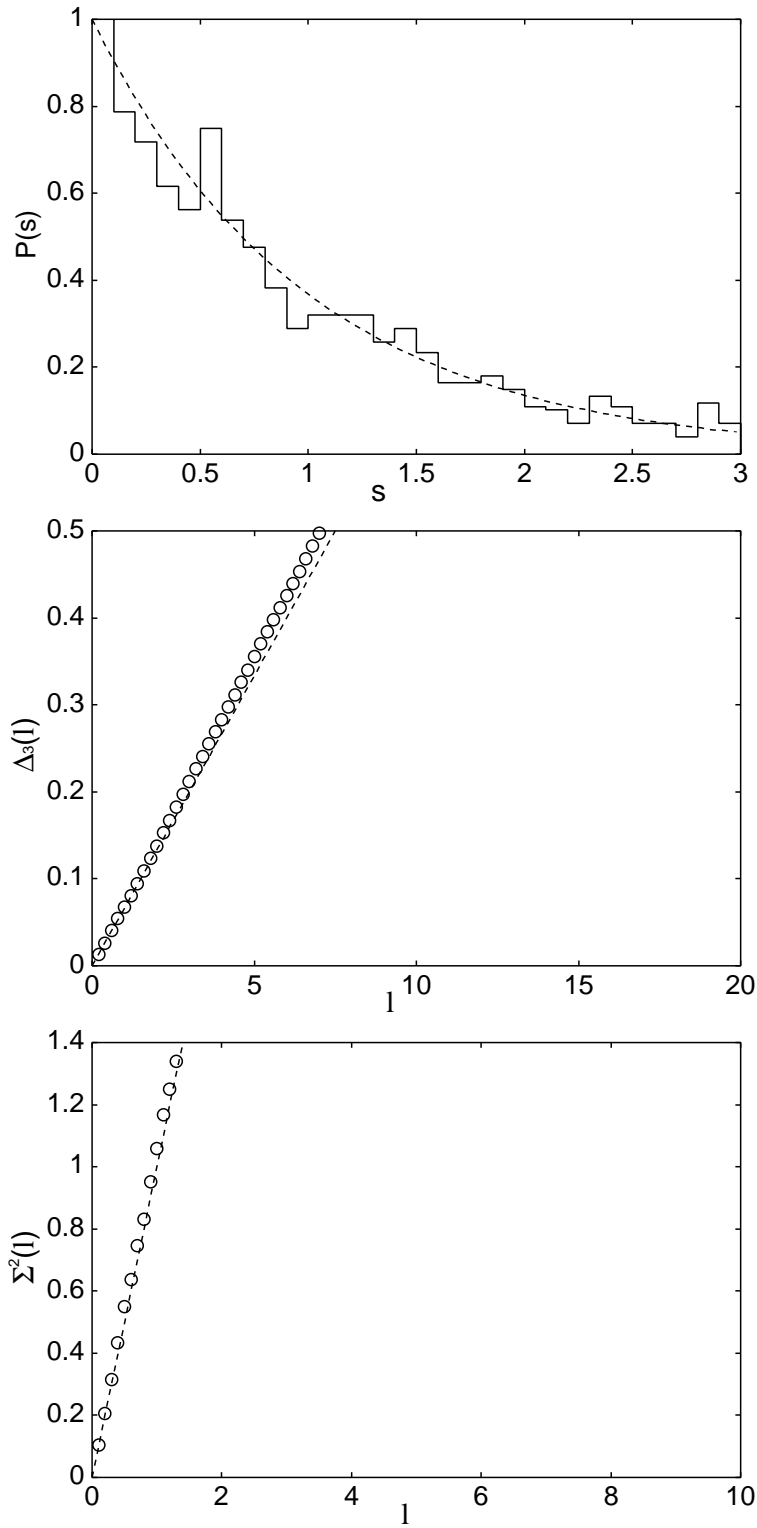


Figure 4.3: Level-spacing distribution, spectral rigidity and numerical variance of the integrable XXZ spin chain ($J_2 = 0$) for $L = 18$, $J_1 = 1$, $\Delta_1 = 0.8$, $S_{\text{tot}}^z = 1$, $K_{\text{tot}} = 0$ (reprinted from Ref. [17]). Broken line shows the Poisson distribution.

4.3 Integrable XXZ spin chain

Let us confirm the Poissonian behavior for the generic case of the integrable XXZ spin chain. When $J_2 = 0$, the level-spacing distribution $P(s)$ mostly show the Poisson distribution as shown in Fig. 4.3. The spectral rigidity $\Delta_3(l)$ and the number variance $\Sigma^2(l)$ also shows Poissonian behavior. We confirmed numerically the standard result for some generic values of the XXZ coupling Δ_1 .

On the other hand, extraordinary behavior can be seen for the special case of the integrable XXZ spin chain that has the sl_2 loop algebra symmetry. Here we recall that the XXZ spin chain is integrable when the NNN coupling J_2 vanishes, and also that the sl_2 loop algebra symmetry exists when q is a root of unity. Here the anisotropy Δ_1 is related to q through $\Delta_1 = (q + q^{-1})/2$. For instance, when the parameter q is given by $\exp(i\pi/3)$, we have $\Delta_1 = 0.5$.

The level spacing distribution $P(s)$ and the spectral rigidity $\Delta_3(l)$ of the integrable XXZ spin chain are shown for $\Delta_1 = 0.5$ in Fig. 4.4. In Fig. 4.4 (a) we do not perform desymmetrization with respect to spin reversal, while in Fig. 4.4 (b) we plot the level-spacing distribution $P(s)$ and the spectral rigidity $\Delta_3(l)$ after we desymmetrize the Hamiltonian with respect to the spin reversal operation.

We observe that there still remain many degeneracies associated with the sl_2 loop algebra symmetry, even after desymmetrizing the Hamiltonian with respect to spin reversal symmetry. The level-spacing distribution $P(s)$ has a small peak at $s = 0$ in Fig. 4.4 (b). Furthermore, the slopes of $\Delta_3(l)$ shown in the insets of Figs. 4.4 (a) and 4.4 (b) are larger than that of Poissonian behavior. However, the numerical result does not necessarily give a counterexample to the conjecture of RMT. The level statistics might show Poissonian behavior, if we completely desymmetrize the Hamiltonian matrix in terms of the sl_2 loop algebra symmetry.

4.4 Next-nearest-neighbor coupled XXZ spin chains

We now numerically discuss the characteristic behavior of level statistics for next-nearest-neighbor (NNN) coupled XXZ spin chains in this section.

4.4.1 Wigner behavior for $S_{\text{tot}}^z = 0$

For a sector of $S_{\text{tot}}^z = 0$, we numerically discuss the characteristic behavior of level statistics on the XXZ spin chains. We should remember that the system is invariant under spin reversal only when $S_{\text{tot}}^z = 0$. Here we note that spin reversal symmetry has not been considered explicitly in previous studies of level statistics for various quantum spin chains. In some sense, desymmetrizing the Hamiltonian with respect to spin reversal symmetry

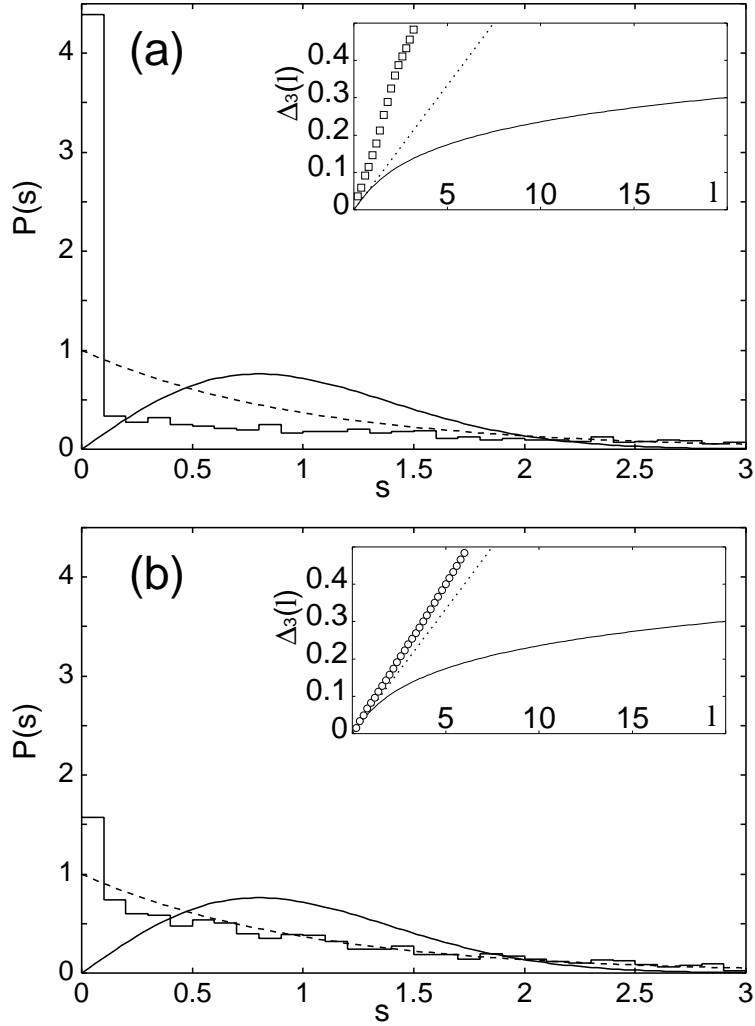


Figure 4.4: Level-spacing distribution of the integrable XXZ spin chain ($J_2 = 0$) for $L = 18$, $J_1 = 1$, $\Delta_1 = 0.5$, $S_{\text{tot}}^z = 0$, $K_{\text{tot}} = 2\pi/L$. (a) Desymmetrization with respect to spin reversal is not performed. (b) Desymmetrization with respect to spin reversal is performed. The inset is spectral rigidity for each case (reprinted from Ref. [17]). Broken lines corresponds to Poissonian behavior, and solid lines Wigner behavior.

has been avoided due to some technical difficulty. For XXZ spin chains, Level statistics has been discussed only for sectors of $S_{\text{tot}}^z \neq 0$, where it is not necessary to consider spin reversal symmetry.

Let us show explicitly such a case that Wigner behavior appears for $S_{\text{tot}}^z = 0$ if we consider spin reversal symmetry. In Fig. 4.5 we have obtained the numerical results for level statistics such as the level-spacing distribution $P(s)$, the spectral rigidity $\Delta_3(l)$ and the number variance $\Sigma^2(l)$, for the sector of $K_{\text{tot}} = 2\pi/L$ and $S_{\text{tot}}^z = 0$. Here we note that in the sector the parity invariance does not exist and we focus on spin reversal symmetry. The numerical results of level statistics shown in Fig. 4.5 clearly suggest Wigner behavior. The curve of the Wigner distribution fits well to the data of the level-spacing distribution $P(s)$. The plots of the spectral rigidity $\Delta_3(l)$ are consistent with the curve of Wigner behavior as shown in Fig. 4.5. It is also the case with the number variance $\Sigma^2(l)$.

4.4.2 How does non-Wigner behavior appear?

Unexpected non-Wigner behavior has been reported in Ref. [15] for level-spacing distributions of the NNN coupled XXZ chains. Let us discuss the reason why it was observed, considering both mixed symmetry and finite-size effects. There are two types of non-Wigner profiles for the nonintegrable systems: one is given by almost the numerical average of the Poisson and the Wigner distributions, and another one is rather close to the Poisson distribution. The profiles of the first type appear in various cases [15], such as the case of $\Delta_2 = 0.5$. Similar non-Wigner behavior has been observed for a circular billiard when the angular momentum $L_z = 0$, and for an interacting two-electron system with the Coulomb interaction in a quantum billiard when $L_z = 0$ [41]. The profiles of the second type appear in particular for the case of $\Delta_1 \simeq 1$ or $\Delta_2 \simeq 1$. We may call the latter Poisson-like behavior rather than simple non-Wigner behavior. Both types of non-Wigner distributions have been observed in the subspace of $S_{\text{tot}}^z = 0$, which is the largest sector of the Hamiltonian matrix of Eq. (4.3). Here we note that the observations in Ref. [15] for $S_{\text{tot}}^z = 0$ do not contradict with the Wigner behavior of Ref. [31] for $S_{\text{tot}}^z \neq 0$, where the level-spacing distributions of similar XXZ chains have been discussed.

We show level-spacing distributions in Fig. 4.6 for the four cases: $S_{\text{tot}}^z = 0$ or 1 and $\Delta_1 = \Delta_2 = 0.5$ or 0.98. The numerical results suggest that the value of S_{tot}^z should be important as well as the anisotropy parameters, Δ_1 and Δ_2 , in the observed non-Wigner behavior of the level-spacing distributions. When $\Delta_1 = \Delta_2 = 0.5$, Wigner behavior appears for $S_{\text{tot}}^z = 1$, while the non-Wigner behavior was observed for $S_{\text{tot}}^z = 0$. We have also checked that Wigner behavior appears for $S_{\text{tot}}^z = 2$. Furthermore, we have confirmed that such S_{tot}^z -dependence of the level-spacing distribution is valid for some values of K_{tot} . Here we have desymmetrized the Hamiltonian according to S_{tot}^z , K_{tot} and the parity when it exists, but not to the spin reversal. Here we note that the parity invariance exists only

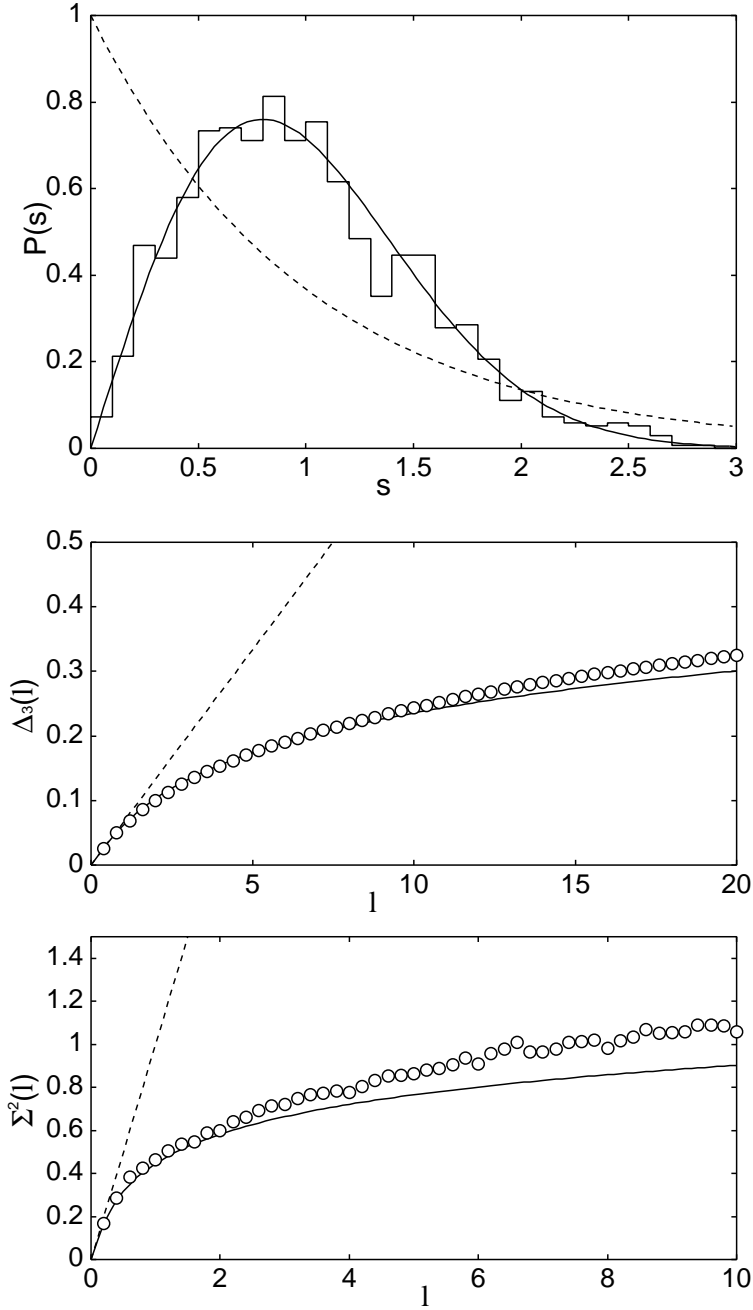


Figure 4.5: Level-spacing distribution $P(s)$, spectral rigidity $\Delta_3(l)$, and number variance $\Sigma^2(l)$ of the NNN coupled chain for $L = 18$, $J_2/J_1 = 0.5$, $\Delta_1 = \Delta_2 = 0.5$, $S_{\text{tot}}^z = 0$, $K_{\text{tot}} = 2\pi/L$ under complete desymmetrization (reprinted from Ref. [17]). Broken lines correspond to Poissonian behavior, and solid curves Wigner behavior.

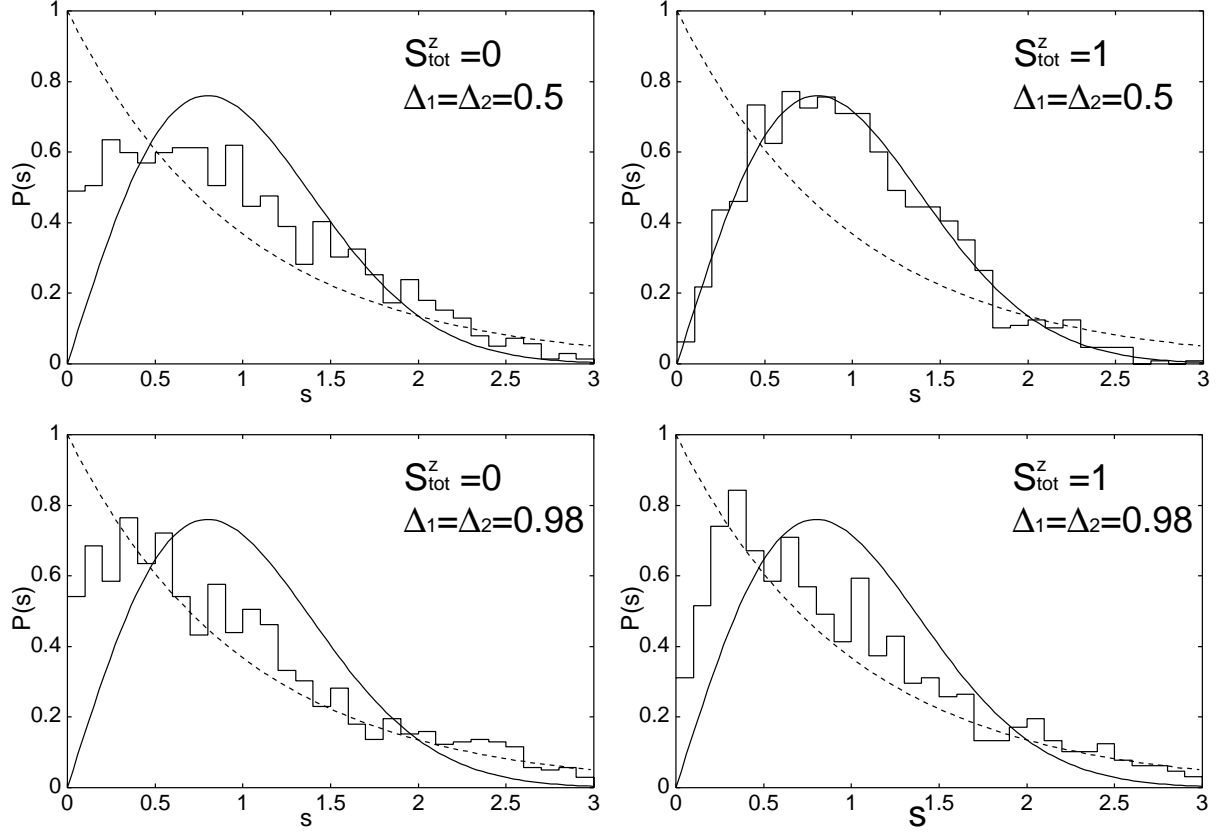


Figure 4.6: Level-spacing distribution $P(s)$ of the NNN coupled chain for $L = 18$, $J_2/J_1 = 1$, $K_{\text{tot}} = 0$ (reprinted from Ref. [17]). Here, desymmetrization is performed except for spin reversal. Broken lines, the Poisson distribution; solid curves, the Wigner distribution. In each of the four distributions $P(s)$ vanishes at $s = 0$: there is no degeneracy among energy levels.

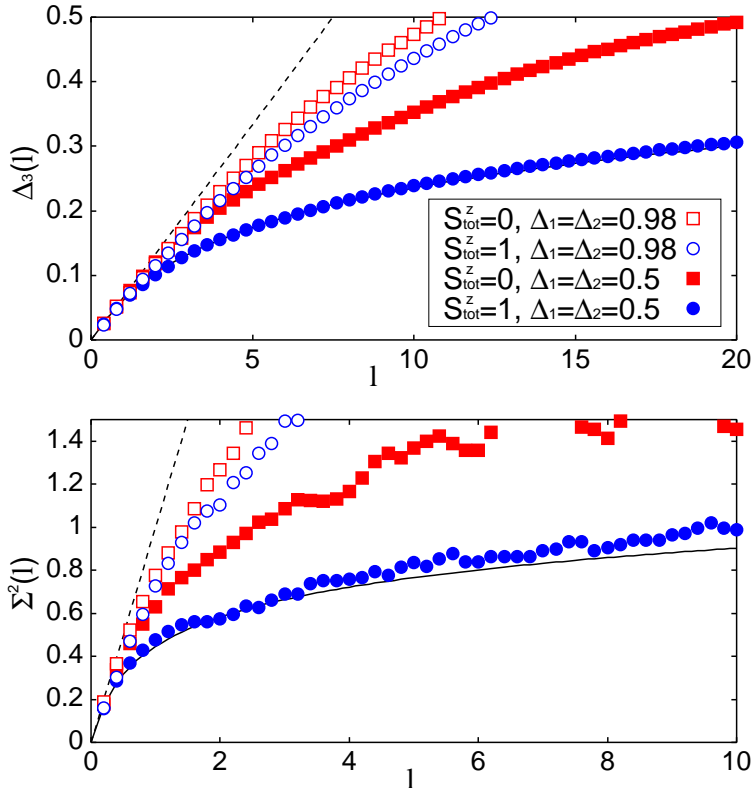


Figure 4.7: Spectral rigidity $\Delta_3(l)$ and number variance $\Sigma^2(l)$ of the NNN coupled chain for $L = 18$, $J_2/J_1 = 1$, $K_{\text{tot}} = 0$ (reprinted from Ref. [17]). Here, desymmetrization is performed except for spin reversal. Broken lines, Poissonian behavior; Solid lines, Wigner behavior.

for sectors with $K_{\text{tot}} = 0$ or π when L is even.

The non-Wigner behavior observed for the case $S_{\text{tot}}^z = 0$ and $\Delta_1 = \Delta_2 = 0.5$ shown in Fig. 4.6 should be due to mixed symmetry. We have not performed the desymmetrization according to spin reversal which is important only for $S_{\text{tot}}^z = 0$. Let us recall the Wigner behavior for $S_{\text{tot}}^z = 0$ shown in Fig. 4.5. It is for $K_{\text{tot}} = 2\pi/L$. However, Wigner behavior should appear also for the sector of $K_{\text{tot}} = 0$ and $S_{\text{tot}}^z = 0$ where we have to perform the desymmetrization according to both parity and spin reversal simultaneously. Because the behavior of level statistics should be independent of K_{tot} .

The Poisson-like behavior for the case $\Delta_1 = \Delta_2 = 0.98$ should be dominated by the finite-size effects. In fact, for $S_{\text{tot}}^z = 1$ of Fig. 4.6, the Poisson-like behavior appears when $\Delta_1 = \Delta_2 = 0.98$, while Wigner behavior appears when $\Delta_1 = \Delta_2 = 0.5$. We have confirmed that such tendency does not depend on the value of K_{tot} : we see it not only for $K_{\text{tot}} = 0$ but also for $K_{\text{tot}} \neq 0$. We discuss the finite-size effects on this model later.

The observations of the level-spacing distributions can also be confirmed by investigating spectral rigidity $\Delta_3(l)$ and number variance $\Sigma^2(l)$. In Fig. 4.7, $\Delta_3(l)$ and

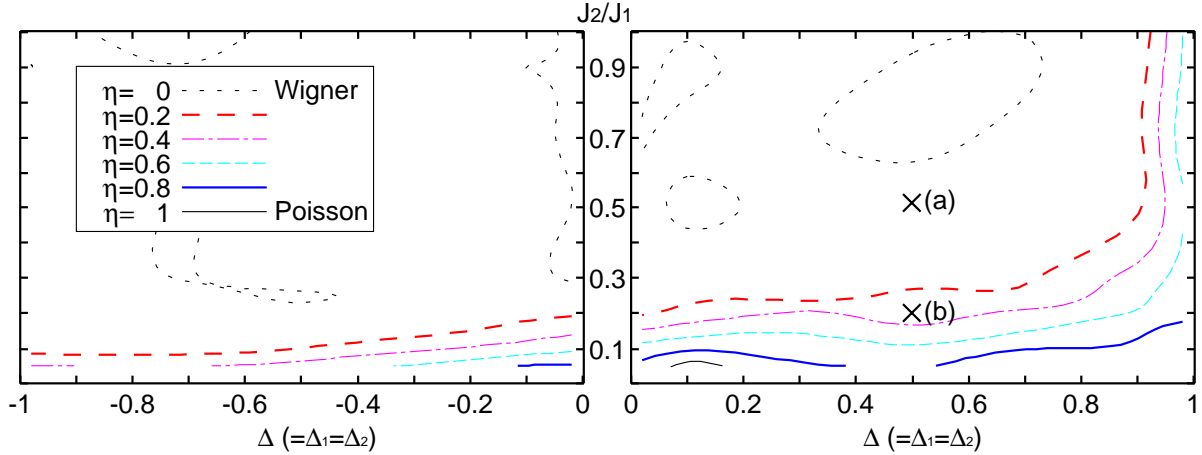


Figure 4.8: The diagram of contour lines of η for the NNN coupled chain with $L = 18$, in the sector of $S_{\text{tot}}^z = 1$ and $K_{\text{tot}} = 0$ (reprinted from Ref. [17]). Roughly speaking, the area above the red long dashed line, Wigner behavior; the area below the blue solid line, Poissonian behavior. The points (a) and (b) correspond to Figs 4.9(a) and 4.9(b), respectively.

$\Sigma^2(l)$ are shown for the four cases corresponding to those of Fig. 4.6. For $S_{\text{tot}}^z = 1$ and $\Delta_1 = \Delta_2 = 0.5$, Wigner behavior appears. For $S_{\text{tot}}^z = 0$ and $\Delta_1 = \Delta_2 = 0.5$, an intermediate behavior appears, which is close to the average between Wigner and Poissonian behaviors. For $\Delta_1 = \Delta_2 = 0.98$, both for $S_{\text{tot}}^z = 0$ and $S_{\text{tot}}^z = 1$, Poisson-like behavior appears for $\Delta_3(l)$ and $\Sigma^2(l)$.

4.4.3 Finite-size effects on the level spacing distribution

Let us explicitly discuss finite-size effects appearing in level statistics. Hereafter we discuss level statistics for the case $S_{\text{tot}}^z = 1$ so that we do not have to perform the desymmetrization according to spin reversal. They should be important in the Poisson-like or non-Wigner behavior observed in level statistics for the completely desymmetrized XXZ Hamiltonians. There are two regions in which finite-size effects are prominent: A region where J_2 is close to zero and another region where Δ_1 and Δ_2 are close to 1. In the former region, quantum integrability appears through finite-size effects, and the characteristic behavior of level statistics becomes close to Poisson-like behavior. In the latter region, Poisson-like behavior appears due to the symmetry enhancement at the point of $\Delta_1 = \Delta_2 = 1$, where the $U(1)$ symmetry of the XXZ spin chain expands into the spin $SU(2)$ symmetry.

Let us now discuss how the degree of non-Wigner behavior depends on the anisotropy parameters, Δ_1 and Δ_2 , and the NNN coupling, J_2 . For simplicity we set $\Delta_1 = \Delta_2$ and denote it by Δ , and we also consider the ratio of J_2/J_1 . We express the degree of non-

Wigner behavior by the following parameter:

$$\eta = \frac{\int_0^{s_0} [P(s) - P_{\text{Wig}}(s)] ds}{\int_0^{s_0} [P_{\text{Poi}}(s) - P_{\text{Wig}}(s)] ds}, \quad (4.15)$$

where $s_0 = 0.4729\dots$ is the intersection point of $P_{\text{Poi}}(s)$ and $P_{\text{Wig}}(s)$ [16, 37]. We have $\eta = 0$ when $P(s)$ coincides with $P_{\text{Wig}}(s)$, and $\eta = 1$ when $P(s)$ coincides with $P_{\text{Poi}}(s)$. The diagram of contour lines of η is shown in Fig. 4.8. We have calculated them for the area $-0.98 \leq \Delta \leq -0.02$, $0.02 \leq \Delta \leq 0.98$, and $0.02 \leq J_2/J_1 \leq 1$, where $\Delta = \Delta_1 = \Delta_2$.

The contour lines of η show that behavior close to Wigner one appears in a large region, while the Poisson-like behavior appears in a narrow region along the line of $J_2/J_1 = 0$ and that of $\Delta_1 = \Delta_2 = 1$. The Poisson-like behavior is dominated by finite-size effects and hence should vanish when $L \rightarrow \infty$. This expectation should be consistent with the suggestion in Ref. [31] that an infinitesimal integrability-breaking term (the NNN term of Eq. (4.3) in this paper) would lead to Wigner behavior. Here we remark that the phase diagrams of the ground state [42, 43] are totally different from the diagram of contour lines of η . It is due to the fact that level statistics reflects highly excited states rather than the ground state.

When $\Delta_1 = \Delta_2 = 0.98$, Poisson-like behavior appears in level statistics due to some finite-size effects. It will be explicitly shown in Figs. 4.6 and 4.7. When $\Delta_1 = \Delta_2 = 1$, Eq. (4.3) coincides with the Heisenberg chain, which has the spin $SU(2)$ symmetry. Some degenerate energy levels at $\Delta_1 = \Delta_2 = 1$ can become nondegenerate when Δ_1 and Δ_2 are not equal to 1. The difference among the nondegenerate energy levels should be smaller than the typical level spacing when Δ_1 and Δ_2 are close to 1. The typical level spacing, which is of the order of $1/L$, should become large when the system size L is small. Thus, the Poisson-like behavior should practically appear in level statistics. We note that for the Heisenberg chain Wigner behavior appears in the level-spacing distribution when we desymmetrize the Hamiltonian with respect to the spin $SU(2)$ symmetry [27, 28].

4.4.4 Homogeneity of the characteristic behavior of level statistics throughout the spectrum

Let us discuss that for the XXZ spin chains the characteristic behavior of level statistics does not depend on the energy range of the spectrum. In Fig. 4.9, we show level-spacing distributions evaluated at points (a) and (b) shown in the diagram of Fig. 4.8. They are evaluated for three different energy ranges. The distributions shown in Fig. 4.9(a) give Wigner behavior, while the distributions of Fig. 4.9(b) are close to Poisson-like behavior.

Let us explain the three different energy ranges shown in Fig. 4.9. Red histograms show the level-spacing distributions evaluated for all levels, while green bars show those evaluated only for the 1/3 of all levels around the center, and blue crosses for the 10% of all levels located from each of the two spectral edges.

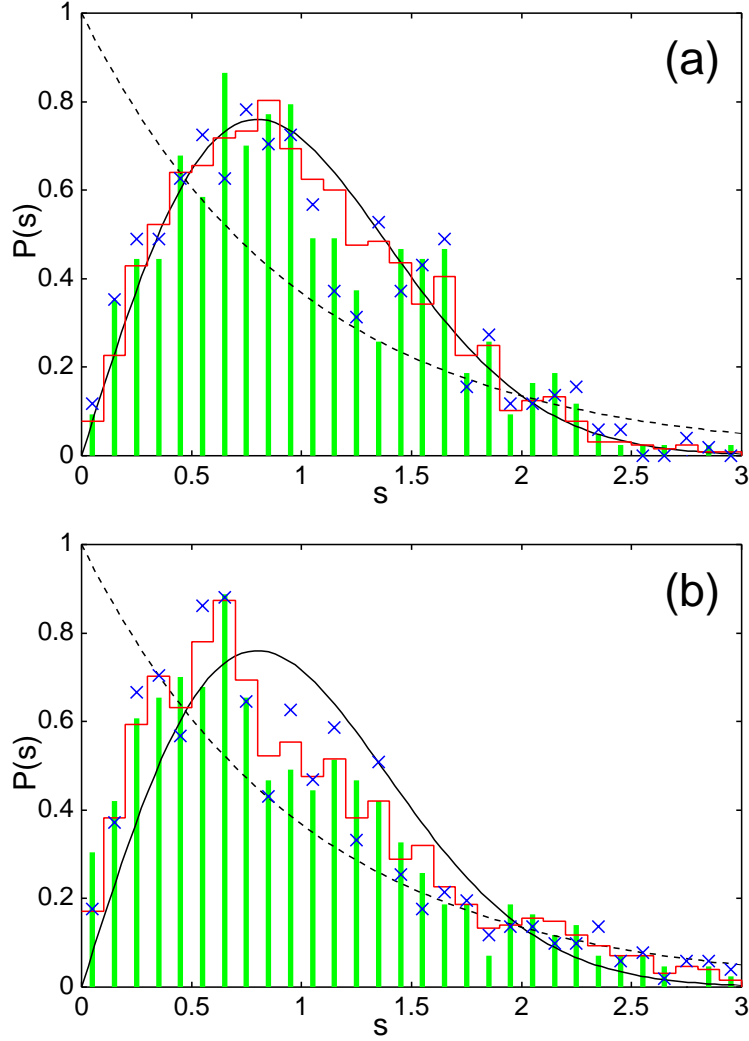


Figure 4.9: Level-spacing distribution of the NNN coupled chain for $L = 18$, $\Delta_1 = \Delta_2 = 0.5$, $S_{\text{tot}}^z = 1$, and (a) $J_2/J_1 = 0.5$; (b) $J_2/J_1 = 0.2$ (reprinted from Ref. [17]). Red histograms are for all levels; green bars, 1/3 of all levels around the center; blue crosses, 10% of all levels from each of the two edges. Solid and broken lines show the Wigner and Poisson distributions, respectively.

Quite interestingly, the distributions evaluated for the different energy ranges are quite similar to each other. Here we should note that some statistical 'noises' exist but they are rather small. This makes a remarkable contrast between the level-spacing distributions of the XXZ spin chains and that of the Anderson model of disordered systems. Here we recall that even in the metallic phase the level-spacing distribution of the Anderson model shows Poissonian behavior if we evaluate it around the two edge regions of the energy spectrum.

4.5 XXZ spin chains under random magnetic field

Now we discuss the characteristic behavior of the XXZ spin chains under random magnetic field. Under random magnetic field, the system is nonintegrable.

4.5.1 Dependence on the anisotropy parameter Δ

Depending on the anisotropic parameter Δ , the level-spacing distribution $P(s)$ and the spectral rigidity $\Delta_3(l)$ change between the Wigner behavior and the Poissonian behavior as shown in Fig. 4.10, where $L = 14$ and $h/J = 0.5$. When $\Delta = 0$, $P(s)$ almost coincides with $P_{\text{Poi}}(s)$ although the system is nonintegrable due to the random magnetic field. As Δ increases, $P(s)$ rapidly changes to $P_{\text{Wig}}(s)$. The behavior of $\Delta_3(l)$ also changes from Poissonian to Wigner behavior as Δ increases.

Let us explain the Poissonian behavior of $\Delta = 0$ in terms of the Anderson localization. The Hamiltonian (4.4) can be mapped into a model of interacting one-dimensional (1D) free fermions under random potential (see Appendix B):

$$\begin{aligned} \mathcal{H} = & \frac{J}{4} 2 \left[\sum_{j=1}^{L-1} (c_j^\dagger c_{j+1} + c_{j+1}^\dagger c_j) - (-1)^M (c_L^\dagger c_1 + c_1^\dagger c_L) \right] \\ & + \Delta \frac{J}{4} \sum_{j=1}^L (4c_j^\dagger c_j c_{j+1}^\dagger c_{j+1} - 4c_j^\dagger c_j + 1) \\ & + \sum_{j=1}^L h_j \left(\frac{1}{2} - c_j^\dagger c_j \right). \end{aligned} \quad (4.16)$$

Here, L is the number of sites; M is the number of fermions; c_j^\dagger and c_j are the creation and annihilation operators of fermions on the j th site, respectively. And the Anderson model of noninteracting disordered fermions is given by

$$\mathcal{H} = \sum_j \varepsilon_j c_j^\dagger c_j + \sum_{\langle i,j \rangle} V (c_i^\dagger c_j + c_j^\dagger c_i), \quad (4.17)$$

where ε_j is the random potential at the j th site; V is a constant hopping integral; $\langle i, j \rangle$ denotes summation over nearest-neighbor sites. One can find that Eq. (4.16) for $\Delta = 0$

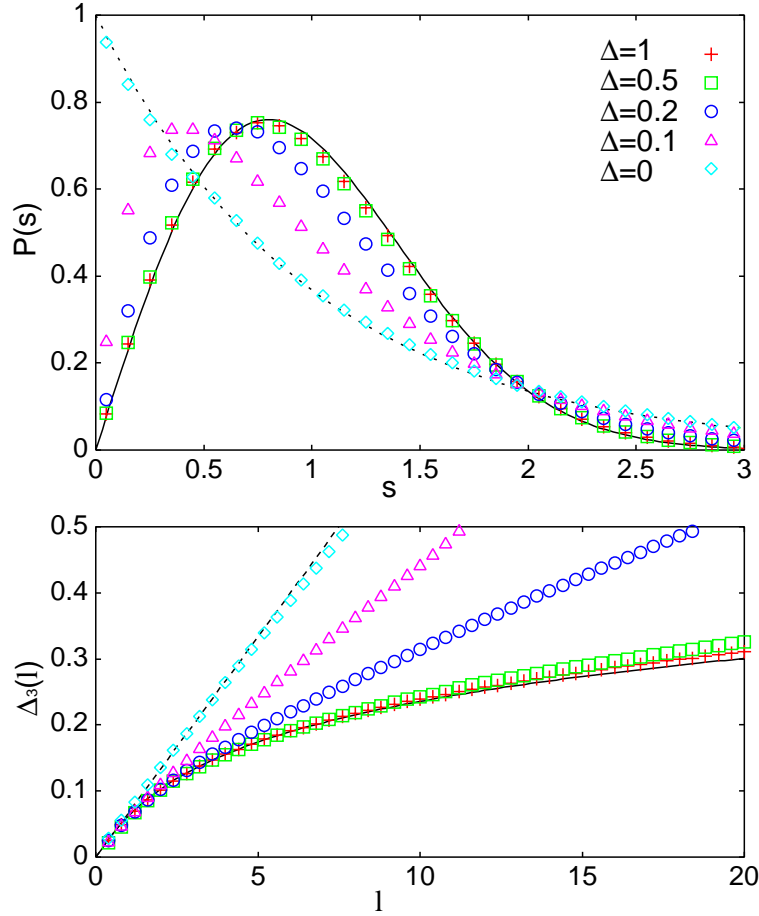


Figure 4.10: Level spacing distribution $P(s)$ and spectral rigidity $\Delta_3(l)$ of the XXZ chains under random magnetic field for $L = 14$, $h/J = 0.5$ (partly reprinted from Ref. [16]). Broken lines, Poissonian behavior; solid lines, Wigner behavior.

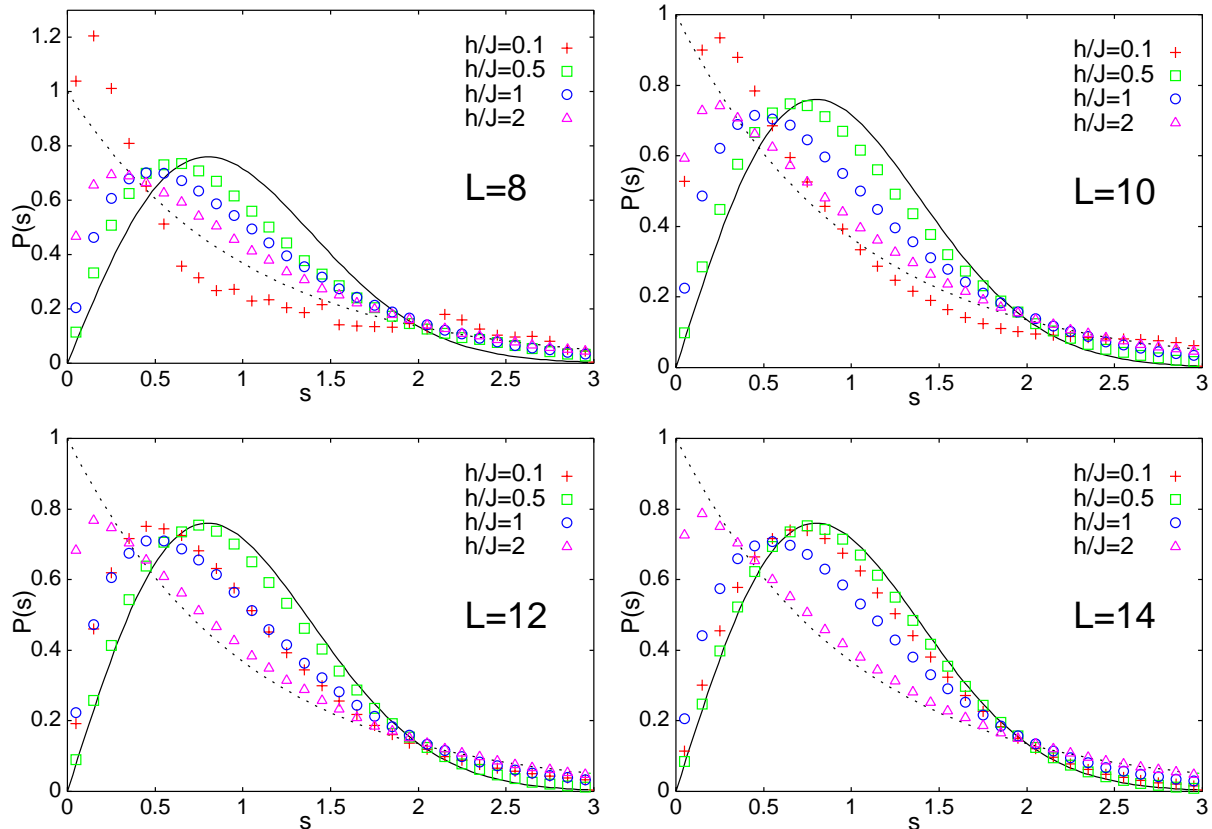


Figure 4.11: Level-spacing distributions of the XXZ chains under random magnetic field for $L = 8, 10, 12, 14$; $h/J = 0.1, 0.5, 1, 2$; $\Delta = 0.5$ (reprinted from Ref. [16]).

corresponds to Eq.(4.17) of the 1D case. It is known that localization always occurs in the 1D case, while the 3D Anderson model has the metallic phase and the localized phase. Here we recall that the metallic phase corresponds to $P_{\text{Wig}}(s)$ and the localized phase to $P_{\text{Poi}}(s)$. Thus, the observed Poissonian behavior for $\Delta = 0$ is consistent with the Anderson localization.

The Hamiltonian (4.4), namely Eq. (4.16), for $\Delta \neq 0$ corresponds to the interacting 1D fermions under random potential. Then, does the Wigner-like behavior of $P(s)$ for $\Delta \neq 0$ suggest that the interaction among fermions should break the Anderson localization in 1D chains? The answer should be “No”. According to Ref. [44], the ground state is in the localized phase at least when $0 < \Delta < 1$. The characteristic behavior of level statistics is influenced mainly by highly excited states, not by the ground states.

4.5.2 Dependence on the magnetic field

We now discuss how the level-spacing distribution $P(s)$ depends on the random magnetic field h . We consider only the case of $\Delta \neq 0$. In Fig. 4.11, the graphs of $P(s)$ are shown

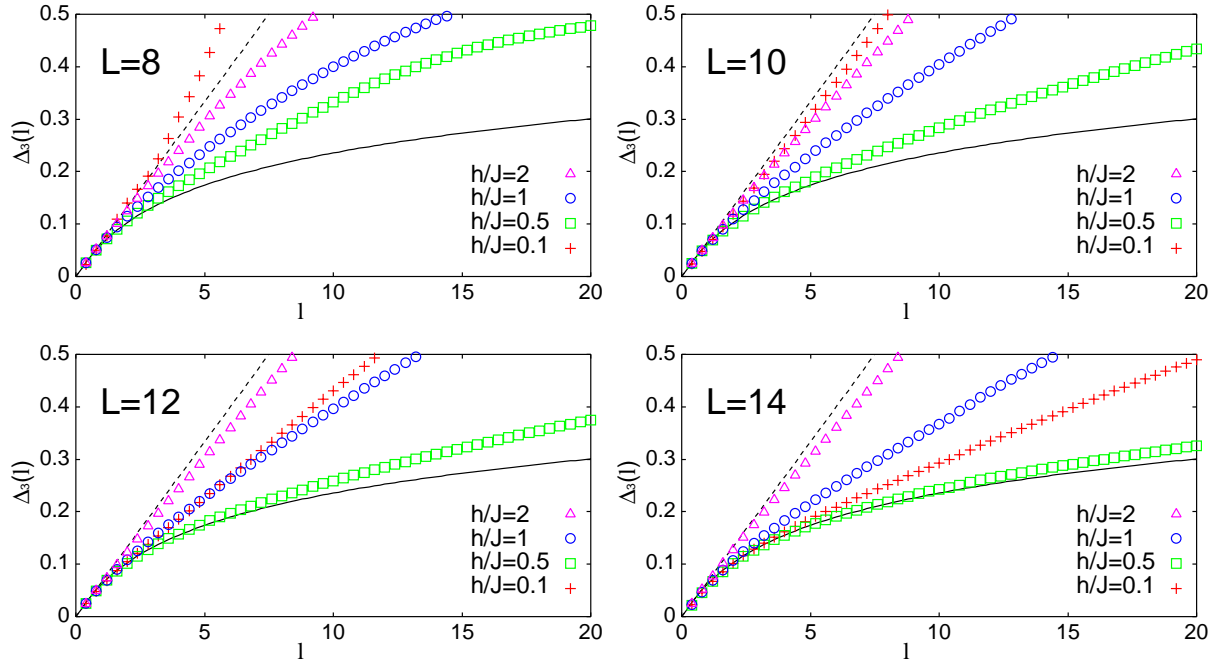


Figure 4.12: Spectral rigidity $\Delta_3(l)$ of the XXZ chains under random magnetic field for $L = 8, 10, 12, 14$; $h/J = 0.1, 0.5, 1, 2$; $\Delta = 0.5$.

for some values of h/J and L , where $\Delta = 0.5$. We first consider the case of large h . As h/J increases from the value of 0.5, we observe that the form of $P(s)$ changes from $P_{\text{Wig}}(s)$ to $P_{\text{Poi}}(s)$. The observation suggests that the effect of random magnetic field on each site should become larger than that of the correlation between adjacent spins, as the random field h/J increases. The spins should become more independent of each other as h/J increases, since the effect of correlation decreases effectively. Thus, the Poisson-like behavior of $P(s)$ should appear in the limit of large h/J . Similar shifts from $P_{\text{Wig}}(s)$ to $P_{\text{Poi}}(s)$ as randomness increases have been discussed for the 3D Anderson model [40], the spin-glass clusters [37], and the open-boundary Heisenberg chain [39].

For the case of small h , the level-spacing distribution $P(s)$ strongly depends on the system size L , and the behavior of $P(s)$ is dominated by finite-size effects. In Fig. 4.11, we observe that the form of $P(s)$ for $h/J = 0.1$ is different from that of the standard Wigner distribution, particularly when L is small. When L is small, random magnetic field is irrelevant to energy levels if it is smaller than the order of $1/L$. In fact, energy differences should be at least in the order of $1/L$, and random magnetic field can be neglected if it is much smaller than some multiple of $1/L$. Thus, for the case of small h , the level statistics should show such a behavior as that of $h = 0$. In fact, the Hamiltonian for $h = 0$ is the integrable XXZ spin chain, which should show Poissonian behavior. Furthermore, the integrable XXZ Hamiltonian at $\Delta = 0.5$ has the sl_2 loop algebra symmetry [7], and the

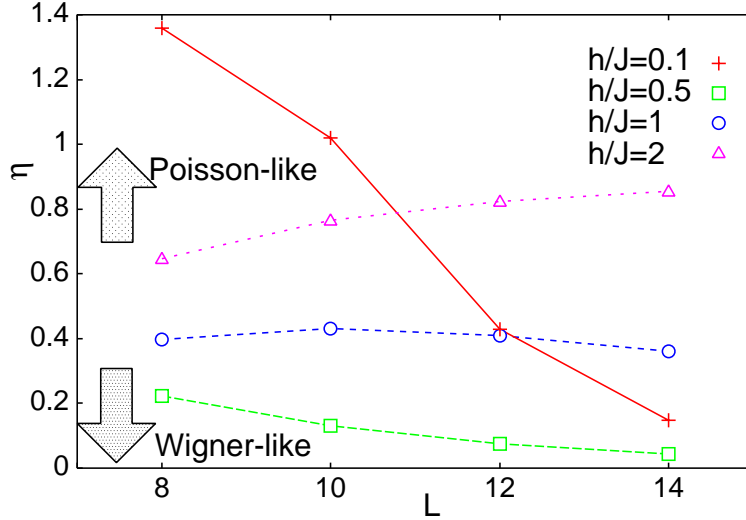


Figure 4.13: Dependence of the parameter η on the lattice size L for $h/J = 0.1, 0.5, 1, 2$ and $\Delta = 0.5$ (reprinted from Ref. [16]). $\eta = 0$ corresponds to the Wigner distribution and $\eta = 1$ to the Poisson distribution.

level-spacing distribution should show a peak at $s = 0$ as shown in Fig. 4.4. In Fig. 4.11, the graph of $P(s)$ for $L = 8$ and $h/J = 0.1$ suggests such behavior.

The behavior of the level-spacing distributions can also be confirmed in Fig. 4.12, where $\Delta_3(l)$ are shown for the four cases corresponding to those of Fig. 4.11. The behavior of $\Delta_3(l)$ changes from Wigner to Poissonian behavior as h/J becomes larger for each L , though the behavior of that for $h/J = 0.1$ strongly depends on the system size L . Particularly, the slope of $\Delta_3(l)$ for $L = 8$ and $h/J = 0.1$ is larger than that of Poissonian behavior.

4.5.3 Dependence on the system size

Let us discuss the finite-size effects on the level-spacing distributions. In order to observe the size dependence of $P(s)$ clearly, we employ the parameter η defined by Eq. (4.15). In Fig. 4.13, the value of η for $h/J = 0.1$ strongly depends on the lattice size L . Moreover, we observe that as L increases, η decreases for $h/J = 0.5$, while η increases for $h/J = 2$. The observation suggests that η approaches either the value 0 or 1 as L increases. In other words, it should become more definite whether $P(s)$ has Wigner-like behavior or not, as the system size becomes large.

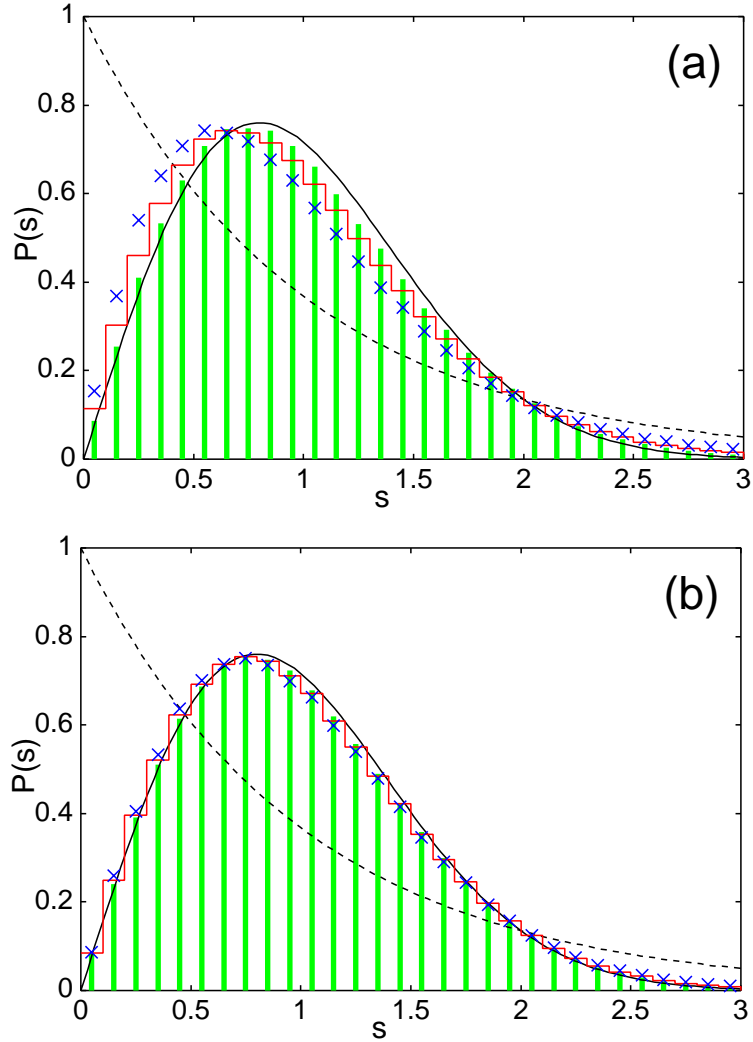


Figure 4.14: Level-spacing distribution of the XXZ spin chains under random magnetic field for $L = 14$, $\Delta = 0.5$, and (a) $h/J = 0.1$; (b) $h/J = 0.5$. Red histograms are for all levels; green bars, $1/3$ of all levels around the center; blue crosses, 10% of all levels from each of the two edges. Solid and broken lines show the Wigner and Poisson distributions, respectively.

4.5.4 Homogeneity of the characteristic behavior of level statistics throughout the spectrum

The characteristic behavior of level statistics does not depend on the energy range of the spectrum for XXZ chains under random magnetic field, either. In Fig. 4.14, we show the level-spacing distributions for (a) $h/J = 0.1$ and (b) $h/J = 0.5$ when $L = 14$ and $\Delta = 0.5$. There is no remarkable difference among the different energy ranges. Even when $h/J = 0.1$, $P(s)$ shows only little difference from $P_{\text{Wig}}(s)$ for the energy range near the edges.

4.6 Summary

For the finite spin- $\frac{1}{2}$ XXZ spin chains with the NNN interaction or with a random magnetic field, we have evaluated characteristic quantities of level statistics such as the level-spacing distribution, the spectral rigidity and the number variance. We have confirmed the correspondence between non-integrability and Wigner behavior in the spectrum. We have also discussed various cases where unexpected non-Wigner behavior appears. Through the numerical results we have obtained the following conjecture: When the symmetry of a finite-size system enhances at some points of the parameter space, the characteristic behavior of level statistics should be given by Poisson-like behavior near some region close to the points. In particular, we have shown that finite-size effects play an important role in the characteristic quantities of level statistics for the XXZ spin chains.

The NNN coupled XXZ chains are integrable for $J_2 = 0$, and their $U(1)$ symmetry extends into $SU(2)$ symmetry at the point of $\Delta_1 = \Delta_2 = 1$. When the parameters are near $J_2 = 0$ and/or $\Delta_1 = \Delta_2 = 1$, the behavior of level statistics is Poisson-like behavior. We have also shown that some unexpected behavior can appear when an extra symmetry is not considered for desymmetrization, such as the case of the spin reversal symmetry in the sector of $S_{\text{tot}}^z = 0$. Here we note that in some cases extra symmetries depend on some parameters as well as some quantum numbers.

For $\Delta = 0$, Poissonian behavior appears in the level statistics of the XXZ spin chains under random magnetic field although the system has the randomness. As Δ increases from zero, $P(s)$ rapidly shifts to the Wigner distribution. The Poissonian behavior of $P(s)$ and $\Delta_3(l)$ have been explained in terms of Anderson localization. For $\Delta \neq 0$, $P(s)$ and $\Delta_3(l)$ strongly depends on L when h is small. When L is finite, $P(s)$ and $\Delta_3(l)$ should show Poisson-like behavior in the small h limit. In the large h limit, however, $P(s)$ and $\Delta_3(l)$ should become close to the Poissonian behavior independent of L .

Chapter 5

Energy Diffusion

In this chapter, we study the dynamical properties of energy spectra. We investigate energy diffusion for next-nearest-neighbor (NNN) coupled XXZ spin chains in the presence of a periodically oscillating magnetic field. Diffusion coefficients are found to obey the power law with respect to both the field strength and driving frequency with its power varying depending on the linear response and non-perturbative regimes [18]. The widths of the linear response and the non-perturbative regimes depend on the strength of frustrations. We have also elucidated a mechanism for oscillation of energy diffusion in the case of weakened frustrations.

5.1 Preliminaries

There exists an accumulation of studies on quantum dynamics of classically chaotic systems, e.g. kicked rotators, kicked spin-tops, hydrogen atoms in time-dependent electric field, and the standard map model, to mention a few [45]. Quantum suppression of energy diffusion, dynamical localization and other signatures of quantum chaos are notable in these dynamics. However, most of the systems treated so far are confined to those with a few degrees-of-freedom, and little attention is paid to dynamics of quantum many-body systems [46, 47, 48] whose adiabatic energy levels are characterized by Gaussian orthogonal ensemble (GOE) spectral statistics, i.e. by a hallmark of quantum chaos. While some important contributions [49, 50, 51, 52, 53, 54, 55] are devoted to dynamics of a kind of many-body systems, those systems are actually described by the random-matrix models, and not by deterministic quantum Hamiltonians. It is highly desirable to explore dynamical behaviors of deterministic quantum many-body systems exhibiting GOE or Gaussian unitary ensemble (GUE) spectral statistics.

On the other hand, the frustrated quantum spin systems have been receiving a wide attention, and we can find their realization in $s = \frac{1}{2}$ antiferromagnetic chains Cu(ampy)Br_2 [11] and $(\text{N}_2\text{H}_5)\text{CuCl}_3$, [12] and in $s = \frac{1}{2}$ triangular antiferromagnets [56].

The high-lying states of these quantum many-body systems deserve being studied in the context of “quantum chaos.” The advantage of the frustrated quantum systems is that one can expect quantum chaotic behaviors appearing already in the low energy region near the ground state [57, 58]. From the viewpoint of real physics of condensed matters, novel features observed in the low-energy region are very important and welcome. Recalling that in most of deterministic Hamiltonian systems quantum chaotic behaviors appear in high-lying states, the role of frustration is essential in the study of quantum dynamics from the ground state of deterministic many-body systems with GOE or GUE level statistics.

In this work, we investigate dynamics of XXZ quantum spin chains which have anti-ferromagnetic exchange interactions for the nearest-neighbor (NN) and the next-nearest-neighbor (NNN) couplings. The NNN couplings cause the frustration, i.e. difficulty in achieving the ground state, thereby attributing a name of frustrated quantum spin chains to these systems. In fact, the level statistics of the NNN coupled XXZ spin chains without an applied magnetic field has been studied intensively in Refs. [15, 17], and it has been shown that GOE behavior, which is typical of quantum chaos, appears already in the low energy region near the ground state.

A natural extension of the research is to investigate dynamics of the frustrated quantum spin chains with an applied periodically oscillating magnetic field. We calculate a time evolution of the system starting from their ground state and analyze the nature of energy diffusion. We shall numerically exhibit the time dependence of energy variance, and show how the diffusion coefficients depend on the coupling constants, the anisotropy parameters, the magnetic field and the frequency of the field. Furthermore, to compare with the energy diffusion in the case of weakened frustrations, we also investigate dynamics of the corresponding energy diffusion in XXZ spin chains with small NNN couplings and/or exchange anisotropy.

The organization of this chapter is as follows: In Sec. 5.2, we shortly explain the idea of energy diffusion. In Sec. 5.3, we briefly describe a numerical approach to obtain the time evolution operator. In Sec. 5.4, we shall show the time dependence of energy variance starting from the ground state of the many-body system and explain a way to evaluate diffusion coefficients. Section 5.5 elucidates how diffusion coefficients depend on field strength and driving frequency. Here the universal power laws are shown to exist in the linear response and non-perturbative regions. Section 5.6 is devoted to a mechanism of oscillation of energy diffusion. We summarize this chapter in Sec. 5.7.

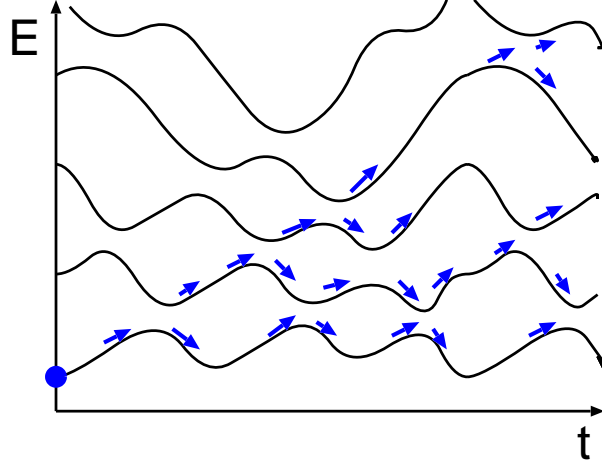


Figure 5.1: Schematic picture of energy spectra.

5.2 What is energy diffusion like?

Let us consider a system which has a time dependent parameter X . The solution of the time-independent Schrödinger equation gives a set of energy levels at a fixed time. The sets of energy levels arranged in time order give adiabatic energy spectra such as Fig. 5.1.

Because of the time-dependent parameter X , the system obeys the time-dependent Schrödinger equation that causes nonadiabatic transitions among energy levels. When the nonadiabatic transitions occur repeatedly, the occupation probabilities of energy levels diffuse. The diffusion of occupation probabilities leads to energy diffusion. The behavior of energy diffusion is determined by the spectral property of the adiabatic energy levels and the changing rate \dot{X} of the parameter.

5.3 Numerical procedure

We give the Hamiltonian for the NN and NNN exchange-coupled spin chain on L sites with a time-periodic oscillating magnetic field as

$$\mathcal{H}(t) = \mathcal{H}_0 + \mathcal{H}_1(t), \quad (5.1)$$

where

$$\begin{aligned} \mathcal{H}_0 = & J_1 \sum_{j=1}^L (S_j^x S_{j+1}^x + S_j^y S_{j+1}^y + \Delta S_j^z S_{j+1}^z) \\ & + J_2 \sum_{j=1}^L (S_j^x S_{j+2}^x + S_j^y S_{j+2}^y + \Delta S_j^z S_{j+2}^z) \\ & - \sum_{j=1}^L B_j^z(0) S_j^z, \end{aligned} \quad (5.2)$$

$$\mathcal{H}_1(t) = \sum_{j=1}^L B_j^z(0) S_j^z - \sum_{j=1}^L B_j^z(t) S_j^z. \quad (5.3)$$

Here, $S^\alpha = \frac{1}{2}\sigma^\alpha$ and $(\sigma^x, \sigma^y, \sigma^z)$ are the Pauli matrices; the periodic boundary conditions (P. B. C.) are imposed. The magnetic field B_j^z on j th site along the z axis is chosen to form a traveling wave:

$$B_j^z(t) = B_0 \sin\left(\omega t - \frac{2\pi j}{L}\right). \quad (5.4)$$

The period of Eq. (5.1) as well as Eq. (5.4) is $T = 2\pi/\omega$. Because of the coexisting spatial P. B. C., however, the effective period of the adiabatic energy spectra is given by $T' = T/L = 2\pi/(\omega L)$. In other words, the period of the Hamiltonian operator is T , and the spectral flow of the eigenvalues has the effective period T' . This periodicity property comes from the traveling-wave form of Eq. (5.4), and is advantageous for our getting a sufficient number of relevant data in each period T .

When $J_1 > 0$ and $J_2 > 0$, the unperturbed Hamiltonian \mathcal{H}_0 without coupling to the magnetic field is translationally invariant and corresponds to a frustrated antiferromagnetic quantum spin model exhibiting GOE level statistics [15, 17]. If $J_2 = 0$ and $B_0 = 0$, it describes an integrable and non-frustrated model. Before calculating energy diffusion, we have to consider the symmetries of the model. We divide the Hamiltonian matrix to some sectors which have the same quantum numbers. In the Hamiltonian Eq.(5.1), total S^z (S_{tot}^z) is conserved. The eigenstates with different S_{tot}^z are uncorrelated. For convenience, we choose the sector of $S_{\text{tot}}^z = 1$. On the other hand, the non-uniform magnetic field breaks the translational symmetry, and leads to mixing between manifolds of different wave-number values.

Before proceeding to consider the time evolution of a wave function, we should note: If we use the original Hamiltonian $\mathcal{H}(t) = \mathcal{H}_0 + \mathcal{H}_1(t)$ as it stands, the mean level spacing of eigenvalues would change depending on J_2 , Δ , and B_0 . To see a universal feature of the energy diffusion, it is essential to scale the Hamiltonian so that the full range of adiabatic energy eigenvalues becomes almost free from these parameters. Noting that this energy range for the original Hamiltonian is of order of L when $J_1 = J_2 = \Delta = 1$, we define the scaled Hamiltonian $H(t) = H_0 + H_1(t)$ so that the full energy range equals L at $t = 0$, which will be used throughout in the text. The Schrödinger equation is given by

$$i\hbar \frac{\partial}{\partial t} |\psi(t)\rangle = H(t) |\psi(t)\rangle = [H_0 + H_1(t)] |\psi(t)\rangle. \quad (5.5)$$

The solution of Eq. (5.5) consists of a sequence of the infinitesimal processes as

$$|\psi(t)\rangle = U(t; t - \Delta t) U(t - \Delta t; t - 2\Delta t) \cdots U(2\Delta t; \Delta t) U(\Delta t; 0) |\psi(0)\rangle. \quad (5.6)$$

The initial state $|\psi(0)\rangle$ is taken to be the ground state, since our concern lies in the dynamical behaviors starting from the many-body ground state. To calculate a time

evolution operator $U(t + \Delta t; t)$ for each short time step Δt , we use the fourth-order decomposition formula for the exponential operator [59]:

$$U(t + \Delta t; t) = S(-ip_5\Delta t/\hbar, t_5)S(-ip_4\Delta t/\hbar, t_4) \cdots S(-ip_1\Delta t/\hbar, t_1), \quad (5.7)$$

where,

$$S(x, t) = \exp\left(\frac{xH_1(t)}{2}\right) \exp(xH_0) \exp\left(\frac{xH_1(t)}{2}\right). \quad (5.8)$$

Here, t_j 's and p_j 's are the following:

$$\begin{aligned} t_j &= t + (p_1 + p_2 + \cdots + p_{j-1} + p_j/2)\Delta t, \\ p &= p_1 = p_2 = p_4 = p_5, \\ &= 0.4144907717943757 \cdots \\ p_3 &= 1 - 4p. \end{aligned} \quad (5.9)$$

The numerical procedure based on the above decompositions is quite effective when $H_1(t)$ and H_0 do not commute and each time step is very small. Our computation below is concerned mainly with the system of $L = 10$, whose $S_{\text{tot}}^z = 1$ manifold involves 210 levels. To check the validity of our assertion, some of the results will be compared to those for the system of $L = 14$ and $S_{\text{tot}}^z = 4$ whose manifold involves 364 levels.

5.4 Time dependence of energy variance

We calculate time evolution of the state and evaluate energy variances at each integer multiple of the effective period $T' = T/L = 2\pi/(\omega L)$. As mentioned already, we choose the ground state as an initial state, following the spirit of real physics of condensed matters. This viewpoint is in contrast to that of the random matrix models where initial states are chosen among high-lying ones [49, 50, 51, 52, 53, 54]. Consequently, the energy variance of our primary concern is the *variance around the ground state energy* E_0 and is defined by

$$\delta E(t)^2 = \langle \psi(t) | [H(t) - E_0]^2 | \psi(t) \rangle. \quad (5.10)$$

Time evolution of $\delta E(t)^2$ is shown in Fig. 5.2. The parameters except for ω are fixed. The larger ω is, the faster the energy diffusion grows, which is consistent with our expectations. The details are explained in Sec. 5.5. A linear growth of $\delta E(t)^2$ in time during the first period can be recognized more clearly for $L = 14$ than for $L = 10$, because the number of data points per period is increased for larger L .

For wide parameter values of the next-nearest-neighbor (NNN) coupling J_2 and the anisotropy parameter Δ , the early stage of quantum dynamics becomes to show the normal diffusion in energy space, i.e. a linear growth of $\delta E(t)^2$ in time. While we investigate this

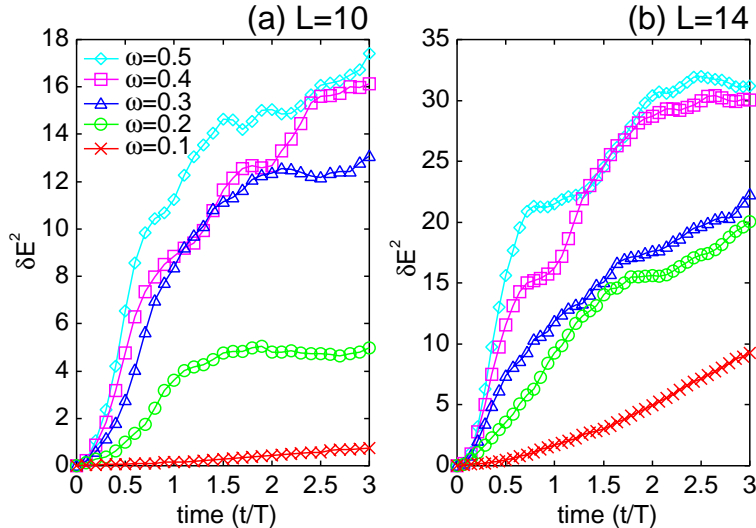


Figure 5.2: Time evolution of energy diffusion for (a) $L = 10$ and (b) $L = 14$ (reprinted from Ref. [18]). The unit of time is the period T . The parameters are the following: $J_1 = J_2 = 1.0$, $\Delta = 0.3$, $B_0 = 1.0$.

normal diffusion process, energy variances will finally saturate because the system size we consider is finite. On the other hand, energy variances can also saturate because of another reason, i.e. the dynamical localization effect. It is associated with a periodic perturbation. In any case, diffusion coefficients have to be determined for times where saturation does not yet occur. We determine the diffusion coefficient D from the fitting

$$\delta E(t)^2 = Dt + \text{const.} \quad (5.11)$$

to some data points around the largest slope in the first period, where the normal diffusion is expected.

5.5 Diffusion coefficients: dependence on field strength and frequency

Since the time evolution of our system starts from the ground state, we consider non-adiabatic regions where inter-level transitions frequently occur. In other words, we suppress a near-adiabatic or the so-called Landau-Zener (LZ) region where the driving frequency ω is much smaller than the mean level spacing divided by Planck constant. Because of a large energy gap between the ground and first excited states, the near-adiabatic region cannot result in the notable energy diffusion and will be left outside a scope of the present study.

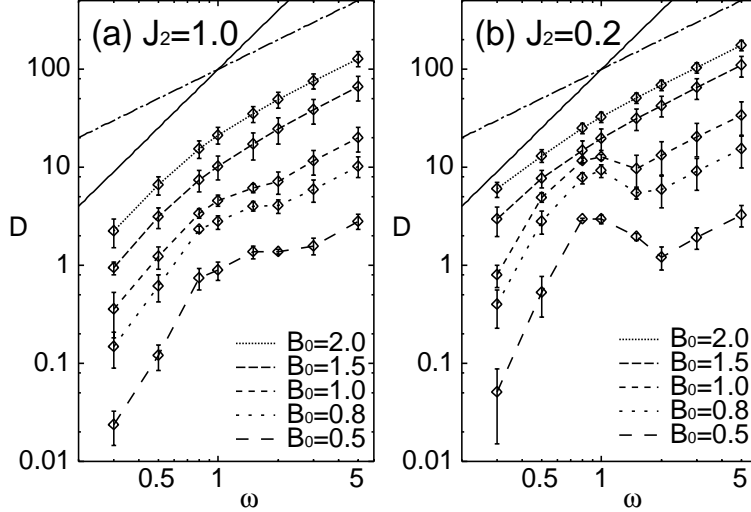


Figure 5.3: Driving frequency dependence of the diffusion coefficients (reprinted from Ref. [18]). The chained line and the solid line are just eye guides for $D \propto \omega^\beta$ with $\beta = 1$ and 2 , respectively. The symbols (\diamond) are the average of the diffusion coefficients calculated for several values of Δ ($0.3 \leq \Delta \leq 0.8$). The parameters are the following: $L = 10$, $J_1 = 1.0$; (a) $J_2 = 1.0$, (b) $J_2 = 0.2$.

Beyond the LZ region, however, so long as the changing rate \dot{X} of a perturbation parameter is not very large,¹ the diffusion coefficient can be calculated using the Kubo formula. We call such a parameter regime “linear response” regime. In the linear response regime, $D \propto \dot{X}^2$ (See, e.g., Refs. [50] and [51]). When \dot{X} is large, however, the perturbation theory fails. We call such a parameter regime “non-perturbative” regime. In the non-perturbative regime, the diffusion coefficient is smaller than that predicted by the Kubo formula [51, 53]. According to Ref. [51], $D \propto \dot{X}^\gamma$ with $\gamma \leq 1$ in the non-perturbative regime. We note that $\dot{X} \propto B_0\omega$ in this work since the perturbation is given by Eq. (5.4). Both Refs. [51] and [53] are based on the random matrix models, which are utterly different from our deterministic one. The discussion about energy diffusion for a random matrix model [51] is briefly reviewed in Appendix E.

Numerical results of diffusion coefficients in Fig. 5.3 are almost consistent with the argument of Ref. [51]. Diffusion coefficients as a function of ω are shown in Fig. 5.3. In Fig. 5.3(a), where $J_2 = 1.0$ (i.e. the fully-frustrated case), D is larger as B_0 is larger for a fixed value of ω . In a small- ω regime, $D \propto \omega^\beta$ with $\beta = 2$, though $\beta > 2$ for small B_0 . The latter is merely attributed to the fact that the perturbation is too small to observe a sufficient energy diffusion when both ω and B_0 are small. In a large- ω regime, $\beta = 1$.

¹More precisely, this phrase means that the time scale upon which the time-dependent Hamiltonian matrix elements decorrelate is much larger than the time scale corresponding to the typical separation of energy levels.

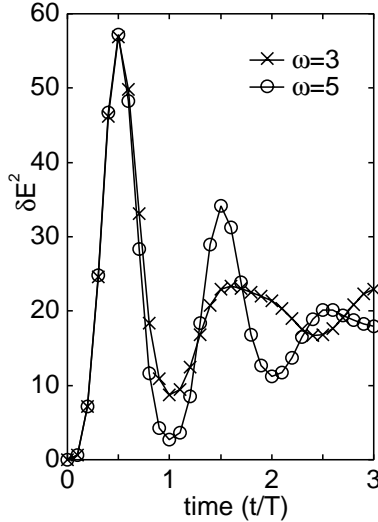


Figure 5.4: Time evolution of energy variance for large ω . The parameters are $L = 10$, $J_1 = J_2 = 1.0$, $\Delta = 0.3$, $B_0 = 2.0$.

Namely, we observe that $\beta = 2$ in the linear response regime and $\beta = 1$ in the non-perturbative regime. In fact, for a large- ω regime, the increase of energy variances per effective period hardly depend on ω until $\delta E(t)^2$ starts to decrease as shown in Fig. 5.4. This explains the observation that $D \propto \omega^\beta$ with $\beta = 1$ in both Fig. 5.3(a) and Fig. 5.3(b). Let us represent the increase of energy variances per effective period as $\Delta(\delta E^2)$. From the definition of D , i.e. Eq. (5.11), $D \propto \Delta(\delta E^2)/T'$. Then we find that $D \propto \omega$ if $\Delta(\delta E^2)$ is constant.

On the other hand, in Fig. 5.3(b) where $J_2 = 0.2$ (i.e. a weakly-frustrated case), the region with $\beta = 1$ expands. For small B_0 , $\beta > 2$ in a small- ω regime. For small B_0 and around $\omega \sim 1$, D seems to decrease rather than increase especially in the case of $J_2 = 0.2$. In fact, the slope of energy variance for large ω is larger than that for small ω in the very early stage of energy diffusion. However, some kind of localization occurs for large ω as shown in Fig. 5.5, which leads to the suppression of D .

It is seen more clearly in Fig. 5.6 how the behavior of D changes between a linear response regime and a non-perturbative regime. The diffusion coefficient D obeys the power law $D \propto (B_0\omega)^\beta$ with its power β being two in the linear response regime and $\beta = 1$ in the non-perturbative regime. For small $B_0\omega$, the power law seems to fail because of some finite-size effects. These universal feature is confirmed in systems of larger size. Actually, D obeys the power law better for $L = 14$ [Fig. 5.6(b)] than $L = 10$ [Fig. 5.6(a)]. In addition, error bars are shorter for $L = 14$ than $L = 10$. Here, we have used the data of $\omega \leq 1$. We cannot expect meaningful results in a large- ω regime since, as mentioned above, energy diffusion is not normal there.

Figure 5.6 suggests that the strength of frustration should affect the range of the

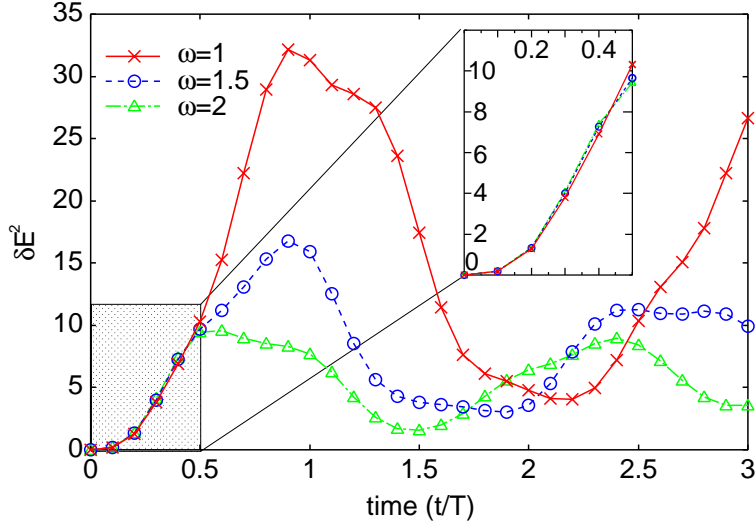


Figure 5.5: Time evolution of energy variance for small B_0 and around $\omega \sim 1$. The parameters are $L = 10$, $J_1 = 1.0$, $J_2 = 0.2$, $\Delta = 0.3$, $B_0 = 0.8$. The inset is the magnified figure of the hatched part.

linear response regime. The linear response regime is shorter for $J_2 = 0.2$ than for $J_2 = 1.0$, while the non-perturbative regime is larger for $J_2 = 0.2$ than for $J_2 = 1.0$. In fact, when $J_2 = 0$ (i.e. the integrable case), $D \propto (B_0\omega)^\beta$ with $\beta = 1$ for almost all the data in the same range of $B_0\omega$ as that of Fig. 5.6.

5.6 Oscillation of energy diffusion in weakly-frustrated cases

We shall now proceed to investigate oscillations of diffusion which occur in the non-perturbative regime of a weakly-frustrated case. Figure 5.7(a) shows an example of oscillatory diffusion for $J_2 = 0.2$, which is compared with a non-oscillatory diffusion for $J_2 = 1.0$. The two examples have the same set of parameters except for J_2 . However, the cases of $J_2 = 1.0$ and $J_2 = 0.2$ are in the linear response regime and in the non-perturbative regime, respectively. The variance for both cases shows normal diffusion at the very early stage of time evolution. For $J_2 = 1.0$, the energy variance seems to saturate after a normal diffusion time. On the contrary, the energy variance for $J_2 = 0.2$ shows large-amplitude oscillations. To investigate more details, we introduce another definition of energy variance:

$$\delta\tilde{E}(t)^2 = \langle \psi(t) | [H(t) - \langle \psi(t) | H(t) | \psi(t) \rangle]^2 | \psi(t) \rangle. \quad (5.12)$$

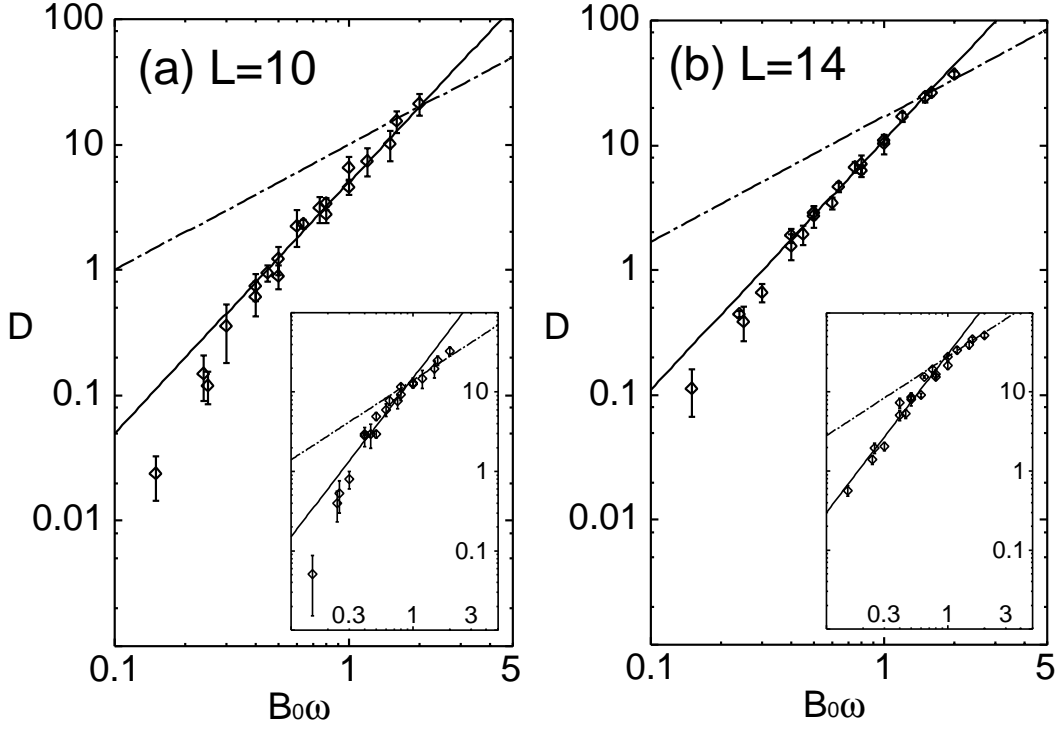


Figure 5.6: Dependence of the diffusion coefficients on the product of field strength B_0 and driving frequency ω for (a) $L = 10$ and (b) $L = 14$ (reprinted from Ref. [18]). The symbols (\diamond) are the average of the diffusion coefficient calculated for several values of Δ ($0.3 \leq \Delta \leq 0.8$). For the main panels, $J_1 = J_2 = 1.0$; for the inset, $J_1 = 1.0$ and $J_2 = 0.2$. The chained line and the solid line are just eye guides for $D \propto (B_0\omega)^\beta$ with $\beta = 1$ and 2 , respectively. Some error bars are too short to see.

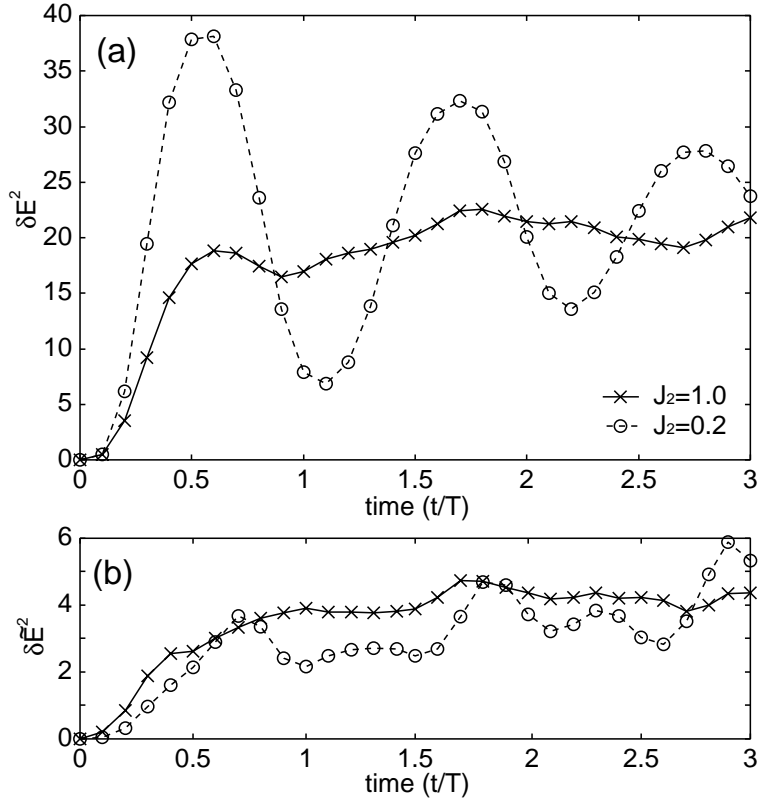


Figure 5.7: Examples for time evolution of energy variances : (a) $\delta E(t)^2$ and (b) $\delta \tilde{E}(t)^2$ (see text) (reprinted from Ref. [18]). Solid lines are for $J_2 = 1.0$; Broken lines, $J_2 = 0.2$. The parameters are the following: $L = 10$, $J_1 = 1.0$, $\Delta = 0.3$, $B_0 = 1.5$, $\omega = 0.5$.

This follows a standard definition of the variance and quantifies the degree of energy diffusion around the *time-dependent expectation* of the energy Hamiltonian. The time evolutions of $\delta\tilde{E}(t)^2$ corresponding to that of $\delta E(t)^2$ are shown in Fig. 5.7(b). In the fully-frustrated case ($J_2 = 1.0$), the profile of $\delta\tilde{E}(t)^2$ is similar to that of $\delta E(t)^2$. This observation indicates that an occupation probability spread over the whole levels after normal diffusion of energy.

On the contrary, in a weakly-frustrated case ($J_2 = 0.2$) in Fig. 5.7, $\delta\tilde{E}(t)^2$ shows small-amplitude oscillations reflecting the large-amplitude oscillations of $\delta E(t)^2$. Most part of $\delta\tilde{E}(t)^2$ for $J_2 = 0.2$ is smaller than that for $J_2 = 1.0$. Furthermore, minima of $\delta\tilde{E}(t)^2$ come just before minima and maxima of $\delta E(t)^2$. These observations indicates the following: an occupation probability, which is diffusing slowly, clustering around the expectation of energy oscillates together with the expectation in the energy space. To make the picture of such behavior clearer, let us consider an occupation probability described by

$$P_t(E_n) = |\langle\phi_n|\psi(t)\rangle|^2, \quad (5.13)$$

where $|\phi_n\rangle$ is the n th excited eigenstate of \mathcal{H}_0 :

$$H_0|\phi_n\rangle = E_n|\phi_n\rangle. \quad (5.14)$$

When $t = 0$, $P_t(E_n)$ is given by the Kronecker delta: $P_0(E_n) = \delta_{E_n, E_0}$, where E_0 is the energy of the ground state at $t = 0$. As t increases, $P_t(E_n)$ forms a wave packet in energy space and moves to higher levels. When the wave packet reaches some highest levels, it reflects like a soliton and moves back to lower levels. Such behavior is repeated, although the wave packet of $P_t(E_n)$ broadens slowly. We have actually watched this soliton-like behavior of $P_t(E_n)$ in a form of an animation.

The picture discussed above is also supported by the adiabatic energy spectra in Fig. 5.8. Figures 5.8(a) and 5.8(b) correspond to fully- and weakly-frustrated cases, respectively. Much more sharp avoided crossings appear in Fig. 5.8(b) than Fig. 5.8(a). Some energy levels appear to be crossing, although they are very close and never crossing in fact. At a sharp-avoided-crossing point, Landau-Zener formula for two adjacent levels is applicable. Then the nonadiabatic transition leads to one-way transfer of a population from a level to its partner, failing to result in the energy diffusion. For small- J_2 , therefore, successive sharp avoided crossings can suppress diffusion of energy.

We believe that large-amplitude oscillations of $\delta E(t)^2$ should be one of characteristic features of the non-perturbative regime in this finite frustrated spin system. In fact, similar oscillations of energy variance are seen for large ω and large B_0 even when $J_2 = 1.0$ though the energy variance rapidly converges after one or two periods. For example, such a behavior of energy variance is seen in Fig. 5.4. How long such oscillations continue should depend mainly on J_2 .

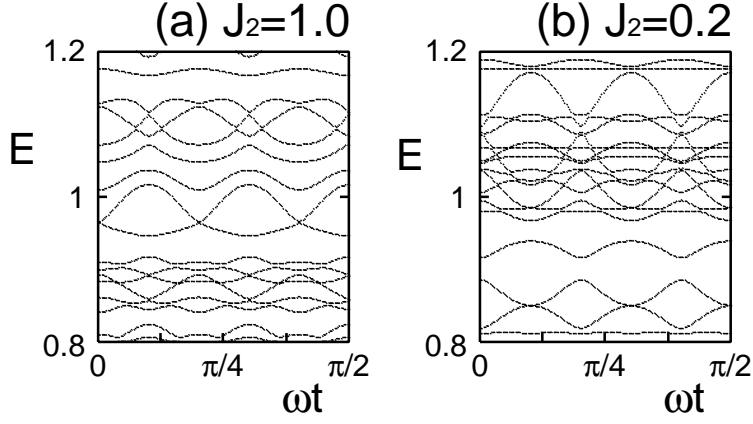


Figure 5.8: Parts of energy spectra depending on adiabatically fixed time t with $0 \leq t \leq T/4$ (reprinted from Ref. [18]). Effective period is $\omega T' = 2\pi/10$. The parameters are the following: $L = 10$, $J_1 = 1.0$, $\Delta = 0.3$, $B_0 = 0.8$; (a) $J_2 = 1.0$, (b) $J_2 = 0.2$.

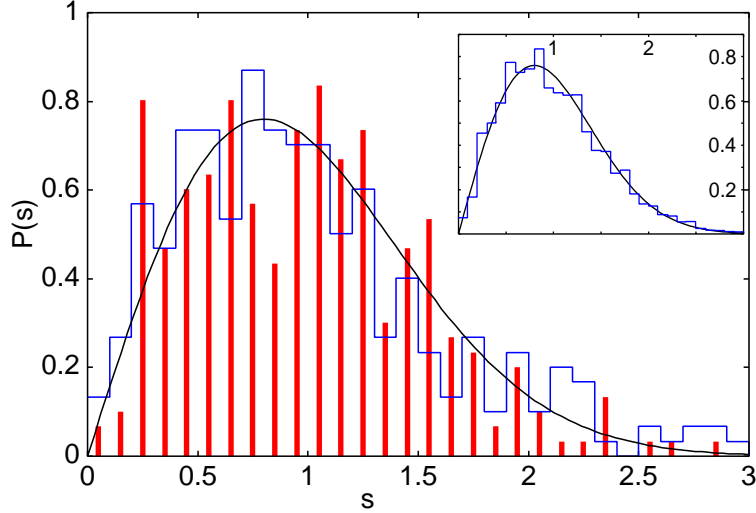


Figure 5.9: Level-spacing distributions at $t = \pi/4$ for lowest 300 levels from the ground state (about 10% of all 3003 levels) (reprinted from Ref. [18]). Blue histogram is for $J_2 = 1.0$; Red bars, $J_2 = 0.2$; Solid curve, GOE spectral statistics. The other parameters are the following: $L = 14$, $S_{\text{tot}}^z = 1$, $J_1 = 1.0$, $\Delta = 0.3$, $B_0 = 0.8$. The inset is for all levels when $J_2 = 1.0$. The numerical methods to obtain the level-spacing distributions are referred in Refs. [15, 17].

It is a notable fact that, common to both $J_2 = 1.0$ and $J_2 = 0.2$, the level-spacing distributions in Fig. 5.9 show GOE behavior. This GOE behavior in the adiabatic energy spectra appears for an arbitrary fixed time except for special points such as $t = T = 2\pi/\omega$. This fact suggests that dynamics can reveal some various generic features of quantum many-body systems which can never be explained by level statistics. The level-spacing distributions in Fig. 5.9 convey another crucial fact: they have been calculated for low energy levels because our interest is in the low energy region around the ground state. We have confirmed that the level-spacing distributions for all energy levels in the inset is also described by GOE spectral statistics. It is typical of this frustrated spin system that GOE level statistics is observed already in the low energy region [17]. We have already discussed homogeneity of the behavior of level statistics throughout the spectrum in Chapter 4. One may wonder why $P(s)$ for $J_2 = 0.2$ shows Poisson-like behavior in Fig. 4.9 (b) and GOE behavior in Fig. 5.9. This is because a magnetic field is added in this model, Eq. (5.1).

5.7 Summary

We have explored the energy diffusion from the ground state in frustrated quantum XXZ spin chains under the applied oscillating magnetic field. In a wide parameter region of next-nearest-neighbor (NNN) coupling J_2 and exchange anisotropy Δ , the diffusion is normal until the dynamical saturation begins to prevail. Diffusion coefficients D obeys the power law with respect to both the field strength and driving frequency with its power being two in the linear response regime and equal to unity in the non-perturbative regime. In the case of weakened frustrations with small- J_2 we find oscillation of energy diffusion, which is attributed to a non-diffusive and ballistic nature of the underlying energy diffusion. In this way, the energy diffusion reveals generic features of the frustrated quantum spin chains, which cannot be captured by the analysis of level statistics.

Chapter 6

Conclusions

In this thesis, we have discussed the properties in the energy spectra of XXZ spin chains. The XXZ spin chains are basic quantum spin chains and related to the most important families of integrable spin systems. We have studied level crossings, level bifurcations, and level statistics for the statistical properties, and energy diffusion for the dynamical properties.

To study level crossings, the eigenvalues has been calculated for 3-site, 4-site and 6-site XXZ spin chains. We have observed many counterexamples to the noncrossing rule in the spectra of the integrable XXZ spin chains. Several level crossings are related to the sl_2 loop algebra symmetry. The symmetry of a XXZ spin chain enhances at some particular values of the anisotropy parameter, where multiple level crossings are observed.

Branches have been observed in the flow of eigenvalues for the inhomogeneous transfer matrix of the XXZ spin chain. Those branches can be called “level bifurcations”. The appearance of the branches has been confirmed through the Bethe ansatz method. The observation of level bifurcations may contribute to the development on the exact calculation of thermodynamic quantities for the XXZ spin chain. The transfer matrix of a spin chain is often used to calculate the thermodynamical quantities of it.

Level statistics has been studied for XXZ spin chains with next-nearest-neighbor (NNN) coupling or with a random magnetic field. We have confirmed correspondence between non-integrability and Wigner behavior in the energy spectra and shown how finite-size effects affect the level statistics of the finite-size XXZ spin chains. Studying the finite-size effects on the level statistics should be useful for investigating similar systems or for calculating quantities such as energy diffusion. It has also been suggested that incomplete desymmetrization can cause unexpected behavior in level statistics. Study of the unexpected behavior should be helpful to resolve similar behavior of level statistics even in other systems.

Energy diffusion has been investigated to study the dynamical properties for NNN coupled XXZ spin chains under a periodically oscillating magnetic field. We have observed

that diffusion coefficients D shows a universal behavior: D obeys the power law with respect to both the field strength and driving frequency. The observation may lead to some new nature of frustrated quantum spin systems. For weakened frustrations, we have found the existence of small fluctuation of diffusion coefficients and the non-diffusive behavior of the energy diffusion. The behavior should suggest that energy diffusion reveals some features, which cannot be captured by the analysis of level statistics for the XXZ spin chains.

In this thesis, we have focused on the properties in the energy spectra of XXZ spin chains. We believe that the above intensive study on the XXZ spin chains is very useful for investigating other finite quantum spin chains or finite low-dimensional quantum systems.

Acknowledgements

I wish to thank my supervisor, Professor Tetsuo Deguchi, for his advice, guidance, discussion, concern and encouragement.

I would like to thank Professor Fumiaki Shibata and Professor Katsuyoshi Kobayashi for useful comments and suggestion.

I am grateful to Professor Katsuhiro Nakamura of Osaka City University for collaboration in the work of Chapter 5 and for useful discussion on the work of Chapter 4. I also wish to acknowledge valuable discussion on the work of Chapter 4 with Professor Takeo Kato of University of Tokyo. I also thank to the staffs and students of Prof. Nakamura's Laboratory at Osaka City University.

I would like to express my special thanks to my friends whom I met at Bussei-Wakate Summer School and Butsurikko-Club Seminar. In particular, I would like to thank Mr. Hirofumi Watanabe for telling me how to perform unfolding.

I wish to thank Professor Yshai Avishai of Ben-Gurion University in Israel for valuable comments and suggestion.

I wish to acknowledge the Yukawa Institute for Theoretical Physics at Kyoto University. Discussions during the YITP workshop YITP-W-03-16 on "Quantum Mechanics and Chaos: From Fundamental Problems through Nanosciences" were useful to complete the work of Chapter 4.

This study is partially supported by Hayashi Memorial Foundation for Female Natural Scientists.

Finally, I wish to thank the members of Deguchi Laboratory, my friends and my family for support and encouragement.

Appendix A

Hamiltonian Matrix

Let us show how to describe Eq. (2.1) in the form of the Hamiltonian matrix. The matrices on the j th site, σ_j^\pm and σ_j^z , are given by

$$\sigma_j^\alpha = \underbrace{I \otimes \cdots \otimes I}_{j-1} \otimes \underbrace{\sigma_j^\alpha}_{j\text{th}} \otimes \underbrace{I \otimes \cdots \otimes I}_{N-j}. \quad (\text{A.1})$$

Here,

$$\sigma^+ = \begin{pmatrix} 0 & 1 \\ 0 & 0 \end{pmatrix}, \quad \sigma^- = \begin{pmatrix} 0 & 0 \\ 1 & 0 \end{pmatrix}, \quad \sigma^z = \begin{pmatrix} 1 & 0 \\ 0 & -1 \end{pmatrix}, \quad I = \begin{pmatrix} 1 & 0 \\ 0 & 1 \end{pmatrix}. \quad (\text{A.2})$$

Now we remember

$$A \otimes B = \begin{pmatrix} a_{11} & a_{12} \\ a_{21} & a_{22} \end{pmatrix} \otimes \begin{pmatrix} b_{11} & b_{12} \\ b_{21} & b_{22} \end{pmatrix} = \left(\begin{array}{cc|cc} a_{11}b_{11} & a_{11}b_{12} & a_{12}b_{11} & a_{12}b_{12} \\ a_{11}b_{21} & a_{11}b_{22} & a_{12}b_{21} & a_{12}b_{22} \\ \hline a_{21}b_{11} & a_{21}b_{12} & a_{22}b_{11} & a_{22}b_{12} \\ a_{21}b_{21} & a_{21}b_{22} & a_{22}b_{21} & a_{22}b_{22} \end{array} \right) \quad (\text{A.3})$$

For example, when $L = 3$, Eq. (2.1) is described by

$$\mathcal{H} = \frac{J}{4} \begin{pmatrix} 3\Delta & 0 & 0 & 0 & 0 & 0 & 0 & 0 \\ 0 & -\Delta & 2 & 0 & 2e^{i\phi} & 0 & 0 & 0 \\ 0 & 2 & -\Delta & 0 & 2 & 0 & 0 & 0 \\ 0 & 0 & 0 & -\Delta & 0 & 2 & 2e^{i\phi} & 0 \\ 0 & 2e^{-i\phi} & 2 & 0 & -\Delta & 0 & 0 & 0 \\ 0 & 0 & 0 & 2 & 0 & -\Delta & 2 & 0 \\ 0 & 0 & 0 & 2e^{-i\phi} & 0 & 2 & -\Delta & 0 \\ 0 & 0 & 0 & 0 & 0 & 0 & 0 & 3\Delta \end{pmatrix}. \quad (\text{A.4})$$

Here, we give the base vectors by $|\uparrow\uparrow\uparrow\rangle, |\uparrow\uparrow\downarrow\rangle, |\uparrow\downarrow\uparrow\rangle, \dots, |\downarrow\downarrow\downarrow\rangle$. Namely,

$$\begin{aligned}
 |\uparrow\uparrow\uparrow\rangle &= \begin{pmatrix} 1 \\ 0 \end{pmatrix} \otimes \begin{pmatrix} 1 \\ 0 \end{pmatrix} \otimes \begin{pmatrix} 1 \\ 0 \end{pmatrix} = \begin{pmatrix} 1 \\ 0 \\ 0 \\ 0 \end{pmatrix} \otimes \begin{pmatrix} 1 \\ 0 \end{pmatrix} = \begin{pmatrix} 1 \\ 0 \\ 0 \\ 0 \\ 0 \\ 0 \\ 0 \\ 0 \end{pmatrix}, \\
 |\uparrow\uparrow\downarrow\rangle &= \begin{pmatrix} 1 \\ 0 \end{pmatrix} \otimes \begin{pmatrix} 1 \\ 0 \end{pmatrix} \otimes \begin{pmatrix} 0 \\ 1 \end{pmatrix} = \begin{pmatrix} 1 \\ 0 \\ 0 \\ 0 \end{pmatrix} \otimes \begin{pmatrix} 0 \\ 1 \end{pmatrix} = \begin{pmatrix} 0 \\ 1 \\ 0 \\ 0 \\ 0 \\ 0 \\ 0 \\ 0 \end{pmatrix}, \\
 |\uparrow\downarrow\uparrow\rangle &= \begin{pmatrix} 1 \\ 0 \end{pmatrix} \otimes \begin{pmatrix} 0 \\ 1 \end{pmatrix} \otimes \begin{pmatrix} 1 \\ 0 \end{pmatrix} = \begin{pmatrix} 0 \\ 1 \\ 0 \\ 0 \end{pmatrix} \otimes \begin{pmatrix} 1 \\ 0 \end{pmatrix} = \begin{pmatrix} 0 \\ 0 \\ 1 \\ 0 \\ 0 \\ 0 \\ 0 \\ 0 \end{pmatrix}, \dots \quad (\text{A.5})
 \end{aligned}$$

Appendix B

Jordan-Wigner and Fourier Transformations

Let us rewrite Eq. (4.3) by

$$\begin{aligned}
\mathcal{H} &= \mathcal{H}_1 + \mathcal{H}_2 \\
&= J_1 \sum_{l=1}^L (S_l^x S_{l+1}^x + S_l^y S_{l+1}^y + \Delta_1 S_l^z S_{l+1}^z) \\
&\quad + J_2 \sum_{l=1}^L (S_l^x S_{l+2}^x + S_l^y S_{l+2}^y + \Delta_2 S_l^z S_{l+2}^z),
\end{aligned} \tag{B.1}$$

where \mathcal{H}_1 is the term containing nearest-neighbor couplings and \mathcal{H}_2 is the term containing next-nearest-neighbor couplings. We define the Jordan-Wigner transformation by

$$\sigma_l^- = \exp\left(-i\pi \sum_{j=1}^{l-1} c_j^\dagger c_j\right) c_l^\dagger, \tag{B.2}$$

$$\sigma_l^+ = \exp\left(i\pi \sum_{j=1}^{l-1} c_j^\dagger c_j\right) c_l, \tag{B.3}$$

$$\sigma_l^z = 2\sigma_l^+ \sigma_l^- - 1 = 1 - 2\sigma_l^- \sigma_l^+, \tag{B.4}$$

where c_j^\dagger and c_j are the creation and annihilation operators of fermions on j th site. Under the Jordan-Wigner transformation, \mathcal{H}_1 is written by

$$\begin{aligned}
\mathcal{H}_1 &= \frac{J_1}{4} \Delta_1 \left(L - 2 \sum_{l=1}^L c_l^\dagger c_l \right) \\
&\quad + \frac{J_1}{4} \sum_{l=1}^{L-1} [2(c_l^\dagger c_{l+1} + c_{l+1}^\dagger c_l) + \Delta_1 (4c_l^\dagger c_l c_{l+1}^\dagger c_{l+1} - 2c_{l+1}^\dagger c_{l+1})] \\
&\quad + \frac{J_1}{4} [2(c_L^\dagger c_{L+1} + c_{L+1}^\dagger c_L) + \Delta_1 (4c_L^\dagger c_L c_{L+1}^\dagger c_{L+1} - 2c_{L+1}^\dagger c_{L+1})].
\end{aligned} \tag{B.5}$$

Here, we consider periodic boundary conditions ($\sigma_{L+1}^\pm = \sigma_1^\pm$):

$$\begin{aligned}
c_{L+1} &= \exp\left(-i\pi \sum_{j=1}^L \sigma_j^- \sigma_j^+\right) \sigma_{L+1}^+ = \exp\left(-\frac{i\pi L}{2} + \frac{i\pi}{2} \sum_{j=1}^L \sigma_j^z\right) \sigma_1^+ \\
&= \sigma_1^+ \exp\left[i\pi \left(-\frac{L}{2} + S_{\text{tot}}^z + 1\right)\right], \\
c_{L+1}^\dagger &= \exp\left(i\pi \sum_{j=1}^L \sigma_j^- \sigma_j^+\right) \sigma_{L+1}^- = \exp\left(\frac{i\pi L}{2} - \frac{i\pi}{2} \sum_{j=1}^L \sigma_j^z\right) \sigma_1^- \\
&= \sigma_1^- \exp\left[i\pi \left(\frac{L}{2} - S_{\text{tot}}^z + 1\right)\right],
\end{aligned} \tag{B.6}$$

where we use $e^{S_1^z} \sigma_1^\pm = \sigma_1^\pm e^{S_1^z \pm 1}$. Since $\sigma_1^+ = c_1$, $\sigma_1^- = c_1^\dagger$, and $S_{\text{tot}}^z = (L - M)/2 - M/2 = L/2 - M$, where M is the number of fermions, we have

$$c_{L+1} = -(-1)^M c_1, \quad c_{L+1}^\dagger = -(-1)^M c_1^\dagger. \tag{B.7}$$

Therefore, \mathcal{H}_1 is rewritten by

$$\begin{aligned}
\mathcal{H}_1 &= \frac{J_1}{4} \Delta_1 \left[L + \sum_{l=1}^L (4c_l^\dagger c_l c_{l+1}^\dagger c_{l+1} - 4c_l^\dagger c_l) \right] \\
&+ \frac{J_1}{4} \cdot 2 \left[\sum_{l=1}^{L-1} (c_l^\dagger c_{l+1} + c_{l+1}^\dagger c_l) - (-1)^M (c_L^\dagger c_1 + c_1^\dagger c_L) \right].
\end{aligned} \tag{B.8}$$

Now, we define the Fourier transformation as

$$c_l = \frac{1}{\sqrt{L}} \sum_k \hat{c}_k e^{ikl}, \tag{B.9}$$

$$c_l^\dagger = \frac{1}{\sqrt{L}} \sum_k \hat{c}_k^\dagger e^{-ikl}. \tag{B.10}$$

Here, k takes $(2\pi/L) \times$ (an integer) for odd M and $(2\pi/L) \times$ (a half-integer) for even M , and $0 \leq k < 2\pi$. After the Fourier transformation,

$$\begin{aligned}
\mathcal{H}_1 &= \frac{J_1}{4} \Delta_1 L + J_1 \sum_k (\cos k - \Delta_1) \hat{c}_k^\dagger \hat{c}_k \\
&- \frac{J_1 \Delta_1}{L} \sum_{k_1, k_2, k_3, k_4} \delta_{k_1+k_2, k_3+k_4} \exp[-i(k_2 - k_4)] \hat{c}_{k_1}^\dagger \hat{c}_{k_2}^\dagger \hat{c}_{k_3} \hat{c}_{k_4},
\end{aligned} \tag{B.11}$$

where

$$\delta_{k_1+k_2, k_3+k_4} = \begin{cases} 1 & \text{when } k_1 + k_2 \pmod{2\pi} = k_3 + k_4 \pmod{2\pi}. \\ 0 & \text{otherwise.} \end{cases} \tag{B.12}$$

Considering combination of k 's, we can rewrite Eq. (B.11) by

$$\begin{aligned}
\mathcal{H}_1 &= J_1 \Delta_1 \left(\frac{L}{4} - M \right) + J_1 \sum_k \cos k \cdot \hat{c}_k^\dagger \hat{c}_k \\
&- \frac{2J_1 \Delta_1}{L} \sum_{\substack{k_1 < k_2 \\ k_3 > k_4}} \delta_{k_1+k_2, k_3+k_4} [\cos(k_2 - k_4) - \cos(k_2 - k_3)] \hat{c}_{k_1}^\dagger \hat{c}_{k_2}^\dagger \hat{c}_{k_3} \hat{c}_{k_4}.
\end{aligned} \tag{B.13}$$

In the same way, \mathcal{H}_2 can be rewritten by

$$\begin{aligned}
\mathcal{H}_2 &= J_2 \Delta_2 \left(\frac{L}{4} - M \right) + J_2 \sum_k \cos 2k \cdot \hat{c}_k^\dagger \hat{c}_k \\
&+ \frac{2J_2}{L} \sum_{\substack{k_1 < k_2 \\ k_3 > k_4}} \delta_{k_1+k_2, k_3+k_4} [\cos(k_1 + k_3) + \cos(k_2 + k_4) \\
&\quad - \cos(k_1 + k_4) - \cos(k_2 + k_3)] \hat{c}_{k_1}^\dagger \hat{c}_{k_2}^\dagger \hat{c}_{k_3} \hat{c}_{k_4} \\
&- \frac{2J_2 \Delta_2}{L} \sum_{\substack{k_1 < k_2 \\ k_3 > k_4}} \delta_{k_1+k_2, k_3+k_4} \{ \cos [2(k_2 - k_4)] - \cos [2(k_2 - k_3)] \} \hat{c}_{k_1}^\dagger \hat{c}_{k_2}^\dagger \hat{c}_{k_3} \hat{c}_{k_4}. \quad (\text{B.14})
\end{aligned}$$

Appendix C

Spin reversal symmetry on momentum-based fermions

Let us find the momentum-based expression of the mapping corresponding to the spin reversal transformation ($S_j^\pm \rightarrow S_j^\mp$, $S_j^z \rightarrow -S_j^z$). According to Eqs. (B.2), (B.3), (B.9), and (B.10),

$$\hat{c}_k = \frac{1}{\sqrt{L}} \sum_{l=1}^L \exp(-ikl) \exp\left(-i\pi \sum_{j=1}^{l-1} \sigma_j^- \sigma_j^+\right) \sigma_l^+, \quad (\text{C.1})$$

$$\hat{c}_k^\dagger = \frac{1}{\sqrt{L}} \sum_{l=1}^L \exp(ikl) \exp\left(i\pi \sum_{j=1}^{l-1} \sigma_j^- \sigma_j^+\right) \sigma_l^-. \quad (\text{C.2})$$

Under the transformation $\sigma_l^\pm \rightarrow \sigma_l^\mp$, Eq. (C.1) is transformed as the following.

$$\begin{aligned} \hat{c}_k &\rightarrow \frac{1}{\sqrt{L}} \sum_{l=1}^L \exp(-ikl) \exp\left(-i\pi \sum_{j=1}^{l-1} \sigma_j^+ \sigma_j^-\right) \sigma_l^- \\ &= \frac{1}{\sqrt{L}} \sum_{l=1}^L \exp(-ikl) \exp\left[-i\pi \sum_{j=1}^{l-1} (I_j - \sigma_j^- \sigma_j^+)\right] \sigma_l^- \\ &= \frac{1}{\sqrt{L}} \sum_{l=1}^L \exp[-ikl - i\pi(l-1)] \exp\left(i\pi \sum_{j=1}^{l-1} \sigma_j^- \sigma_j^+\right) \sigma_l^-, \end{aligned} \quad (\text{C.3})$$

where I_j is the unit matrix. Now, considering $e^{2\pi il} = 1$, where l is an integer, we can find that

$$\begin{aligned} \exp[-ikl - i\pi(l-1)] &= \exp[-ikl - i\pi(l-1) + 2\pi il] = \exp[i(\pi - k)l + i\pi] \\ &= -\exp[i(\pi - k)l]. \end{aligned} \quad (\text{C.4})$$

Therefore, Eq. (C.3) is rewritten as

$$\hat{c}_k \rightarrow -\frac{1}{\sqrt{L}} \sum_{l=1}^L \exp[i(\pi - k)l] \exp\left(i\pi \sum_{j=1}^{l-1} \sigma_j^- \sigma_j^+\right) \sigma_l^- = -\hat{c}_{\pi-k}^\dagger. \quad (\text{C.5})$$

In the same way, we can show

$$\hat{c}_k^\dagger \rightarrow -\hat{c}_{\pi-k}. \quad (\text{C.6})$$

Appendix D

Spin reversal operation on the vacuum state

Let us introduce the following matrix:

$$U_s = \prod_{j=1}^L \sigma_j^x. \quad (\text{D.1})$$

We may express the spin reversal operation Eq. (4.5) as follows

$$\begin{aligned} U_s S_j^\pm U_s^{-1} &= S_j^\mp, & U_s S_j^z U_s^{-1} &= -S_j^z \\ U_s \hat{c}_k^\dagger U_s^{-1} &= -\hat{c}_{\pi-k}, & U_s \hat{c}_k U_s^{-1} &= -\hat{c}_{\pi-k}^\dagger. \end{aligned} \quad (\text{D.2})$$

We thus have

$$U_s |0\rangle = \prod_{j=1}^L \sigma_j^x |0\rangle = \sigma_1^- \sigma_2^- \cdots \sigma_L^- |0\rangle \quad (\text{D.3})$$

Applying the Jordan-Wigner transformation and substituting c_ℓ^\dagger 's with \hat{c}_k^\dagger 's through Eqs. (B.9) and (B.10), we have

$$\begin{aligned} \sigma_1^- \sigma_2^- \cdots \sigma_L^- |0\rangle &= c_1^\dagger c_2^\dagger \cdots c_L^\dagger |0\rangle \\ &= \frac{1}{L^{L/2}} \sum_{k_1} \cdots \sum_{k_L} e^{-i(1k_1+2k_2+\cdots+Lk_L)} \hat{c}_{k_1}^\dagger \hat{c}_{k_2}^\dagger \cdots \hat{c}_{k_L}^\dagger |0\rangle \\ &= \frac{1}{L^{L/2}} \left(\sum_{P \in \mathcal{S}_L} e^{(-i \sum_{j=1}^L j k_{Pj})} \epsilon_P \right) \hat{c}_{q_1}^\dagger \hat{c}_{q_2}^\dagger \cdots \hat{c}_{q_L}^\dagger |0\rangle \end{aligned} \quad (\text{D.4})$$

Thus we have the expression Eq. (4.8) of the phase factor A_L . Here we recall that $q_j = (2\pi/L)j$ for $j = 1, 2, \dots, L$ for odd M , and $q_j = (2\pi/L)(j - 1/2)$ for $j = 1, 2, \dots, L$ for even M . We also recall that M denotes the number of down-spins in the sector.

We now calculate the expression Eq. (4.9) for the phase factor A_L . We take a vector $|v\rangle$ with $S_{\text{tot}}^z = 0$ as follows. When M is odd, we introduce $\ell = (M - 1)/2$ and we define $|v\rangle$ by

$$|v\rangle = \left(\hat{c}_1^\dagger \hat{c}_2^\dagger \cdots \hat{c}_\ell^\dagger \right) \cdot \left(\hat{c}_{-\ell}^\dagger \cdots \hat{c}_{-2}^\dagger \hat{c}_{-1}^\dagger \right) \cdot \hat{c}_0^\dagger |0\rangle$$

Here \hat{c}_j^\dagger denotes \hat{c}_k^\dagger with $k = (2\pi/L)j$. When M is even, we take $\ell = M/2$, and we define $|v\rangle$ by

$$|v\rangle = \left(\hat{c}_{1/2}^\dagger \hat{c}_{3/2}^\dagger \cdots \hat{c}_{\ell-1/2}^\dagger\right) \cdot \left(\hat{c}_{-(\ell-1/2)}^\dagger \cdots \hat{c}_{-3/2}^\dagger \hat{c}_{-1/2}^\dagger\right) |0\rangle$$

Here $\hat{c}_{j+1/2}^\dagger$ denotes \hat{c}_k^\dagger with $k = (2\pi/L)(j+1/2)$. Through the operation Eq. (4.6) we can show that $U_s|v\rangle = (-1)^{\ell+1}A_L|v\rangle$ for M odd and $U_s|v\rangle = (-1)^\ell A_L|v\rangle$ for M even. Thus, we have at least $U_s|v\rangle = \pm|v\rangle$.

Let us show that $U_s|v\rangle = +|v\rangle$ for both odd M and even M cases. First we note that $U_s c_1^\dagger c_2^\dagger \cdots c_{L/2}^\dagger |0\rangle = c_{L/2+1}^\dagger c_{L/2+2}^\dagger \cdots c_L^\dagger |0\rangle$. Second, expanding the vector $|v\rangle$ in terms of $c_{j_1}^\dagger c_{j_2}^\dagger \cdots c_{j_{L/2}}^\dagger |0\rangle$ with $1 \leq j_1 < j_2 < \cdots < j_{L/2} \leq L$, we can show that the coefficient of $c_1^\dagger c_2^\dagger \cdots c_{L/2}^\dagger |0\rangle$ in the expansion is equal to that of $c_{L/2+1}^\dagger c_{L/2+2}^\dagger \cdots c_L^\dagger |0\rangle$. Therefore we have $U_s|v\rangle = +|v\rangle$.

Thus, we obtain the expression Eq. (4.9) for the phase factor A_L .

Appendix E

Energy diffusion for a random matrix model

Here, we review the discussion of energy diffusion according to Ref. [51]. First of all, we expand the wave function in an adiabatic basis:

$$|\psi(t)\rangle = \sum_n a_n(t) \exp[-i\theta_n(t)] |\phi_n(t)\rangle, \quad (\text{E.1})$$

$$\theta_n(t) = \frac{1}{\hbar} \int_0^t dt' E_n(t'). \quad (\text{E.2})$$

Here, $|\phi_n(t)\rangle$ and $E_n(t)$ are the eigenstates and the eigenvalues of the instantaneous Hamiltonian, respectively:

$$H(t)|\phi_n(t)\rangle = E_n(t)|\phi_n(t)\rangle. \quad (\text{E.3})$$

Substituting Eq. (E.1) into the time-dependent Schrödinger equation and using Eq. (E.2), we obtain the equation for $a_n(t)$,

$$\dot{a}_n = \dot{X} \sum_{m \neq n} \frac{\langle \phi_n | \frac{\partial H}{\partial X} | \phi_m \rangle}{E_m - E_n} \exp[i(\theta_n - \theta_m)] a_m. \quad (\text{E.4})$$

To analyze Eq. (E.4), we specify some information about the energies $E_n(t)$ and the matrix elements $(\partial H / \partial X)_{nm}(t) = \langle \phi_n | (\partial H / \partial X) | \phi_m \rangle$. The off-diagonal matrix elements are Gaussian distributed with mean value zero and with a variance σ^2 which is defined by

$$\sigma^2(E, \Delta E) = \frac{1}{\rho^2(E)} \sum_n \sum_{m \neq n} \left| \left(\frac{\partial H}{\partial X} \right)_{nm} \right|^2 \delta_\epsilon \left[E - \frac{1}{2}(E_n + E_m) \right] \delta_\epsilon [\Delta E - (E_n - E_m)], \quad (\text{E.5})$$

where the density of states is

$$\rho(E) = \sum_n \delta_\epsilon(E - E_n). \quad (\text{E.6})$$

Here, $E = \frac{1}{2}(E_n + E_m)$ and $\Delta E = E_n - E_m$; $\delta_\epsilon(x)$ is a smoothed delta function, e.g. the Gaussian function: $\exp(-x^2/2\epsilon^2)/(\sqrt{2\pi}\epsilon)$. We characterize the energy scale in $\sigma^2(E, \Delta E)$ by the parameter ΔE_0 which is defined by

$$\Delta E_0 = \frac{1}{\sigma_0^2} \int_0^\infty d\Delta E \sigma^2(E_F, \Delta E), \quad (\text{E.7})$$

where $\sigma_0^2 = \sigma^2(E_F, 0)$. The function $\sigma^2(E, \Delta E)$ in the variable ΔE decays rapidly as $\Delta E \rightarrow \pm\infty$. The parameter ΔE_0 indicates the size of the interval over which σ^2 is significantly different from zero.

We assume that the matrix elements have a correlation function $C(t)$:

$$\left\langle \left(\frac{\partial H}{\partial X} \right)_{nm}(t) \left(\frac{\partial H}{\partial X} \right)_{n'm'}^*(t') \right\rangle = \delta_{nn'} \delta_{mm'} \sigma^2(E, \Delta E) C(t - t'), \quad (\text{E.8})$$

where $n \geq m$ and $n' \geq m'$. The characteristic time scale for the decay of correlations of the matrix elements is $\tau_c = (\sigma_0 \rho \dot{X})^{-1}$.

Here we consider a further simplified model since Eq. (E.4) is hard to solve directly. We replace Eq. (E.4) by

$$\dot{a}_n(t) = \epsilon \sum_{m \neq n} Z_{nm}(t) \exp[i\lambda(n - m)t] a_m(t), \quad (\text{E.9})$$

where $Z_{nm}(t)$ are elements of an anti-Hermitian matrix: $Z_{nm} = -Z_{mn}^*$, $Z_{nn} = 0$. The real and imaginary parts of $Z_{nm}(t)$ are independently Gaussian distributed random numbers. The correlation function of $Z_{nm}(t)$ is

$$\langle Z_{nm}(t_1) Z_{n'm'}^*(t_2) \rangle = \delta_{nn'} \delta_{mm'} f(n - m) C(t_1 - t_2), \quad (\text{E.10})$$

where $C(0) = 1$. This is a reasonable model for Eq. (E.4) when $\epsilon = \dot{X}$, $\lambda = (\hbar\rho)^{-1}$, and $f(\Delta n) = \sigma^2(\Delta E)/\Delta E^2$.

The solution of Eq. (E.9) is

$$a_n(t) = \sum_m U_{nm}(t, 0) a_m(0), \quad (\text{E.11})$$

where the matrix elements of the evolution operator $\hat{U} = \{U_{nm}\}$ satisfy a Dyson equation:

$$U_{nm}(t, 0) = \delta_{nm} + \epsilon \sum_k \int_0^t dt' Z_{nk}(t') U_{km}(t', 0) \exp[i\lambda(n - k)t']. \quad (\text{E.12})$$

Now we derive the equation of motion for occupation probabilities: $P_n(t) = \langle |a_n(t)|^2 \rangle$. Substituting Eq. (E.12) into Eq. (E.11) and using some approximation, we can obtain the following (See Ref. [51] for details):

$$P_n(t) - P_n(0) \sim \epsilon^2 t \sum_m \int_{-\infty}^\infty d\tau \langle Z_{nm}(\tau) Z_{nm}^*(0) \rangle \langle U_{mm}(\tau) \rangle \exp[i\lambda(n - m)\tau] (P_m(0) - P_n(0)). \quad (\text{E.13})$$

From Eq. (E.13),

$$\frac{dP_n}{dt} = \sum_m R_{nm}(P_m - P_n). \quad (\text{E.14})$$

Here the rate constants R_{nm} are given by

$$\begin{aligned} R_{nm} &= \epsilon^2 \int_{-\infty}^{\infty} d\tau \exp[i\lambda(n-m)\tau] \langle Z_{nm}(\tau) Z_{nm}^*(0) \rangle \langle U_{mm}(\tau) \rangle \\ &= \epsilon^2 f(n-m) \int_{-\infty}^{\infty} d\tau \exp[i\lambda(n-m)\tau] C(\tau) c(\tau), \end{aligned} \quad (\text{E.15})$$

where $c(\tau) = \langle U_{mm}(\tau) \rangle$. If the averaged occupation probability varies slowly as a function of n , $P_m - P_n$ can be Taylor expanded in $\Delta n = m - n$:

$$P_m = P_n + \frac{\partial P}{\partial n} \Delta n + \frac{1}{2} \frac{\partial^2 P}{\partial n^2} \Delta n^2 + O(\Delta n^3). \quad (\text{E.16})$$

Therefore, Eq. (E.13) can be approximated by a diffusion equation:

$$\frac{\partial P}{\partial t} = D \frac{\partial^2 P}{\partial n^2}, \quad (\text{E.17})$$

where the diffusion coefficient is

$$D = \frac{1}{2} \sum_m R_{nm} (n-m)^2. \quad (\text{E.18})$$

To analyze Eq. (E.4), we rewrite Eq. (E.15) as

$$R_{nm} = \dot{X}^2 \frac{\sigma(\Delta E)}{\Delta E^2} \int_{-\infty}^{\infty} d\tau \exp[i\Delta E \tau / \hbar] C(\tau) c(\tau), \quad (\text{E.19})$$

where $\Delta E = E_n - E_m \simeq (n-m)/\rho$. From Eq. (E.18), the diffusion coefficient is

$$\begin{aligned} D &= \frac{1}{2} \rho^3 \dot{X}^2 \int_{-\infty}^{\infty} d\Delta E \sigma^2(\Delta E) \int_{-\infty}^{\infty} d\tau \exp[i\Delta E \tau / \hbar] C(\tau) c(\tau) \\ &= \frac{1}{2} \rho^3 \dot{X}^2 \int_{-\infty}^{\infty} d\Delta E \sigma^2(\Delta E) F(\Delta E), \end{aligned} \quad (\text{E.20})$$

where we approximate the summation in Eq. (E.18) by an integral. The total weight of the function $F(\Delta E)$ is

$$\begin{aligned} \int_{-\infty}^{\infty} d\Delta E F(\Delta E) &= \int_{-\infty}^{\infty} d\tau C(\tau) c(\tau) \int_{-\infty}^{\infty} d\Delta E \exp[i\Delta E \tau / \hbar] \\ &= 2\pi\hbar \int_{-\infty}^{\infty} d\tau \delta(\tau) C(\tau) c(\tau) = 2\pi\hbar C(0) c(0) = 2\pi\hbar. \end{aligned} \quad (\text{E.21})$$

When $\Delta E_0 \gg \hbar\rho\sigma_0\dot{X}$, $F(\Delta E)$ decays rapidly to zero while $\sigma(\Delta E)$ is significantly different from zero. Then the diffusion coefficient is approximated as follows:

$$\begin{aligned} D &= \frac{1}{2} \rho^3 \dot{X}^2 \int_{-\infty}^{\infty} d\Delta E \sigma^2(\Delta E) F(\Delta E) \\ &\sim \frac{1}{2} \rho^3 \dot{X}^2 \sigma_0^2 \int_{-\infty}^{\infty} d\Delta E F(\Delta E) \\ &= \pi\hbar\rho^3 \sigma_0^2 \dot{X}^2. \end{aligned} \quad (\text{E.22})$$

When $\Delta E_0 \ll \hbar \rho \sigma_0 \dot{X}$, $\sigma(\Delta E)$ decays rapidly to zero while $F(\Delta E)$ is significantly different from zero. Then,

$$\begin{aligned} D &\sim \frac{1}{2} \rho^3 \dot{X}^2 \tau_c \int_{-\infty}^{\infty} d\Delta E \sigma^2(\Delta E) = \rho^3 \dot{X}^2 \tau_c \Delta E_0 \sigma_0^2 \\ &\sim \rho^2 \sigma_0 \Delta E_0 \dot{X}. \end{aligned} \tag{E.23}$$

Here $\tau_c = (\sigma_0 \rho \dot{X})^{-1}$.

From the above arguments, we now know that $D \propto \dot{X}^2$ for small \dot{X} and that $D \propto \dot{X}$ for large \dot{X} .

References

- [1] E. Teller, J. Phys. Chem. **41**, 109 (1937).
- [2] L. D. Landau and E. M. Lifshitz, *Quantum Mechanics* (Pergamon Press, London, 1958) p. 262.
- [3] A. S. Davydov: *Quantum Mechanics* (Pergamon Press, New York, 1965) p. 175.
- [4] J. von Neumann and E. Wigner, Phys. Z. **30**, 467. (1929)
- [5] O. J. Heilmann and E. H. Lieb, Ann. N. Acad. Sci. **172**, 583 (1971).
- [6] M. V. Berry and M. Wilkinson, Proc. R. Soc. London, Ser. A **392**, 15 (1984).
- [7] T. Deguchi, K. Fabricius and B. M. McCoy, J. Stat. Phys. **102**, 701 (2001).
- [8] K. Fabricius and B. M. McCoy, *MathPhys Odyssey 2001* ed. M. Kashiwara and T. Miwa (Birkhäuser, Boston, 2002) p. 119.
- [9] T. Deguchi, J. Phys. A **35**, 879 (2002).
- [10] S. E. Nagler, W. J. L. Buyers, R. L. Armstrong, and B. Briat, **27**, 1784 (1983).
- [11] H. Kikuchi *et al.*, Physica B **284-288**, 1631 (2000).
- [12] M. Hagiwara *et al.*, Physica B **294-295**, 83 (2001).
- [13] T. Deguchi and K. Kudo: Bussei Kenkyu (Kyoto) **80**, 195 (2003) [in Japanese].
- [14] K. Kudo and T. Deguchi, J. Phys. Soc. Jpn. **72**, 1599 (2003).
- [15] K. Kudo and T. Deguchi, Phys. Rev. B **68**, 052510 (2003).
- [16] K. Kudo and T. Deguchi, Phys. Rev. B **69**, 132404 (2004).
- [17] K. Kudo and T. Deguchi, cond-mat/0409761.
- [18] K. Kudo and K. Nakamura, in preparation.

- [19] A. Klümper, J. R. Reyes Martínez, C. Scheeren and M. Shiroishi, *J. Stat. Phys.* **102**, 937 (2001).
- [20] R. J. Baxter, *Exactly Solved Models in Statistical Mechanics* (Academic Press, London, 1982).
- [21] L. Takhtajan and L. Faddeev, *Russ. Math. Survey* **34**, 11 (1979).
- [22] L. A. Takhtajan, *Lecture Notes in Physics* (Springer-Verlag, Berlin, 1985) Vol. 242, p. 175.
- [23] M. L. Mehta, *Random Matrices*, 2nd ed. (Academic, San Diego, 1991).
- [24] M. V. Berry and M. Tabor, *Proc. R. Soc. Lond. A* **356**, 375 (1997).
- [25] O. Bohigas, M. J. Giannoni, and C. Schmit, *Phys. Rev. Lett.* **52**, 1 (1984).
- [26] G. Montambaux, D. Poilblanc, J. Bellissard, and C. Sire, *Phys. Rev. Lett.* **70**, 497 (1993).
- [27] T. C. Hsu and J. C. Anglès d'Auriac, *Phys. Rev. B* **47**, 14 291 (1993).
- [28] D. Poilblanc, T. Ziman, J. Bellissard, F. Mila, and G. Montambaux, *Europhys. Lett.* **22**, 537 (1993).
- [29] P. van Ede van der Pals and P. Gaspard, *Phys. Rev. E* **49**, 79 (1994).
- [30] J. C. Anglès d'Auriac and J. M. Maillard, *Physica A* **321**, 325 (2003).
- [31] D. A. Rabson, B. N. Narozhny, and A. J. Millis, *Phys. Rev. B* **69**, 054403 (2004).
- [32] H. Meyer, J. C. Anglès d'Auriac, and H. Bruus, *J. Phys. A* **29**, L483 (1996).
- [33] H. Meyer, J. C. Anglès d'Auriac, and J. M. Maillard, *Phys. Rev. E* **55**, 5380 (1997).
- [34] H. Meyer and J. C. Anglès d'Auriac, *Phys. Rev. E* **55**, 6608 (1997).
- [35] J. C. Anglès d'Auriac and F. Iglói, *Phys. Rev. E* **58**, 241 (1998).
- [36] R. Berkovits, and Y. Avishai, *J. Phys. C: Condens. Matter* **8**, 389 (1996).
- [37] B. Georgeot and D. L. Shepelyansky, *Phys. Rev. Lett.* **81**, 5129 (1998).
- [38] Y. Avishai, J. Richert, and R. Berkovits, *Phys. Rev. B* **66**, 052416 (2002).
- [39] L. F. Santos, *J. Phys. A* **37**, 4723 (2004).

- [40] B. I. Shklovskii, B. Shapiro, B. R. Sears, P. Lambrianides, and H. B. Shore, *Phys. Rev. B* **47**, 11487 (1993).
- [41] N. Nakazono, T. Kato, and K. Nakamura, *Prog. Theor. Phys. Supp.* **150**, 165 (2003); S. Sawada *et al.*, in preparation.
- [42] S. Hirata and K. Nomura, *Phys. Rev. B* **61**, 9453 (2000).
- [43] K. Nomura and K. Okamoto, *J. Phys. A* **27**, 5773 (1994).
- [44] L. Urba, A. Rosengren, *Phys. Rev. B* **67**, 104406 (2003).
- [45] See articles in *Quantum Chaos Y2K, Proceedings of Nobel Symposium* edited by K. F. Berggren and S. Åberg (Royal Swedish Academy of Sciences/World Scientific, Singapore, 2001).
- [46] G. Jona-Lasinio and C. Presilla, *Phys. Rev. Lett.* **77**, 4322 (1996).
- [47] T. Prosen, *Phys. Rev. Lett.* **80**, 1808 (1998); T. Prosen, *Phys. Rev. E* **60**, 3949 (1999).
- [48] V. V. Flambaum and F. M. Izrailev, *Phys. Rev. E* **64**, 026124 (2001).
- [49] M. Wilkinson, *J. Phys. A* **21**, 4021 (1988).
- [50] M. Wilkinson and E. J. Austin, *Phys. Rev. A* **46**, 64 (1992).
- [51] M. Wilkinson and E. J. Austin, *J. Phys. A* **28**, 2277 (1995).
- [52] A. Bulgac, G. D. Dang, and D. Kusnezov, *Chaos, Solitons and Fractals* **8**, 1149 (1997).
- [53] D. Cohen and T. Kottos, *Phys. Rev. Lett.* **85**, 4839 (2000).
- [54] D. Cohen, F. M. Izrailev, and T. Kottos, *Phys. Rev. Lett.* **84**, 2052 (2000); D. Cohen, *Lecture Notes in Physics* **597** edited by P. Garbaczewski and R. Olkiewicz, p. 317 (2002).
- [55] M. Machida, K. Saito, and S. Miyashita, *J. Phys. Soc. Jpn.* **71**, 2427 (2002).
- [56] Y. Kitaoka *et al.*, *J. Phys. Soc. Jpn* **67**, 3703 (1998); V. P. Plakhty *et al.*, *Phys. Rev. Lett.* **85**, 3942 (2000); A. Lascialfari *et al.*, *Phys. Rev. B* **67**, 224408 (2003).
- [57] K. Nakamura, Y. Nakahara, and A. R. Bishop, *Phys. Rev. Lett.* **54**, 861 (1985); K. Nakamura, *Quantum Chaos* (Cambridge University Press, Cambridge, 1993).

- [58] H. Yamasaki, Y. Natsume, A. Terai, and K. Nakamura, *J. Phys.: Condens. Matter* **16**, L395 (2004).
- [59] M. Suzuki, *Phys. Lett. A* **146**, 319 (1990).